University of California
Santa Barbara

Diverse synthetic methods for the preparation of polymer materials

A dissertation submitted in partial satisfaction
of the requirements for the degree

Doctor of Philosophy
in
Chemistry

by

Anna Melker

Committee in charge:

Professor Craig J. Hawker, Chair
Professor Javier Read De Alaniz
Professor Ram Seshadri
Professor Galen Stucky

January 2018

The Dissertation of Anna Melker is approved.

Professor Javier Read De Alaniz

Professor Ram Seshadri

Professor Galen Stucky

Professor Craig J. Hawker, Committee Chair

January 2018

Diverse synthetic methods for the preparation of polymer materials

by

Anna Melker

To my husband, Olof Jonsson

That the nobility of Man, acquired in a hundred centuries of trial and error, lay in making himself the conquerer of matter, and that I had enrolled in chemistry because I wanted to maintain faithful to that nobility. That conquering matter is to understand it, and understanding matter is necessary to understanding the universe and ourselves. -Primo Levi

Acknowledgements

I am grateful to my research advisor, Professor Craig Hawker, for the opportunity to work in his world-class laboratory. During my time at UCSB, Craig has given me the opportunity to work on so many different sides of polymer science, put his belief in me to work independently, and encouraged me to collaborate with different groups on campus and at KTH. Craig taught me so much about experimental design and how to do rigorous science, always pushing me to do better and ask more questions, making me a better scientist.

I also thank Professor Ram Seshadri for his heartfelt encouragement and mentorship throughout my doctoral studies. Ram made Saturday and Sundays at the MRL a fun time. Professor Galen Stucky and Professor Javier Read De Alaniz: thank you for your great questions on my work as my thesis committee members, and for reading this dissertation.

Professors Jonas Goldsmith and Ryan Hayward: without your support, encouragement, and belief in my abilities, I would never have considered a career in science. Thank you for mentoring me as an undergraduate and continued guidance throughout my career.

I am grateful to the mentors who taught me how to work in the laboratory and interpret data: Scott Christenson, who first introduced me to the world of polymer science and his love for DeGennes, Ryan Fealy, whose good spirits and patient hands taught me so much at Bryn Mawr College, Justin Poelma, whose enthusiasm and advice have shaped my research career at UCSB, and finally, Athina Anastasaki, who pushed me to work harder and succeed. I would not be the scientist I am today without all of your guidance.

I deeply appreciate and thank Professor Eva Malmström and Professor Michael Malkoch for the opportunity to work in their labs and collaborate with their talented students: I learned so much from you, and working with you in Stockholm was an absolute pleasure every single day. I would like to thank Fiona Hatton, Kristina Olofsson, Carmen Cobo Sanchez, Sarah Brännström, Emma Larsson, Oliver Andren, Viktor Granskog, Jokke Engström, Samer Nameer, Sandra Garcia Gallego, Jamie Godfrey, Jonna Holmqvist, Alexandra Holmgren, Patrik Stenström, Assya Boujemaoui, Sam Pendergraph, Christian Porsch, Martin Wåhlander, Janne Mongkhontreerat, and Ville Olsson. Thank you also for giving me the opportunity to mentor students, I had so much fun teaching Zozan Tunc, Hannah Hemlin, and Sofia Carlsson.

I thank the following people for their friendship and endless support at UCSB: Edward Toumayan, Cynthia Wang, Brenden McDearmont, Megan Butala, Vicky Doan Nguyen, Fang Narupai, Matt Menyo, Elijah Shelton, Chelsea Catania, Michael Gotrik, Carolin Fleischmann, and Yingdong Luo. I also thank the following postdocs for helpful scientific discussions over the years: Revital Kaminker, Bernd Oschmann, Frank Chiu, Shaoguang Li, Anna Lehrner, Daniel Klinger, Jimmy Lawrence, Bas Van Ravensteijn, Reggie Bou Zerdan, Brett Fors, and Will Gutekunst.

The MRL has been a great place to work thanks to the hard work and cheerfulness of Rachel Behrens, Amanda Ström, Mary McGuan, Dotti Pak, Jerry Hu, Julie Standish, Fuzzy Rodgers, Miguel Zepeda, Tom Mates, Phillip Kohl, Shamon Walker, and Jaya Nolt. Thank you for your patience in teaching me how to use new instruments and for always making me smile.

Finally, this dissertation would not be possible without the unconditional, loving support of my family, Neil, Ilona, Shari, Shula, and Jared, and my husband, Olof. Thank you for always being there for me.

Curriculum Vitæ

Anna Melker

Education

2017	Ph.D. in Chemistry (Expected), University of California, Santa Barbara.
2017	Certificate in Technology Management Practice, University of California, Santa Barbara.
2012	B.A. *Magna Cum Laude* in Chemistry, Bryn Mawr College.

Research Experience

2013-2017	Graduate Student Researcher, University of California, Santa Barbara. Advisor: Craig Hawker.
2015-2016	Visiting Research Fellow, KTH Royal Institute of Technology, Stockholm, Sweden. Advisors: Eva Malmström and Michael Malkoch. Project: From Trash to Functional Material: Synthesis of bio-based, cellulose reinforced electrolytes for next generation Li-S batteries.
2012-2013	Fulbright Fellow, Uppsala University, Uppsala, Sweden. Advisor: Leif Hammarström. Project: Artificial Photosynthesis for Hydrogen Production.
2011-2012	Undergraduate Student Researcher, Bryn Mawr College. Advisor: Jonas Goldsmith. Thesis: Optimization of hydrogen production systems through different combinations of photosensitizers and electron relays.
2010	REU Intern, University of Massachusetts-Amherst. Advisor: Ryan Hayward.

Publications

Anastasaki, A., Oschmann, B., Willenbacher, J., **Melker, A.**, van Son, M. H. C., Truong, N. P., Schulze, M. W., Discekici, E. H., McGrath, A. J., Davis, T. P., Bates, C. M., Hawker, C. J. One pot synthesis of ABCDE multiblock copolymers with hydrophobic, hydrophilic, and semi-fluorinated segments. Angewandte Chemie. doi: 10.1002/anie.201707646

Melker, A., Fors, B. P., Hawker, C. J. and Poelma, J. E. (2015), Continuous flow synthesis of poly(methyl methacrylate) via a light-mediated controlled radical polymerization. J. Polym. Sci. A Polym. Chem., 53: 26932698. doi: 10.1002/pola.27765

Presentations

August 2017	Lecture, "Polymer Self-Assembly: A Love-Hate Relationship Creates Order." *Lunch and Learn*, UCSB
October 2016	Invited lecture, "Towards sustainable and scalable materials for next generation Li-S batteries." *Southern California Electrochemical Energy Alliance*, UCSB
February 2016	Poster, "Polymeric, sulfur cathodes based on renewable feedstocks." *Materials Research Outreach Program Symposium*, UCSB
December 2015	Poster, "Synthesis of Novel, Sulfur-rich polymers: poly(sulfur-co-myrcene)." *Pacifichem*, Honolulu, Hawaii
August 2014	Poster, "Continuous Flow Synthesis via a Light-Mediated Controlled Radical Polymerization." *American Chemical Society National Meeting*, San Francisco, CA

Fellowships

2016	American Scandinavian Foundation, John G. Bergqvist fund for Chemistry Fellowship, $5,000
2016	International Center for Materials Research (ICMR) Study Abroad Fellowship, $5,000
2016	Swedish Research Council (Vetenskapsrådet) Fellowship, 166,140 SEK
2015	National Science Foundation Graduate Research Opportunities Worldwide Fellowship, $5,000
2013	National Science Foundation Graduate Research Fellowship, $136,000
2012	Fulbright Fellowship to Sweden, 110,000 SEK
2010	National Science Foundation Research Experience for Undergraduates, University of Massachusetts-Amherst, $5,000

Awards

2017	Professional Development Award, UCSB, $400
2015	Outstanding Service to the Department of Chemistry, UCSB, $300
2014, 2015	Dow-Materials Research Laboratory Travel Award, UCSB, $1250
2014	American Chemical Society Conference Travel Award, Controlled Radical Polymerization Symposium, $500

Mentoring and Leadership

2014-2017	President (2017), Graduate Students for Diversity in Science, UCSB
2016	Teaching Assistant, KTH Royal Institute of Technology
2011-2012	Teaching Assistant, Bryn Mawr College

Volunteering and Science Outreach

2016	Judge, Polymer Networks Group Conference, KTH, Stockholm, Sweden
2014-present	Science Outreach Volunteer at Materials Research Laboratory, UCSB

Languages

English (native), French (fluent), Swedish (intermediate), Hungarian (intermediate), Korean (basic), Latin (basic)

Professional Associations

American Chemical Society, American Association for the Advancement of Science, Swedish Fulbright Alumni Association, Fulbright Alumni Association- Greater Los Angeles Chapter

Abstract

Diverse synthetic methods for the preparation of polymer materials

by

Anna Melker

New synthetic methods in polymer chemistry developed over the last twenty years and advances in materials characterization tools have enabled the creation of highly defined, discrete polymers. The advances in chemistry allow for the targeting of specific molar masses with low molar mass distributions, which in turn allows for more direct studies of structure-to-property relationships, including matching experimental results more closely with theory. Facile, one-pot synthesis of diblock and multiblock copolymers to high monomer conversion, without the need to stop and purify after each addition, have enabled precise control over molar masses with high degrees of chain end fidelity and where each block has a discrete, known composition. When the blocks are chosen to be chemically incompatible e.g. immiscible, they can undergo interesting self-assembly behavior to form spherical, hexagonally packed, gyroid, and lamellar architectures, depending on the degree of polymerization, volume fractions of each block, and the repulsive interactions between the monomers. As each of the blocks can be precisely known down to each degree of polymerization, this enables the construction of accurate phase diagrams with high degrees of certainty for these materials. This helps develop a closer match between experimentalists and theorists looking to design new materials with never-before-seen phases and properties, ultimately advancing

the applications of block copolymers in nanotechnology.

Contents

Chapter 1

Introduction

1.1 Permissions and Attributions

1. The content of chapter 2 has previously appeared in the Journal of Polymer Science: Part A, Polymer Chemistry. It is reproduced here in accordance with the journal's author use guidelines.

1.2 Polymerization Techniques and Characterization

Recent advances in polymer synthesis have allowed polymer chemists to develop polymerizations with unprecedented degrees of control. [1, 2] Under ideal conditions in these reactions, chain ends successfully pop on and off in a controlled manner to accommodate more monomer units over time, leading to polymers with nearly equal chain lengths. These polymerizations are marked by min-

imal to no termination events or side reactions hampering polymer growth and are highly prized among the polymer community to make discrete materials of known composition. Mimicking the ability of nature to create precise materials ushers in unprecedented control over molecular architecture, allowing for more concrete studies on structure-to-property relationships and enabling the design and synthesis of new materials for very specific applications.

Polymers synthesized through techniques such as atom-transfer radical polymerization (ATRP), [3] reversible addition-fragmentation chain-transfer (RAFT), [4] and nitroxide-mediated polymerization (NMP) [5] result in materials with a high degree of control over molar mass, affording even molar mass distributions (Đ, the polydispersity index), retention of chain end fidelity, and in some cases, precisely known, discrete molecular architecture (such as pertaining to diblock or multiblock functionalities). In light-mediated ATRP, particular combination of solvents and photocatalysts allowed the synthesis of methacrylates and acrylates, depending on exact reaction conditions. The discovery of the use of $Ir(ppy)_3$ to control synthesis of methacrylates in NMP solvent was presented by Fors and Hawker [6] and explored herein. The proposed reaction mechanism is shown in Figure 1.1.

Copper catalyzed ATRP is a more traditional form of controlled radical polymerization, but recent variations include the addition of copper wire [8] or conducting the polymerizations under irradiation. [9]. This chemistry enables the facile synthesis of acrylic polymers through high conversion (> 95 %) in a variety of solvents (Figure 1.2).

Concurrently, molar mass and molar mass distributions have the ability to

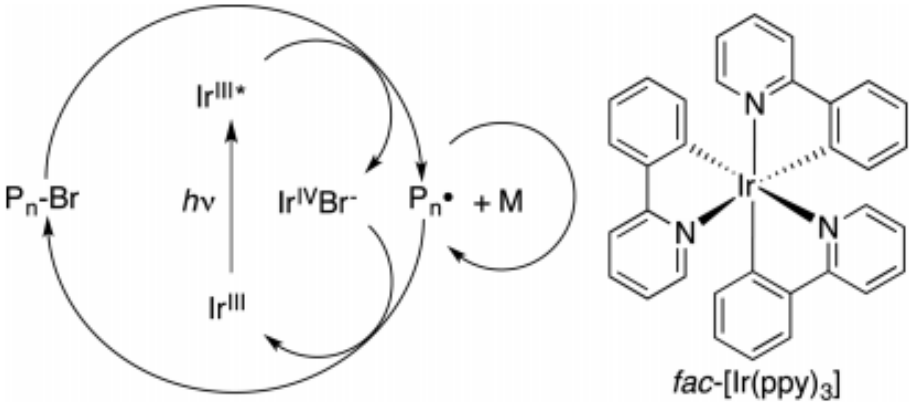

Figure 1.1: A proposed mechanism for the controlled radical polymerization of methacrylates using visible light and an Ir-photocatalyst. P_n refers to the growing polymer chain. Scheme reproduced from references [6] and [7].

affect properties of the polymer material. Just a small variation in chain length between polymer chains could have an affect on the nanoscale packing and order of self-assembling polymers. [10] However, the end applications of the resultant polymer may not depend on the polymerizations being highly controlled. Indeed, in some cases some degree of variation between chain lengths or chain end fidelity can be tolerated and even sought after. Such is the case with highly branched and crosslinked materials, where a Đ> 1.5 is a desirable attribute. A consequence of uncontrolled, negative termination reactions could be a high Đ.

For example, a focus of part of the work herein was on free-radical polymerization of sulfur with unsaturated hydrocarbons. [11] Heat-activated ring opening of elemental sulfur above 159°C induces free radical polymerization through unsaturated bonds in alkenes and alkynes (Figure 1.3). The final architecture of the polymer was designed to be highly branched and crosslinked, to form a network amenable to Li ion transportation and conduction.

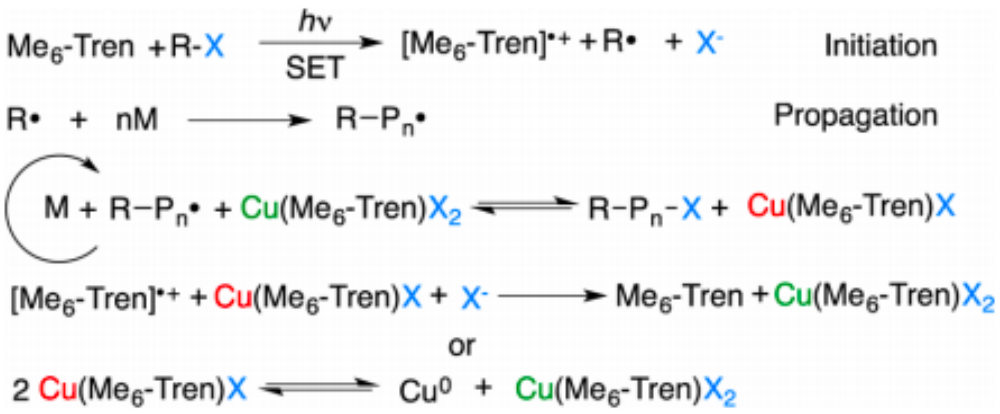

Figure 1.2: A proposed mechanism for the controlled radical polymerization of (meth)acrylates using visible light, a tertiary amine ligand (Me_6Tren), and a copper catalyst. Scheme reproduced from references [7] and [9].

The controlled nature of a polymerization can be determined through kinetic experiments, where the reaction mixture is sampled over the course of time to determine how much of the starting material remains and how much of the product has been made. Recent experiments using magnetic tweezers have shown that unlike speculations that controlled polymer growth occurs in continuous defined steps, polymers are grown in growth spurts. [12] Regardless of the livingness of a reaction, it is useful to determine polymer addition over time from kinetic experiments. Kinetics can be monitored by Nuclear Magnetic Resonance (NMR) by integrating the peak corresponding to certain protons on the polymer and comparing it to the size of the peak for the monomer protons. The ratio of concentration of monomer at time zero ($t = 0$) divided by the concentration of monomer at time $= t$ gives information on the percent conversion. The logarithm of this ratio, when plotted against time $= t$, is a straight line for the polymerization to be considered controlled or living.

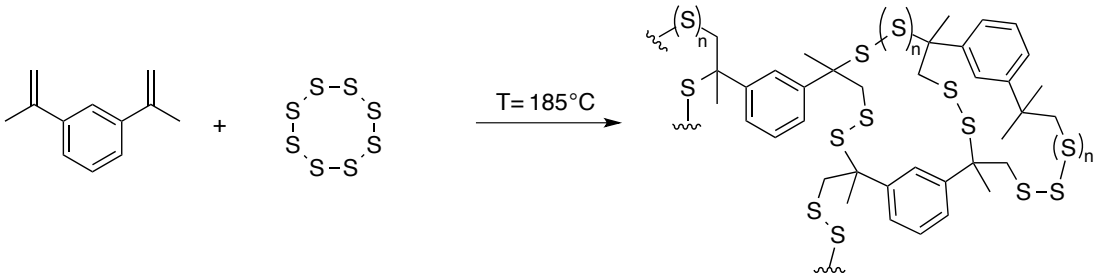

Figure 1.3: A ring opening polymerization, termed inverse vulcanization, occurs at high temperature, where sulfur diradicals attack alkenes to form polymeric sulfur. Scheme reproduced from reference [11].

Other techniques, such as Differential Scanning Calorimetry (DSC), Gel Permeation Chromatography/Size Exclusion Chromatography (GPC or SEC), Fourier Transform Infrared Spectroscopy (FTIR), and Gas Chromatography Mass Spectrometry (GC MS) can also be used. In the case of GPC, which is most commonly used as a complementary method to reaffirm NMR results and give a additional information on molar mass and molar mass distribution of the polymer, crude reaction mixtures are injected into the GPC instrument and polymer molecules are sorted based on residence time in the column. Therefore, at the beginning of the reaction, the polymer chain lengths will be shorter and have a longer retention time on the column than at the end of the polymerization, assuming linear growth and no negative side reactions occur, such as termination events. DSC can be used for samples that are insoluble and where starting materials or products have a distinct signature in the DSC, such as a melt temperature (T_m) or a glass transition temperature (T_g), and it can be a facile, lower cost alternative to solid state NMR. However, simply the appearance or disappearance of one of these peaks is not thorough enough: in the case of sulfur-containing polymers, a calibration curve must be made for known amounts of elemental sulfur before

determining the amount of unreacted sulfur remaining in the final product. [11] Electron Spray Ionization Mass Spectrometry (ESI MS) and MALDI TOF experiments are commonly employed to determine chain end fidelity, which is important for additional functionalization such as growing a second block of polymer and as a way to check for reaction control. [13]

Determining the molecular composition of insoluble, non-carbon based polymers, such as those containing high amounts of sulfur or silicon, necessitates different instrumentation. X-Ray Photoelectron Spectroscopy (XPS) is a highly useful technique for analyzing powders and thin films, where x-rays penetrate the surface of the polymer film (<10nm depth) with specific x-ray energies to release k-shell electrons. XPS gives structural information on which atoms are connected to one another and the relative abundances of each atom. For more information on film composition, in cases where there can be two or more films or in diblock copolymers, DSIMS is useful as it ablates away layers to determine composition based on depth, similar to X-Ray Reflectivity Diffractometry (XRD) used for inorganic materials. XPS is a great technique for diblock copolymers composed partially of fluorinated blocks, which selectively assemble at the top of a thin polymer film, leading to interesting surface properties. [14] Fourier Transform Infrared Spectroscopy is another technique to determine which functional groups are present on an insoluble polymer, especially helpful to determine whether a reaction has succeeded in transforming a functional group. In the case of sulfur-containing polymers, Raman spectroscopy is useful as it shows S-S bond signatures.

1.3 Physical Properties

The end applications of polymers often require specific physical attributes. Physical properties of polymers are commonly reported alongside organic reaction characterization data, going further than traditional melting point data of organic compounds. Differential Scanning Calorimetry (DSC) and Thermal Gravimetric Analysis (TGA) are employed to determine thermal properties of polymers. DSC gives information on enthalpy of heat, melting and crystallization temperatures, and glass transition temperature. Rates of heating, whether a sample is first heated or cooled, as well as size of the sample, all affect the data collected. Therefore, changes in sample prep can lead to slight variations in the size of thermal transitions and should be noted when comparing data to the literature and between samples. Data should be reported from the second or third heating or cooling cycle to remove thermal history of the sample, except in the cases where DSC is used to determine at what temperature the reaction occurs between starting materials.

TGA is used to determine how temperature affects the polymer, such as under intensive applications in high heat applications. When dealing with temperature sensitive polymers, it is important to know at what temperature they degrade or change. This is especially important with poly(*tert*-butyl acrylate), where the *tert*-butyl group can be thermally excised from the polymer chain to form poly(acrylic anhydride) at an elevated temperature. Caution should be taken when thermally annealing these polymers for SAXS experiments and any other thin film characterization, as their morphology could change upon thermal deprotection to the anhydride. [15] Thermosets are polymers that have high heat

tolerance and do not degrade (measured as a loss of mass) until high temperatures, usually above 300°C. Thermosets typically do not melt, but degrade before they reach the temperature at which they would melt. TGA data represent the degradation temperature at which 5% of the mass has been lost, T_{deg}.

1.4 Polymer Morphology

The study of the three dimensional structure of polymer chains is a critical component to property-driven materials design. Polymers self-organize or self-assemble into shapes depending on a variety of forces, from intermolecular and intramolecular repulsions and attractions to Van Der Waals forces, hydrogen bonding, and electrostatic repulsions. Polymers follow a random walk described by Brownian motion equations, but in the case of mixed homopolymer blends and diblock copolymers, things become more complicated. Single Chain in Mean Field Theory (SCFT) calculations are used to approximate equilibrium morphologies exhibited by polymer blends or copolymers based on factors such as χ and the relative composition of each component. Polymer morphology is observed experimentally with Small Angle X-Ray Scattering where reflections on a 2D image are processed to give a signature profile where the mathematical relationships between each inflection point to a specific morphology. [16] The canonical polymer morphologies are spherical, cylindrical, gyroid, and lamellae, although many more have been found and are theorized to exist (Figure 1.4).

The work described herein deals with three distinctive polymerization strategies to obtain materials for a broad array of applications using either light or

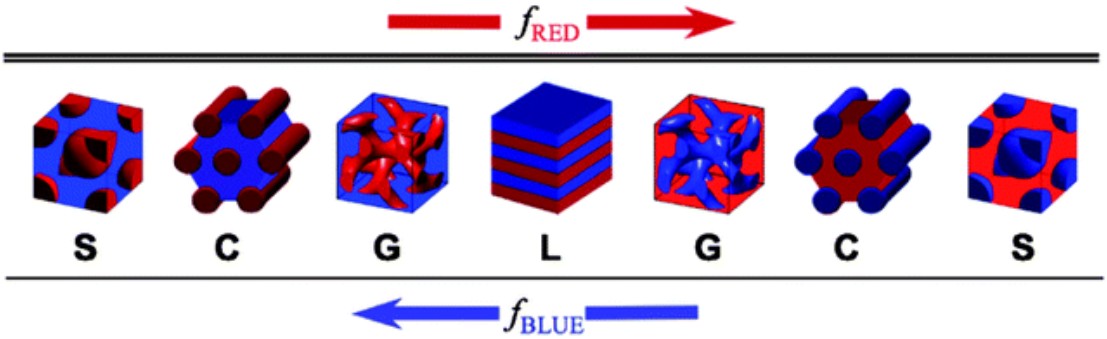

Figure 1.4: The four canonical morphologies that block copolymers can self--assemble into: spherical (S), cylindrical (C), gyroid (G), and lamellar (L). Diagram here reproduced from reference [17].

heat stimuli: light-mediated $Ir(ppy)_3$-catalyzed controlled radical polymerization, light-mediated Cu ATRP, traditional Cu ATRP with copper wire (Cu (0)), and high temperature, free radical inverse vulcanization for high sulfur catenation materials. A particular focus of many of the projects was applications driven: characterizing the materials beyond their chemical composition to their use as the cathode material in Li-S batteries or analyzing their self-assembly behavior. Chapter 2 describes the engineering of light-mediated $Ir(ppy)_3$ polymerizatios in continuous flow reactors. Chapter 3 explores the use of sulfur-containing polymers in Li-S batteries. Chapter 4 and 5 look at a series of highly defined diblock copolymers, their self-assembly behavior, and resulting morphology through Small Angle X-Ray Scattering. Chapter 6 describes a synthesis for fluorinated and hydrophobic star polymers via Cu(0) chemistry in a fluorinated solvent, with high chain end integrity to synthesize block stars with minimal side reactions. The ability to access new morphology in diblock copolymers is a direct result of unprecedented control over polymerizations with exciting new synthetic polymer strategies, allowing us to design a library of polymers to access never-before-seen polymer morphologies.

Chapter 2

Continuous flow synthesis of poly(methyl methacrylate) via a light-mediated controlled radical polymerization

2.1 Introduction

Controlled radical polymerization techniques such as atom transfer radical polymerization (ATRP), reversible addition fragmentation chain transfer polymerization (RAFT) and nitroxide mediated polymerization (NMP) have gained considerable attention in the past several decades. An enabling feature of this technology is that non-experts can easily gain access to well-defined macromolecular architectures based on the polymerization of a wide range of functionalized vinyl

monomers. Recently, the ability to regulate controlled polymerizations through a variety of stimuli has significantly increased the scope of applications for these processes. [18, 19]

With the use of accessible external stimuli, such as applied voltage, [20] mechanical force [21] and light, [6, 22, 23, 24, 25, 26, 27, 28] the promise of controlling the chain growth process *in situ* has been realized. Light is an especially attractive external stimulus because of its availability and ability to provide both spatial and temporal control. Recently, our group reported on the light-mediated controlled radical polymerization of methacrylates and acrylates using traditional inorganic photoredox systems, such as *fac*-$\mathrm{Ir(ppy)_3}$ [6, 28] as well as novel organic catalysts. [27] These polymerizations are highly responsive to visible light, allowing chain growth to be turned "on" and "off," while maintaining control over molecular weight and dispersity (Đ). However, scaling these reactions presents several challenges. [29] Perhaps the most significant obstacle for large-scale reactions is achieving even and full penetration of light through the reaction media, a consequence of Beer-Lambert's law. [30, 31]

Even at 50 ppm concentrations, the high molar extinction coefficient of *fac*-$\mathrm{Ir(ppy)_3}$ (12,000 $\mathrm{M^{-1} \cdot cm^{-1}}$) results in 99% of incident light being absorbed in the first 1.4 cm. Furthermore, the rate of polymerization decreases exponentially with increasing distance from a light source. A secondary consequence of light being absorbed unevenly through the depth of the reactor is the range of polymerization rates present in one reaction. Chains growing at different rates depending on their location in the reactor could give rise to broader dispersities for the resulting polymer. Continuous flow microreactors are particularly attractive for addressing

the drawbacks of light-mediated reactions. [32, 33]

Photoredox catalysed transformations on small molecule substrates have benefited from simple flow reactors, [31] and at least one UV-induced polymerization of methyl acrylate was recently reported by Wenn et al. [34] The high surface area to volume ratios typical of tubular microreactors enable full and even penetration of light through the reaction media by reducing the path length. As a result, the reaction rate, scalability, and reproducibility of light mediated reactions have been improved by utilizing flow reactors over traditional batch reactions. [35] Several groups have recently demonstrated the advantages of using continuous flow reactors in polymer synthesis. [33, 36] Polymerizations that have very fast kinetics [37] or are highly exothermic [38] have benefited from the efficient mixing ability and heat exchange capabilities of flow reactors. Controlled radical polymerizations have also been performed under flow conditions [39, 40] allowing for the synthesis of libraries of polymers with control over molecular weight and low dispersities. [41] Diehl et al. [42] demonstrated an increase in polymerization rate for the synthesis poly(N-isopropylacrylamide) under flow conditions compared to conventional heating strategies. However, flow reactors have several drawbacks that prevent their widespread adoption for polymerizations. The greater surface-area-to-volume ratio of flow tubing increases the likelihood of oxygen permeation, which can be detrimental to oxygen sensitive controlled radical polymerizations. Therefore, the choice of reactor materials is crucial to the operation of a continuous flow setup.

The most widely used tubing material in continuous flow reactors is perfluoroalkoxy alkane (PFA), which has the favourable properties of being translucent,

flexible, and chemically resistant. However, PFA is highly permeable to oxygen. This problem has caused several groups to look elsewhere for suitable reaction vessels. For example, Thang and coworkers [43] were unable to perform RAFT in PFA tubing due to radical quenching and moved to stainless steel tubing. Recently, fluorinated ethylene propylene (FEP) has been investigated as a reactor material but also suffers from high permeability to oxygen. [44] In this study, we investigated four widely available tubing materials, PFA, FEP, tetrafluoroethylene (Tefzel), and ethylene chlorotrifluoroethylene (Halar), for the light-mediated polymerization of MMA catalysed by *fac*-Ir(ppy)$_3$. We then compared two of the tubing materials with very different oxygen barrier properties in order to understand the impact of oxygen diffusivity on polymerization kinetics. Finally, the material with the best barrier properties was compared to batch reactions under identical conditions in order to demonstrate the rate enhancement over traditional reaction setups for light-mediated polymerizations.

2.2 Methods

Poly(methyl methacrylate) was synthesized by photomediated controlled radical polymerization as previously reported by Fors et al.5 1-Methyl-2-pyrrolidinone (NMP, Sigma Aldrich, ReagentPlus, 99 %), Ethyl α-bromophenylacetate (Sigma Aldrich, 97 %), and Tris[2-phenylpyridinato-C2,N]iridium(III) (Ir(ppy)$_3$, Sigma Aldrich) were used as received without further purification. The MEHQ inhibitor in methyl methacrylate (Sigma Aldrich, 99%) was removed by filtering over a plug of basic alumina. PFA, Tefzel, Halar, and FEP tubing were purchased from Idexx

Health and Sciences.

The molecular weight of the poly(methyl methacrylate) was determined with gel permeation chromatography (GPC) using PS standards and ^{1}H NMR spectroscopy (Varian, 600MHz) by integrating the resonances for the initiator (ethyl α-bromophenylacetate) and comparison to unique resonances for PMMA. All NMR spectra were obtained in deuterated chloroform and analysed using MestReNova software. Dispersity indices (Đ) were determined by gel permeation chromatography (GPC) using either a Waters 2695 separation module with a Waters 2414 refractive index detector in chloroform (0.25% triethylamine) against polystyrene standards or using a GPC MALS detector, with the same manufacture of eluting column and separation module equipped with four additional detectors: Wyatt DAMN HELEOS-II, Wyatt Optilab rEX, Waters 2996 Photodiode Array Detector, and Wyatt ViscoStar.

Continuous flow setup

The continuous flow reactor was assembled by wrapping 550 cm of either Halar, PFA, FEP, or Tefzel tubing (I.D. 0.02 in) around the outside of a retrofitted 1L beaker with no bottom to maximize ambient air flow cooling (Figure 2.1). One end of the reactor was fitted to a static mixing tee and two inlet lines while the other end was attached to a collection vial. Two degassed solutions were prepared and added to separate plastic Air-Tite Luer Lock syringes for injection via a syringe pump (New Era Pump Systems Inc.). In a typical reaction, one solution contained 0.005 mol% (1.77 mg, 2.703 $\cdot 10^{-3}$ mmol) of the catalyst: *fac*-Ir(ppy)$_3$, in N-methylpyrrolidone (NMP) (13 mL), and the other contained a solution of monomer and initiator: methyl methacrylate (MMA) (53.9 mmol, 5.77 mL) and

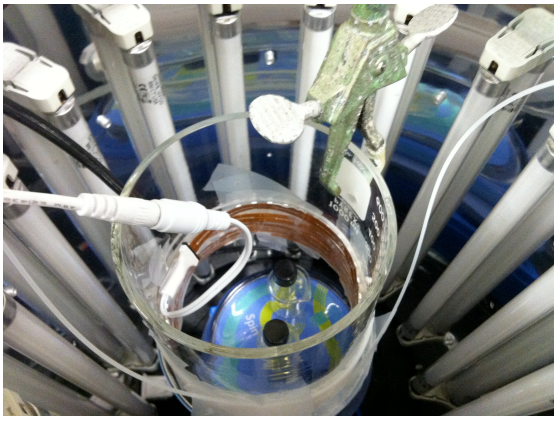

Figure 2.1: 1L retrofitted beaker with tubing wrapped around the outside and LEDs (λ = 380 nm) taped to the inside. Flow reactor was suspended inside a Rayonet reactor equipped with bulbs and fan cooling.

ethyl α bromophenyl acetate (0.537 mmol, 94.0 μL) in 7.15 mL NMP. To avoid any oxygen contamination in the tubing, argon followed by degassed NMP was flowed through the microtube reactor prior to each reaction and an argon balloon was employed at the outlet line in the collection flask (Figure 2.2).

All reactions were performed at room temperature in a Rayonet light box (Figure 2.2) equipped with (λ = 380 nm) bulbs and a fan for cooling. When comparing polymerization kinetics of the PFA and Halar reactors, the flow reactor was also irradiated from the inside of the beaker with a strip of LEDs (λ= 380 nm), purchased from Elemental LED. The same LEDs were also used as additional radiation in the batch reactions for comparison to the Halar flow experiments.

Flow rates were varied between 1 μL min^{-1} to 20 μL min^{-1} to achieve residence times ranging from 25 to 500 minutes. These were determined according to the following calculations:

Length of tubing x 2π x (inside radius of tubing)^2 = Volume of reactor in μL

Residence time = Volume of reactor μL / (total syringe flow rate μL*minutes^{-1}

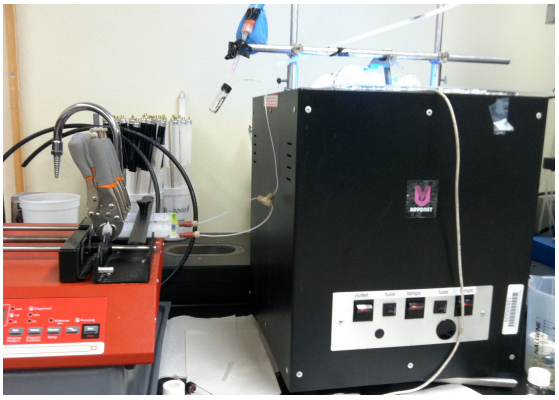

Figure 2.2: Syringe pump, with t-mixer and connectors to flow reactor inside of Rayonet box. Reaction mixture was collected in a vial with Argon-filled balloon attached.

x 100) Equilibration time = 2 x residence time

For example, the calculation for the 220 minute time point is as follows: 5500 mm x 2π x (0.254 mm)^2 = 11.14 μL

and

11.14 μL/(5 μL x minutes^{-1} x 100) = 222 minutes residence time

Rate per each syringe (2 total) = 2.25 μL minutes^{-1}

Equilibration time = 2 x 222 minutes = 445 minutes

The reactor was allowed to equilibrate for two residence times before collecting the crude reaction mixture for analysis. For comparison, batch reactions were prepared in 20 mL scintillation vials from stoichiometrically equivalent degassed reactant volumes under identical lighting conditions as for the flow experiments.

2.3 Comparison Between Different Types of Tubings

We first investigated the choice of tubing material for use in the continuous flow reactor by comparing their performance under identical reaction conditions. Four fluoropolymer tubing materials: PFA, FEP, Tefzel, and Halar, were chosen to compare the effect of transparency and gas barrier properties on the light mediated polymerizations. The oxygen permeability values for the tubing materials are listed in the table in Figure 2.3. PFA and FEP possess similar properties with oxygen permeability values of 881 and 748 respectively ($cm^3 \cdot 100in^{-2} \cdot 24h \cdot atm \cdot mil^{-1}$), good chemical resistance, and high transparency. Tefzel and Halar are less transparent but exhibit superior oxygen barrier properties with permeability values as low as 100 and 25 ($cm^3 \cdot 100in^{-2} \cdot 24h \cdot atm \cdot mil^{-1}$), respectively (per manufacturer specifications from Upchurch Scientific). This represents a 35-fold difference in oxygen permeability between PFA and Halar. Although the opacities of the tubing materials differed slightly, a correlation between percent conversion and refractive index as reported by the manufacturer could not be made, perhaps because of the difference in wavelength of light tested. The refractive index values were 1.340, 1.338, 1.400, and 1.447, for PFA, FEP, Tefzel, and Halar, respectively. Identical polymerization reactions utilizing the various tubing materials were evaluated to directly compare reactor performance. The light mediated polymerizations were conducted in a Rayonet Reactor light box equipped with 380 nm bulbs and a fan. Specifically, monomer conversion was measured at residence times of 55 minutes and 220 minutes (Figure 2.3).

Tubing (timepoint)	Oxygen Permeability[a]	Conv. (%)	M_n (g·mol^{-1})[b]	Đ[c]
PFA (55 min)	881	11	1500	1.21
PFA (220 min)	881	31	3300	1.23
FEP (55 min)	748	11	2000	1.24
FEP (220 min)	748	37	3500	1.15
Tefzel (55 min)	100	11	1000	1.25
Tefzel (220 min)	100	41	5300	1.24
Halar (55 min)	25	15	1400	1.24
Halar (220 min)	25	42	5400	1.21

Figure 2.3: Percent conversion of poly(methyl methacrylate) (theoretical M_n = 10,000 g $\cdot$ mol^{-1}) reported for four polymer tubes at residence times of 55 and 220 minutes.

Despite visual differences in reactor transparency, the results did show that a controlled polymerization could be achieved and after a residence time of 55 minutes, PFA, FEP, and Tefzel yield about 11% monomer conversion with Halar producing a conversion of 15%. Extending the irradiation time to 200 minutes showed more varied results with monomer conversions ranging from 31% for PFA to 42% for Halar. Narrow molecular weight distributions between 1.15 and 1.24 were obtained under all the conditions tested, indicating the polymerizations exhibited fast initiation and controlled behaviour under flow conditions. The data show a trend of higher monomer conversions for lower oxygen permeable tubing at longer residence times. This led us to speculate that oxygen diffusion through the reactor tubing, not its transparency to light, was the most important material property to consider for these light-mediated polymerizations under continuous flow conditions. Therefore, additional comparisons between PFA and Halar flow reactors were made to understand the role of oxygen permeability in the system.

We hypothesized that superior oxygen barrier properties were key to obtaining high conversions of monomer via a flow reactor, especially at longer reaction times when the greater surface-to-volume ratio of tubing becomes an important factor. In order to take full advantage of the polymerization rate enhancement under continuous flow conditions previously observed by others, a strip of LEDs was added to illuminate the tubing from the inside while the light box irradiated from the outside. The flow rates for polymerization were varied between 20 μL min^{-1} and 1.06 μL min^{-1} , corresponding to residence times of 25 and 500 minutes, respectively. Figure 2.4 and 2.5 compare monomer conversion versus residence time for identical polymerization reactions performed in either PFA or Halar tubing.

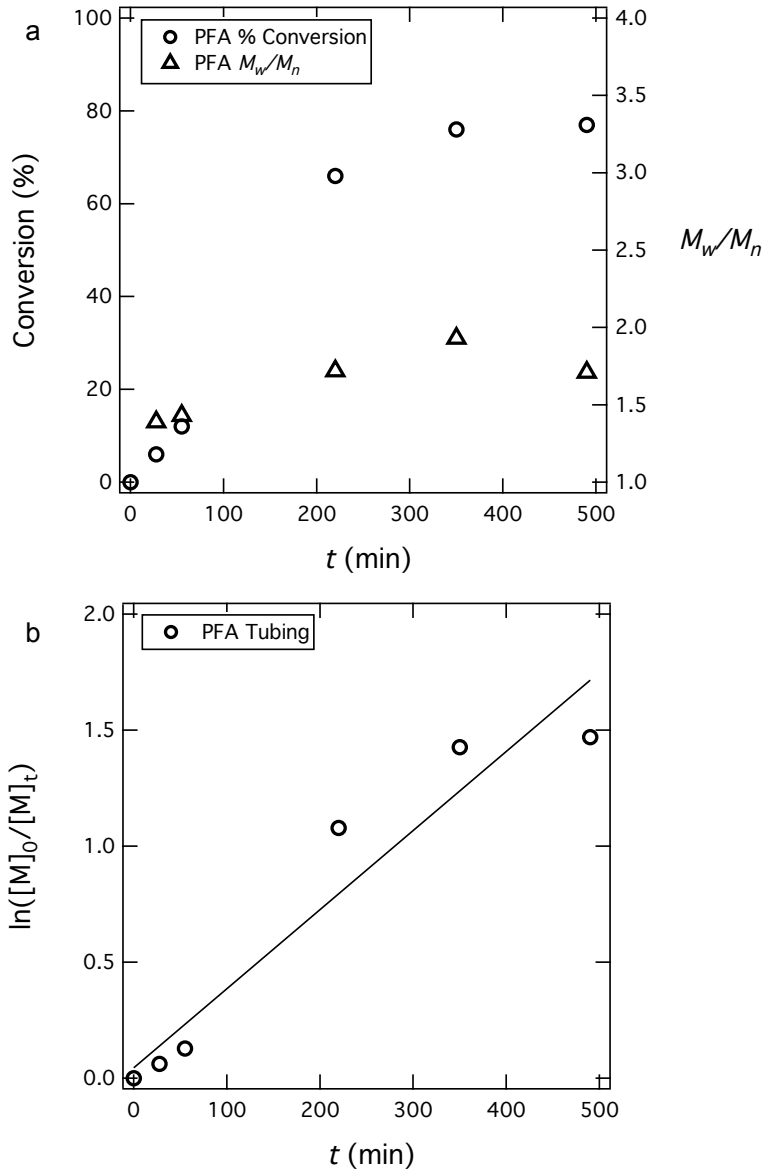

Figure 2.4: Plots showing the polymerization of MMA in a PFA tubing continuous flow reactor. In part a, the conversion and M_w/M_n (Đ) are shown versus time for PFA, where open triangles indicate dispersity and open circles indicate percent conversion. In part b, the linear plot of percent conversion is shown versus time, $\ln([M]_0/[M]_t)$ where $[M]_0$ and $[M]_t$ refer to concentration of the monomer at time zero and t. Data shown are from several experiments.

Significant improvements in performance were observed for reactor systems constructed from Halar, allowing for monomer conversions of greater than 80% after 450 minutes (Figure 2.5). While polymerizations performed in Halar tubing show a linear relationship and an r-squared value of 0.98 between $\ln([M]_0/[M]_t)$ and time, typical for controlled radical polymerizations, reactions in PFA tubing consistently deviated from linear behaviour, with a lower r-squared value, 0.92. In addition, after 200 minutes, polymerizations in PFA afforded broad molecular weight distributions, from 1.5-1.9 (Figure 2.4) with a plateau in molecular weight. This is presumably due to termination events caused by oxygen diffusion through the reactor material. It is important to note that there may be other important factors, like transparency to light and resistivity, which contribute to the superiority of Halar for light mediated flow reactions.

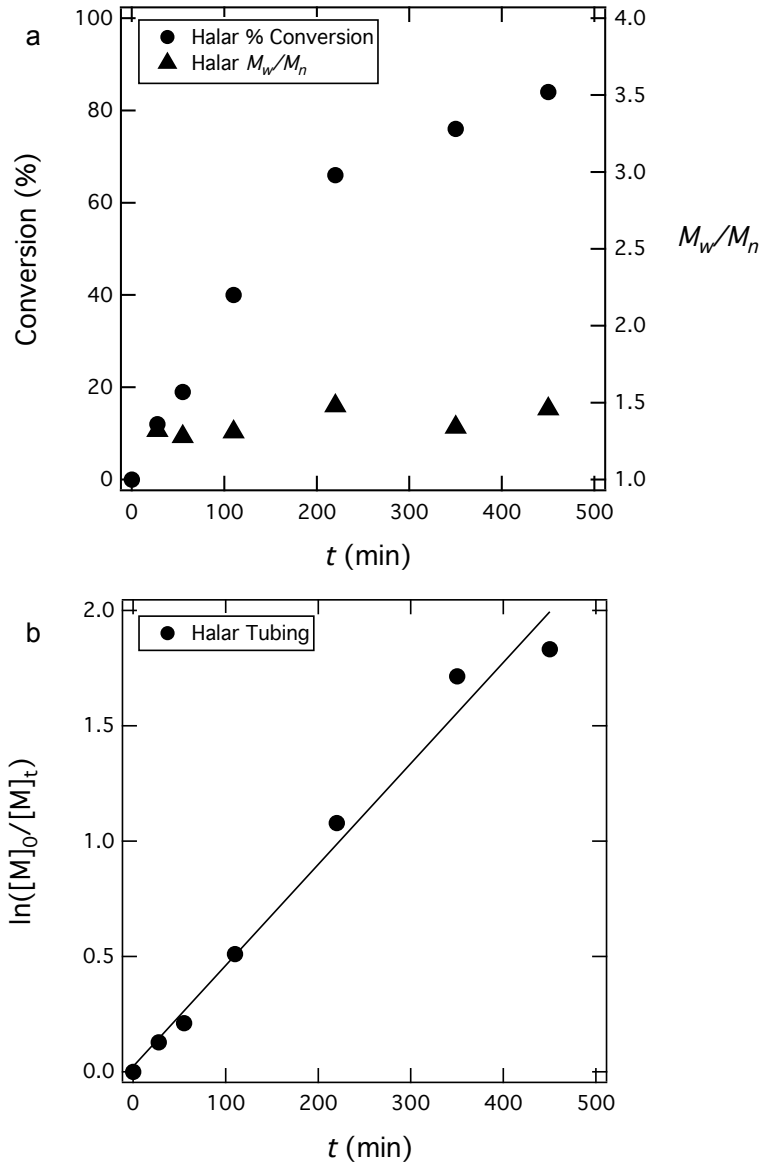

Figure 2.5: Plots showing the polymerization of MMA in a Halar tubing continuous flow reactor. In part a, the conversion and M_w/M_n (Đ) are shown versus time for Halar, where filled triangles indicate dispersity and filled circles indicate percent conversion. In part b, the linear plot of percent conversion is shown versus time, $\ln([M]_0/[M]_t)$ where $M]_0$ and $[M]_t$ refer to concentration of the monomer at time zero and t. Data shown are from several experiments.

The living nature of the light mediated polymerization under flow conditions is further supported by a linear evolution of molecular weight as shown in Figure 2.6. Size exclusion chromatography (SEC) traces plotted in Figure 2.6 show a clear trend towards shorter retention times with increasing reaction time while maintaining low molecular weight distributions. The number average molecular weights (M_n) were also found to increase linearly with monomer conversion as depicted in Figure 2.6.

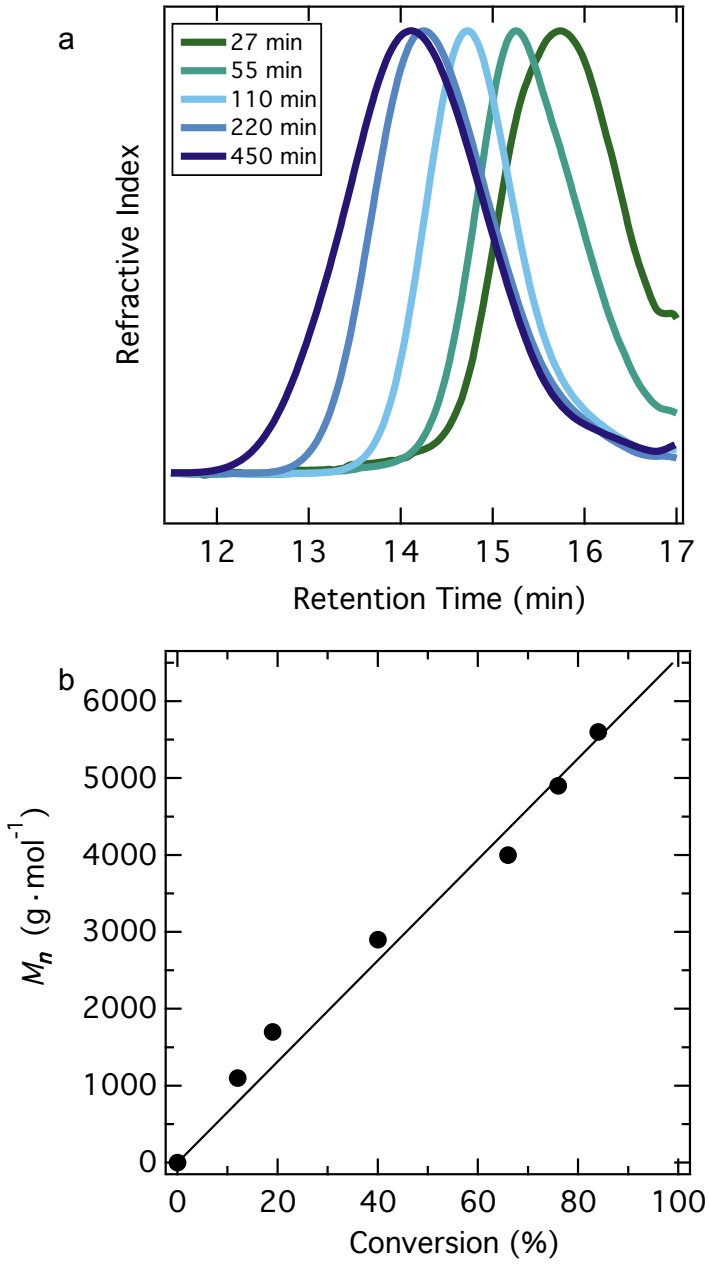

Figure 2.6: A target molecular weight study of 5 kg· mol^{-1} poly(methyl methacrylate) in Halar tubing. In part a, SEC traces show a decrease in retention time with increasing flow times; in part b, the molecular weight shows linear growth with increasing conversion. M_n was calculated by ^{1}H NMR as previously noted. All data shown are from a single kinetic experiment.

[M]/[I]	Conv. (%)[a]	M_n ($g \cdot mol^{-1}$) (theor.)	M_n ($g \cdot mol^{-1}$) (exp.)	Đ
50	45	2300	2300	1.11
50	62	3100	3000	1.16
50	84	4200	4500	1.34
100	24	2400	2700	1.20
100	42	4200	4400	1.33
100	68	6800	7500	1.43
150	12	1800	1900	1.20
150	24	3600	3800	1.08
150	30	4500	4400	1.09

[a] All experiments were run in the Halar continuous flow reactor.

Figure 2.7: The concentration of monomer to initiator ([M]/[I]) was varied and theoretical and experimental molecular weights were compared at different conversion.

We were also interested in exploring the robustness of the polymerization process for different monomer to initiator ratios. The crude reaction mixture was collected at three time points: 55 minutes, 110 minutes, and 220 minutes for a single reaction system and analyzed by GPC. Figure 2.7 shows good agreement between the experiment and theoretical molecular weights at different conversions for monomer to initiator concentration ratios of 50, 100 and 150:1. Notably, low dispersities (Đ) ranging from 1.09 to 1.34 were obtained for all of the conditions tested.

2.4 Comparison to Batch Reactions

Polymerization rates for the Halar flow reactor were then compared to traditional batch reactors in order to fully understand the efficiency and potential utility of flow systems for photo-mediated living radical procedures. Reactions were carried out in 20 mL scintillation vials as a prototypical batch reactor and compared with the Halar flow reactions using identical reactor volumes and irradiated for equal residence times. Figure 2.9 shows the natural log of the conversion versus time for the Halar reactor and batch reactor. From the line fits, there is a rate increase of at least 50% for the continuous flow setup, which is in agreement with what others have found when switching from batch reactors to flow reactors. A rationale is that in the flow system, even permeation of light throughout the entire reactor results in an increase in propagation rate and therefore a faster rate overall. This increase is obviously greater than any detrimental effects due to oxygen permeation. By contrast, the batch reactions are more susceptible to uneven and inefficient penetration of light, depending on the type of reaction vessel and orientation of the reaction setup. The high molar absorptivity of the reaction mixture due to the presence of the photoredox catalyst reduces the amount of light reaching the center of the vial thus slowing the rate of polymerization. This concept was demonstrated with a simple proof of concept experiment comparing monomer conversion at a specific time while modulating the intensity of light with neutral density filters (Figure 2.8).

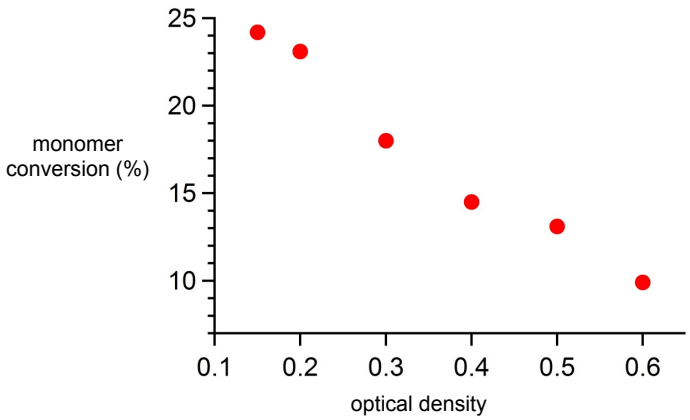

Figure 2.8: A plot showing monomer conversion versus optical density filters. The rate of polymerization was found to be first order with respect to the dose of light used for the polymerization reaction.

The rate of polymerization was found to be first order with respect to the dose of light used for the polymerization reaction. Figure 2.9 clearly illustrates that this effect can be observed in a traditional reaction setup and may be reduced by utilizing a flow reactor. In addition, our studies suggest a flow reactor could prove beneficial for the high throughput synthesis and functionalization of polymers compared to traditional procedures for light mediated polymerizations and reactions.

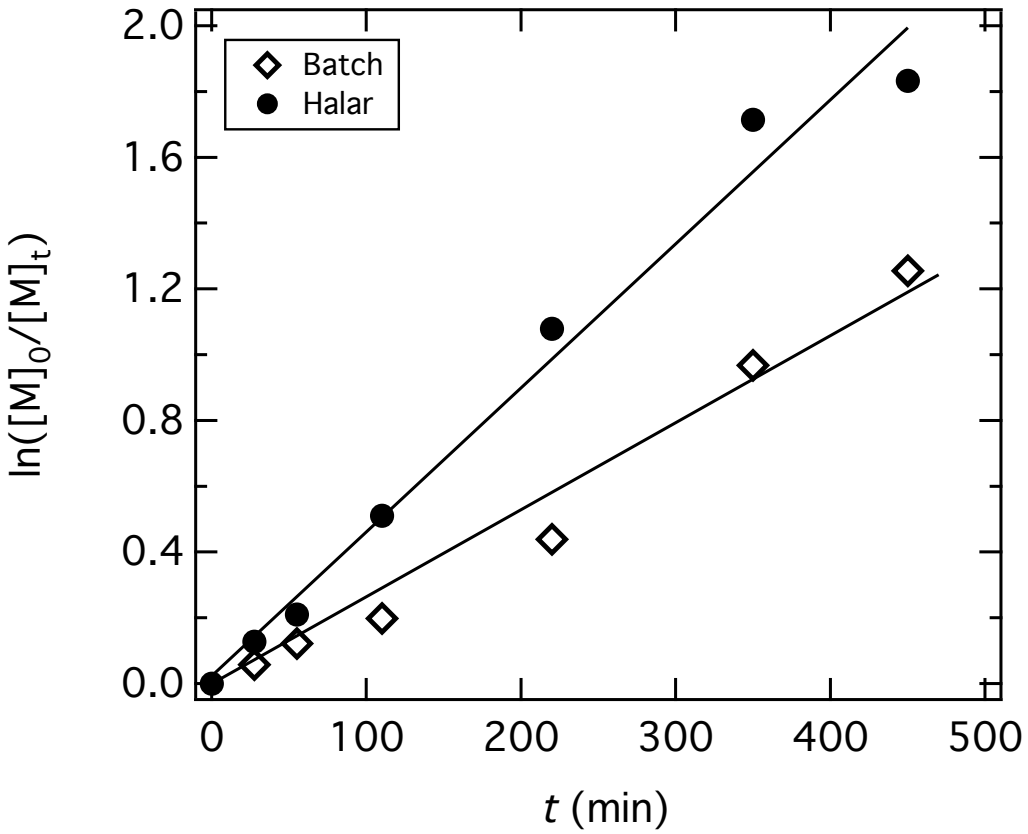

Figure 2.9: Polymerization of MMA in continuous flow Halar reactor (closed circles) compared with batch reactors (open diamonds) based on 20 mL scintillation vials. The continuous flow reaction shows 50% increased polymerization rate when compared to the corresponding batch systems using the same reaction conditions and light input. All batch reactions were performed without stirring. The percentage conversion is plotted linearly versus time, as $\ln([\mathrm{M}]_0/[\mathrm{M}]_t)$ where $[\mathrm{M}]_0$ and $[\mathrm{M}]_t$ refer to concentration of the monomer at t=0 and t.

2.5 Conclusions

We have optimized a continuous flow reactor based on Halar tubing for light mediated polymerizations. A combination of decreased oxygen permeability and increased transparency to visible light leads to significant improvement in polymerization efficiency. This continuous flow reactor system allows controlled molecular weight, low polydispersity materials to be prepared in a facile, user-friendly process. A number of advantages were observed when compared to traditional batch reactors including less waste and modularity.

Chapter 3

Poly(sulfur-*co*-myrcene): towards sustainable and scalable materials for next generation Li-S batteries

3.1 Motivations for Use of Sustainable Feedstocks

Recent work has shown the utility of sustainable feedstocks [11] as building blocks for making functional, commodity materials of scale. [45] One such starting material is sulfur, which is inexpensive, nontoxic, and readily available. The solvent-free copolymerization of waste elemental sulfur with a variety of monomers, termed inverse vulcanization due to the high feed ratio of sulfur, has shown promise in diverse applications [46, 47], such as water purification, [48] infrared optics, [49] and Li-S batteries. [50] In the latter application, sulfur has the potential to replace expensive and toxic intercalation Li-ion cathode materials. [51]

Li-S batteries have up to six times the theoretical capacity of Li-ion and could prove a major player in next-generation energy storage. However, sulfur batteries based on elemental sulfur are prone to suffer from polysulfide dissolution into the electrolyte during cycling, which results in a "shuttle phenomenon," thereby reducing capacity and battery cycling lifetime. [52] Many researchers have tried to address this problem by trapping the polysulfides in a matrix—through covalent bonding, [11, 53] adsorbed to conductive carbons, [54, 55] encapsulated inside TiO_2 shells, [56] or through polar-polar interactions with graphene oxide. [57] It is hypothesized that the formation of carbon-sulfur bonds through crosslinking enables the copolymer to repair and interact with carbon additives better than elemental sulfur on its own, [58] leading to improvements in both the conductivity and mechanical stability of Li-S batteries. Copolymerizing sulfur with an organic monomer [58, 59] can also improve the electrical conductivity of sulfur, as sulfur alone is highly insulating. Seminal work by Pyun et al. [45, 50, 60, 61, 62, 63, 64] inspired us to pursue a sulfur copolymer cathode material using a sustainably sourced terpene, myrcene, which has up to three reactive sites (Figure 3.1).

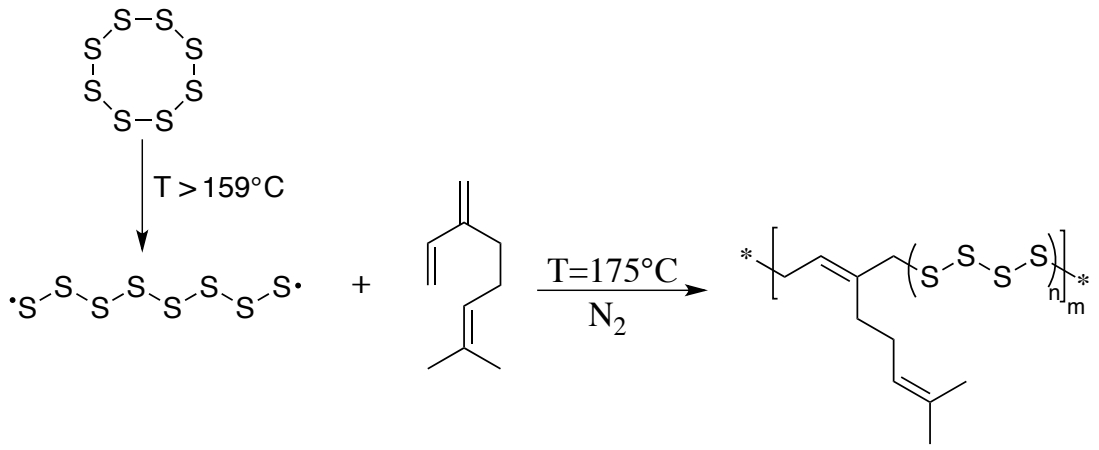

Figure 3.1: Myrcene and sulfur react at 175°C under nitrogen atmosphere to form a copolymer.

We report the first use of myrcene in a facile copolymerization with sulfur for application as the cathode material in Li-S batteries. While there are several studies on the reactions of terpenes with sulfur [65, 66, 67] none had yet explored their use in Li-S batteries to date in 2014, when this project was undertaken. Myrcene is a natural essential oil found in aromatic plants like thyme and derived in large quantities from nonedible biomass such as pine tree needles. [68, 69] It is a ten-carbon olefin containing a conjugated diene and an isopropylidene functionality. As such, it is a notably cheap and nontoxic starting material suitable for diverse polymerization pathways, [69] as outlined in Figure 3.3. Heat-activated ring opening of elemental sulfur above 159°C induces free radical polymerization through unsaturated bonds in alkenes and alkynes. [70] By varying the ratio of sulfur to co-monomer, it is possible to modify materials properties and ease of processing as solubility, mechanical properties, and conductivity all depend on sulfur content. [71] However, as carbons are added to the network in place of sulfur, the overall capacity of the battery drops as this is calculated based on electrons from sulfur. Accordingly, for battery applications the highest initial performance comes from high sulfur loading. The tricky part, therefore, is keeping this material from dissolving into the electrolyte as it reacts with Li+ ions and undergoes other deleterious side reactions. Additionally, the choice of co-monomer seems to have significant impact on the battery's performance, as described in this paper. Compared to other large, benzylic monomers widely used in crosslinking sulfur, myrcene contains three double bonds per 136 $g \cdot mol^{-1}$ (1,3-diisopropenylbenzene only has two double bonds per 158 $g \cdot mol^{-1}$). Myrcene also has a high boiling point (176°C), above the ring opening temperature of sulfur (159°C), which proves

useful for thermally activated polymerizations via inverse vulcanization, preventing material loss to evaporation during polymerization. The facile synthesis of sulfur copolymers from myrcene expands on the recognized sustainability of inverse vulcanization, especially as technical grade myrcene is suitable. Poly(sulfur-*co*-myrcene), abbreviated herein as S-Myr, was synthesized in varying ratios of sulfur to myrcene (90:10, 80:20 weight percent). Purification of the copolymers by washing with CS_2 removed soluble lower molecular weight fractions of the copolymer and any remaining unreacted S_8. The S-Myr copolymers were analyzed by thermal, spectroscopic, and electrochemical characterization: solid state NMR, infrared and Raman spectroscopy (FT-IR and Raman), differential scanning calorimetry (DSC), thermogravimetric analysis (TGA), X-ray photoelectron spectroscopy (XPS), and galvanostatic cycling (GCPL). In the latter method, the copolymers' performance was compared to elemental sulfur.

3.2 Synthesis and Methods

Materials Sulfur (reagent grade, sublimed, 100 mesh particle size, Sigma Aldrich) and 7-Methyl-3-methylene-1,6-octadiene (Myrcene, technical grade, Sigma Aldrich), and carbon disulfide (Sigma Aldrich) were used as received without further purification. The BHT inhibitor in myrcene was removed over a plug of alumina prior to use.

Instrumentation ^{1}H and ^{13}C nuclear magnetic resonance spectroscopy were performed on a 600MHz SB Varian VNMRs for solutions and 500MHz WB Bruker Avance NMR for solid materials, respectively. $CDCl_3$ was used as a standard for

solution experiments while a 4mm MAS double resonance broadband ^{1}H/X probe was used for the solid-state experiments with spinning at 10 THz. Thermogravimetric Analysis (TGA) was performed on a Discovery (TA Instruments) using a heating rate of 10°C per min from 25°C to 600°C, using nitrogen purge gas. Differential scanning calorimetry (DSC) was performed in crimped Al pans on a TA Instruments DSC, where data from three heating and cooling cycles were taken from -50°C to 150°C at a rate of 10°C per min. For DSC analysis, the first cycle was used to check for the elemental sulfur melt peak at 118°C, and the third heating cycle was used for analysis of the glass transition to remove thermal history. X-ray photoelectron spectroscopy (XPS) was performed using a Kratos Axis Ultra with a monochromatic Al Kα source (14.87 keV). Photoelectrons at 20 eV and 80 eV were detected with a multichannel detector. The spectra were fit in CasaXPS by a least-squares method to Voigt functions with Shirley baselines.

Synthesis of poly(sulfur-*co*-myrcene) Myrcene (Myr) was added neat in ratios of 10-20 weight percent to elemental sulfur at room temperature in a pre-polymerization mixing step. A typical 2 g scale reaction to make S-Myr 80:20 contained sulfur (1.6 g, 0.05 mol) and myrcene (0.5 mL, 0.4 g, 0.5 mol). After the reagents were combined, they were homogenized in a centrifugal mixer for 3 minutes to ensure even distribution prior to heating. The resulting smooth mixture was added to a 20 mL reaction vial equipped with a magnetic stir bar and purged with nitrogen for 10 minutes before being added to a thermostated silicone oil bath at 175°C. Within two minutes, the sulfur melted and separated from the organic top layer but with vigorous stirring the entire reaction mixture homogenized and turned a viscous dark orange with no layer separation. After seven minutes, the

mixture vitrified, evidenced by the stir bar losing speed. At this point the reaction vessel was removed from heat and immediately placed into powdered dry ice until frozen through. The material was either analyzed as prepared or subjected to purification with CS_2 washes. ^{13}C NMR poly(sulfur80wt%-*co*-myrcene20wt%) (400MHz, solid state MAS, δ): 136.8-122.9 (C=C), 59.2-51.5 (C-S) 44.2-17.3 (C-C). Elemental analysis: poly(sulfur80wt%-*co*-myrcene20wt%) Found: S, 88. IR: poly(sulfur-80wt%-*co*-myrcene20wt%): ν = 2963 (broad,-CH3), 2930 (broad, -CH2), 2884 (broad, -CH), 1663 (weak, C=C), 1448 (sharp, -CH2), 1383 (sharp, -CH3), 1330 (weak, =CH2), 1237 (weak), 1159 (weak), 1120 (sharp), 856 (broad), 780 (strong, C=C) cm^{-1}.

The copolymerization of sulfur and myrcene can be conducted in bulk at 175 °C due to the good solubility of myrcene in molten sulfur. The radical addition of sulfur diradicals formed at the elevated temperatures to the double bonds of myrcene is described schematically in Figure 3.3. Upon copolymerization, the reaction mixture solidifies, which is in agreement with previous literature on inverse vulcanization, [11] yielding a brown solid material (Figure 3.2).

Figure 3.2: Photo of poly(sulfur80wt%-*co*-myrcene20wt%), prepared on several grams scale.

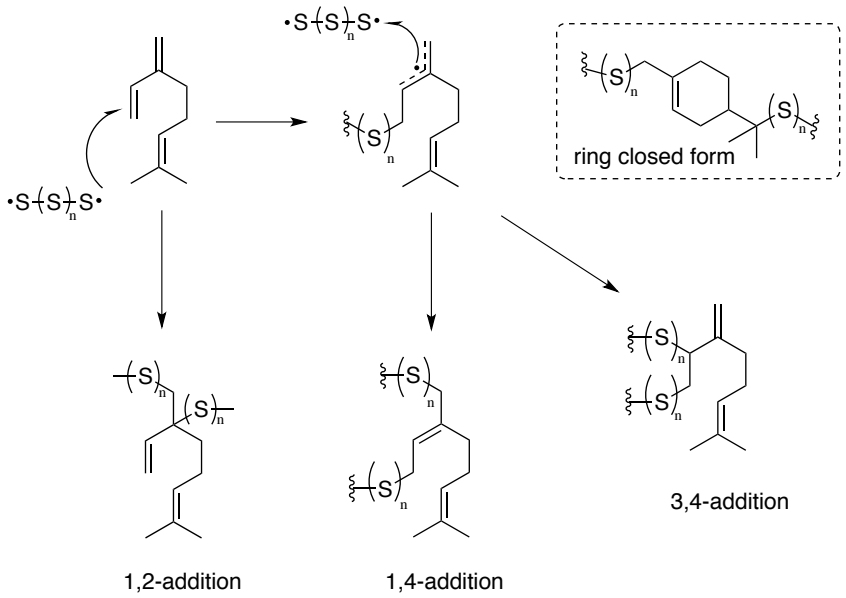

Figure 3.3: Schematic illustration of hypothetical reaction pathways for the inverse vulcanization of sulfur and myrcene forming poly(sulfur-*co*-myrcene).

Myrcene on its own is capable of forming several different homopolymers through the diene and can also undergo ring closure through the isopropylidene, resulting in 1,2-, 1,4-, and 3,4- additions and the ring-closed form, where reactivity is highly dependent on the polymerization conditions. [72, 73] Figure 3.3 shows a variety of sulfur additions to myrcene that were proposed before characterizing our copolymers. In actuality, a primary reaction pathway was found for poly(sulfur-*co*-myrcene) formed through inverse vulcanization. To rule out myrcene homopolymers forming from thermal activation, a kinetic study was conducted on myrcene under identical reaction conditions (175°C under N_2) and followed by ^{1}H NMR. No homopolymerization was discernable by heating the myrcene for double the reaction time used to polymerize sulfur and myrcene combined (Figure 3.4).

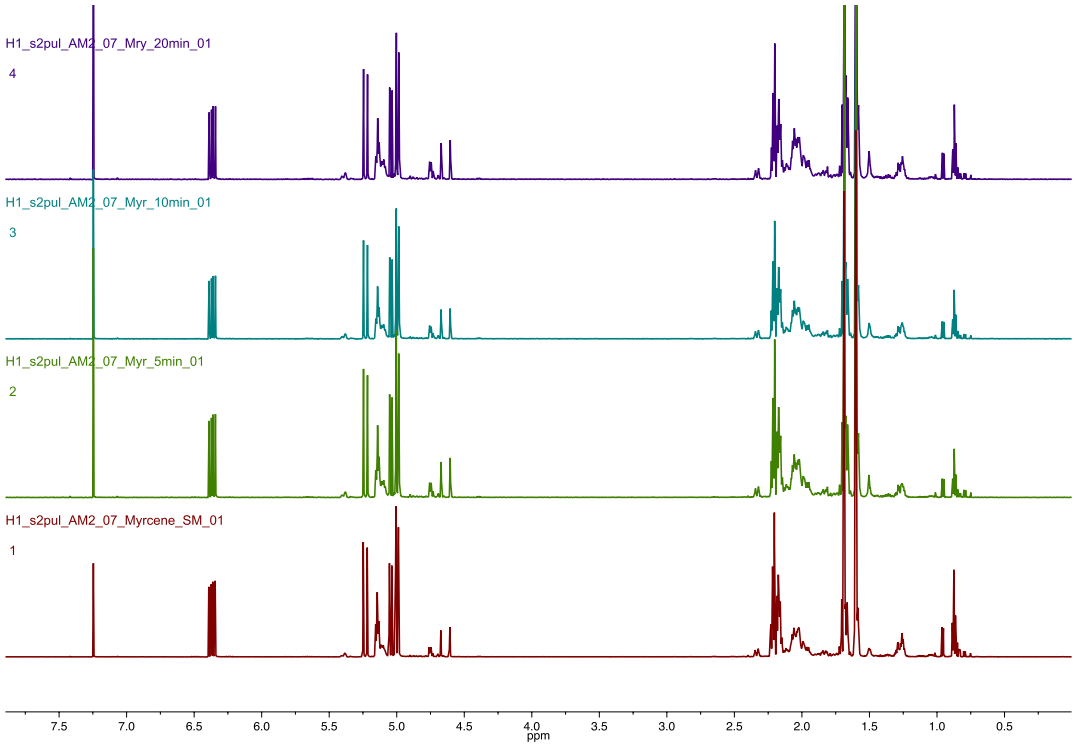

Figure 3.4: A kinetic study of neat myrcene heated at 175°C for 20 minutes. No homopolymerization was detected during this time frame, indicating that sulfur radicals were indeed driving the polymerization.

3.3 Characterization

FT-IR analysis provides some insight into the polymer structure (Figure 3.5). There is a near complete disappearance of the peak from the monomer to the polymers at 3096 cm^{-1}, a C=C-H stretch attributed to the hydrogen of sp^2 hybridized carbons of the diene. This indicates polymerization through 1,4-addition. [74] The sharp peak at 1596 cm^{-1}, absent in the polymers, is also identified as C=C double bonds of the diene. [74] Peak broadening from 2981 to 2870 cm^{-1} indicates the increase in the number of aliphatic -CH and -CH_2 bonds as the polymer forms. Disappearance of the sharp peak at 991 cm^{-1} from sp^2 C-H from the myrcene spectrum, indicative of sp^2 hybridized carbons on the monomer, signifies a consumption of alkenes. The peak at 844 cm^{-1} in the monomer spectrum, indicative of a tri-substituted alkene, shifts just slightly to 854 cm^{-1} in the polymer spectra, indicating that this bond is preserved in the final polymer. Raman spectroscopy confirms the polysulfide [75] nature of the copolymer, where the S-Myr 80:20 copolymer shows identifiable S-S bending modes at 213 $^{-1}$, 239 $^{-1}$ as well as several other peaks at 150, 205, 427, 458, 471 cm^{-1} (Figure 3.6), similar to those found in other sulfur copolymers. [48]

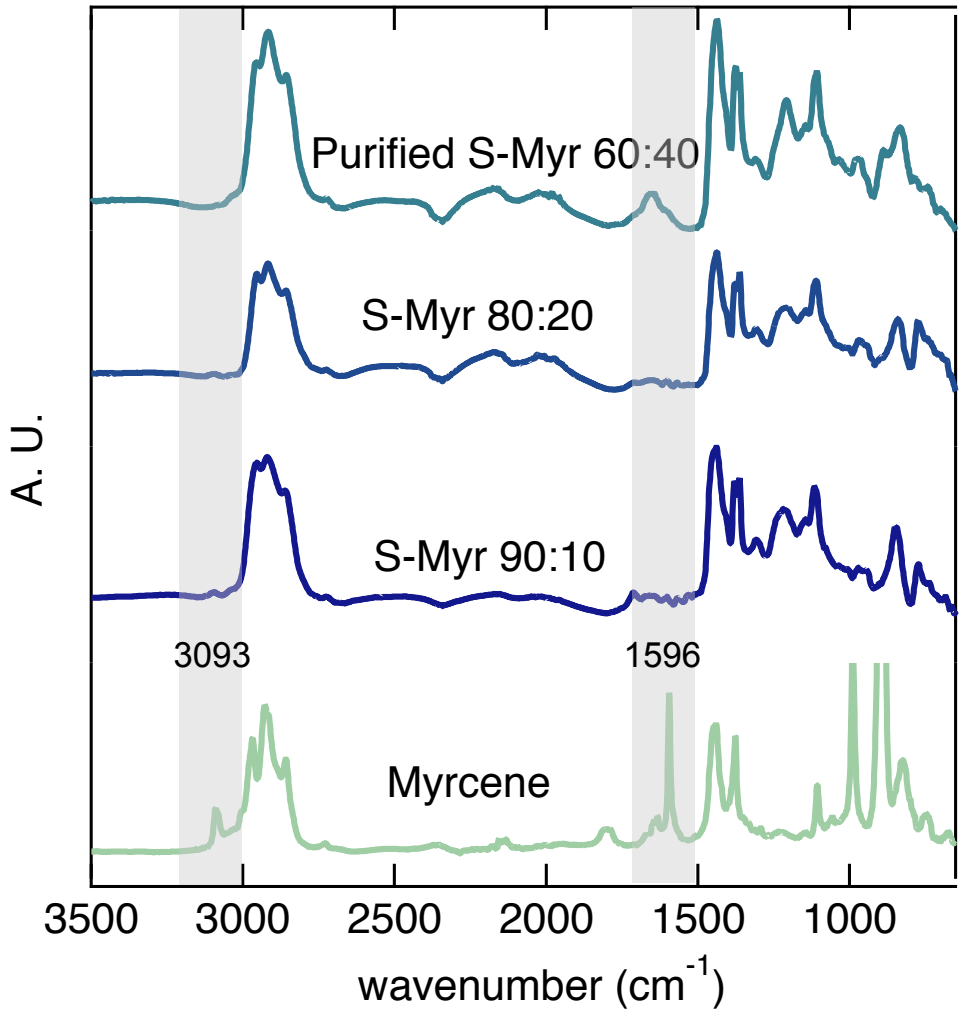

Figure 3.5: FT-IR Spectra of myrcene monomer and sulfur-myrcene copolymers.

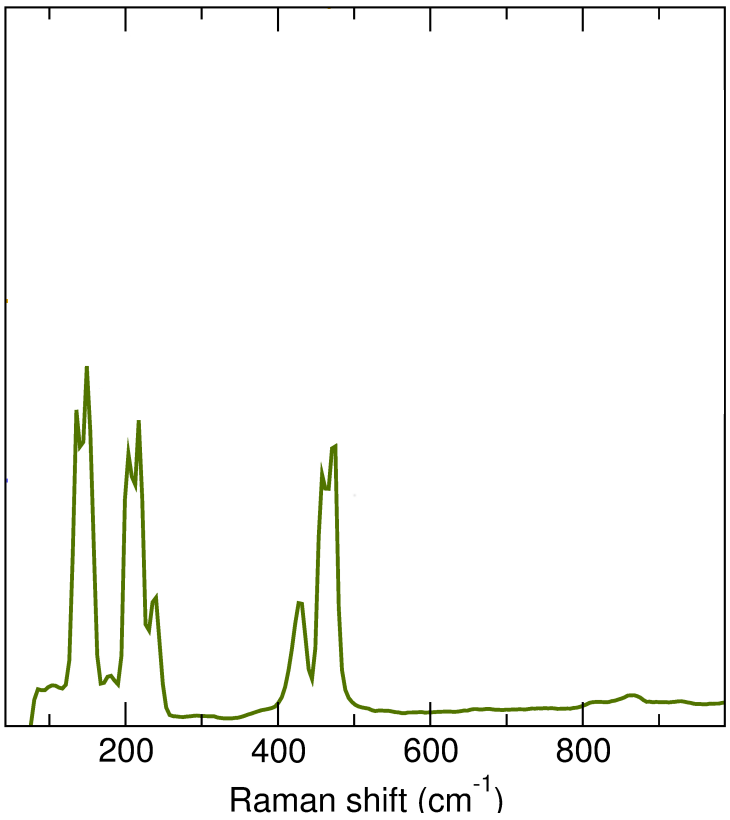

Figure 3.6: Raman spectrum of poly(sulfur80wt%-*co*-myrcene20wt%) from 0 to 1000 cm^{-1}.

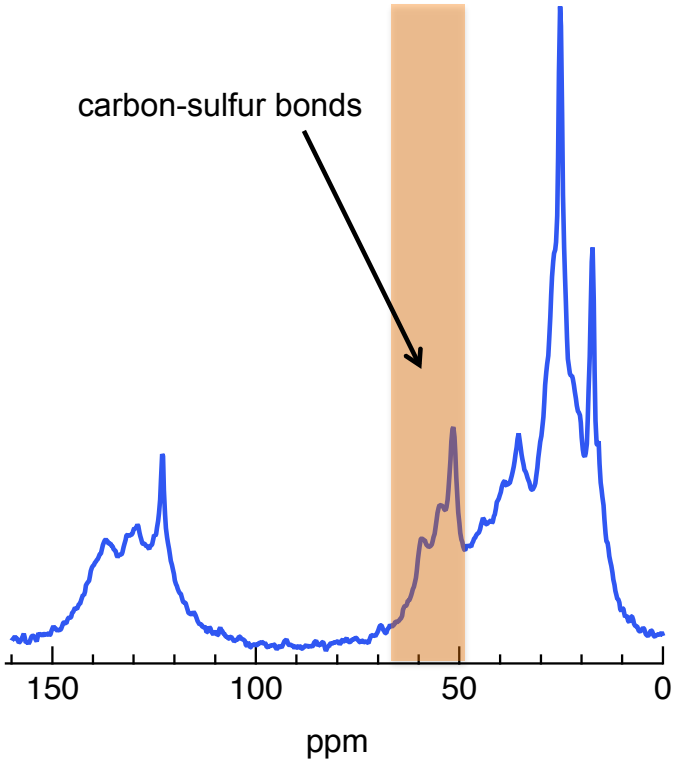

Figure 3.7: ^{13}C NMR spectrum of S-Myr 80:20.

Furthermore, solid state ^{13}C NMR with magic angle spinning confirms the formation of a sulfur-containing polymer due to the emergence of carbon-sulfur peaks in the 50-60 ppm region (Figure 3.7), where none had existed in the myrcene monomer spectrum (Figure 3.8).

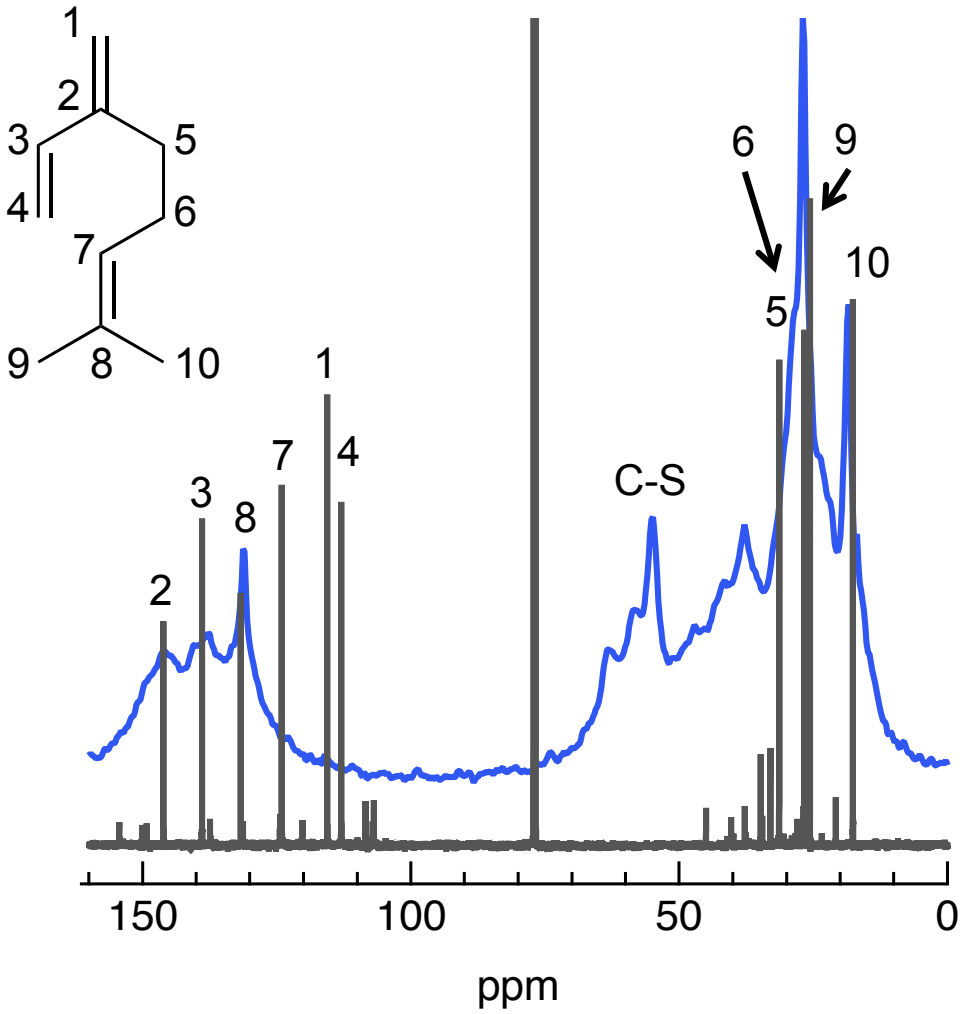

Figure 3.8: An overlay of the ^{13}C NMR of myrcene (grey) and poly(sulfur80wt%-*co*-myrcene20wt%) (blue).

Figure 3.7 shows three broad olefinic peaks in the range of 100-150 ppm due to unreacted double bonds incorporated in the S-Myr copolymer. The unreacted double bond signals are mainly ascribed to the sterically more hindered secondary and tertiary sp^2 hybridized carbons, whereas the signals of the primary sp^2 hybridized carbons disappear (see Figure 3.8). From this, 1,4-addition is likely the major reaction pathway, as previously reported. [72, 73, 75]

In the ^{13}C NMR of the myrcene starting material (Figure 3.8, it is possible to see ten major carbons, six in the olefinic region identified from highest ppm to lowest as C3, C8, C2, C7, C1, and C4 and four in the aliphatic region C5, C6, C9, and C10. In total, there are seven major peaks in the ^{13}C NMR spectrum of the polymer and several shoulder peaks, which are satellites. From the monomer to the polymer, the downfield olefin region changes from six peaks to a broad three, showing C3, C8, and C2/C7 overlapping. According to studies on poly(myrcene) isomers, the disappearance of C1 and C4 from the olefinic region could indicate a majority of 1,4- addition to the polymer. [72,73,75] Furthermore, the retention of a peak for C8 in the copolymer demonstrates the isopropylidene showing low affinity to crosslink with sulfur. Moreover, there are still signals near C2 and C3 in the olefinic region in the polymer spectrum. In the aliphatic region, there emerges a carbon sulfur bond region between 60-50 ppm with peaks found from 59.29, 51.57, followed by aliphatic peaks at 44.21, 38.92, 35.50, 26.60, and 17.37ppm. The ^{13}C NMR spectra of all copolymers were analogous regardless of purification.

Thermogravimetric analysis (TGA) and differential scanning calorimetry (DSC) were performed to understand the broader properties of the copolymers (Figure 3.9) and compared with literature compounds. From the TGA curves, it is possi-

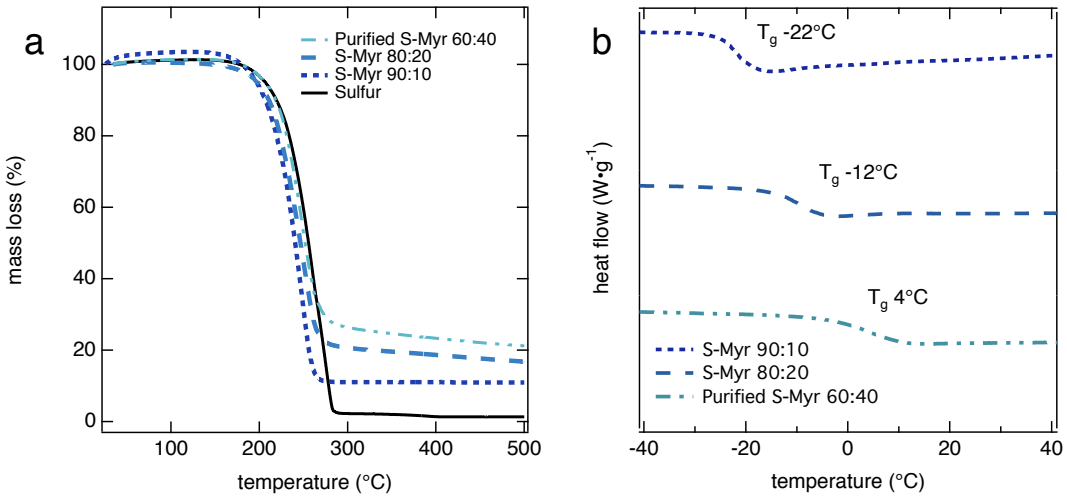

Figure 3.9: TGA (a) and DSC thermograms (b) for S-Myr copolymers. TGA experiments (a) were performed under nitrogen atmosphere. DSC traces (b), where the y axis is endo down, show Tg increases proportionally to organic content for 10, 20, and 40wt% myrcene. All three plots are staggered for ease of comparison. Purified S-Myr 60:40 refers to S-Myr 80:20 washed with CS_2.

ble to see a smooth one-stage thermal decomposition beginning around 200°C for all copolymers (Figure 3.9, part a). Less mass loss was found for the sulfur copolymers than elemental sulfur. Additionally, as the organic fraction of the copolymer increased, the mass loss decreased as expected. The DSC thermograms (Figure 3.9, part b) show glass transition temperatures (Tg) increasing with increasing organic moieties, analogous to results in the literature for other sulfur copolymers. At temperatures above 90°C, sulfur melting peaks (T_m) were observed in the DSC traces of S-Myr 80:20 (110°C) and S-Myr 90:10 (103°C) (Figure 3.10). Unreacted sulfur is typically observed for inverse vulcanization with low feed ratios of comonomers. [11]

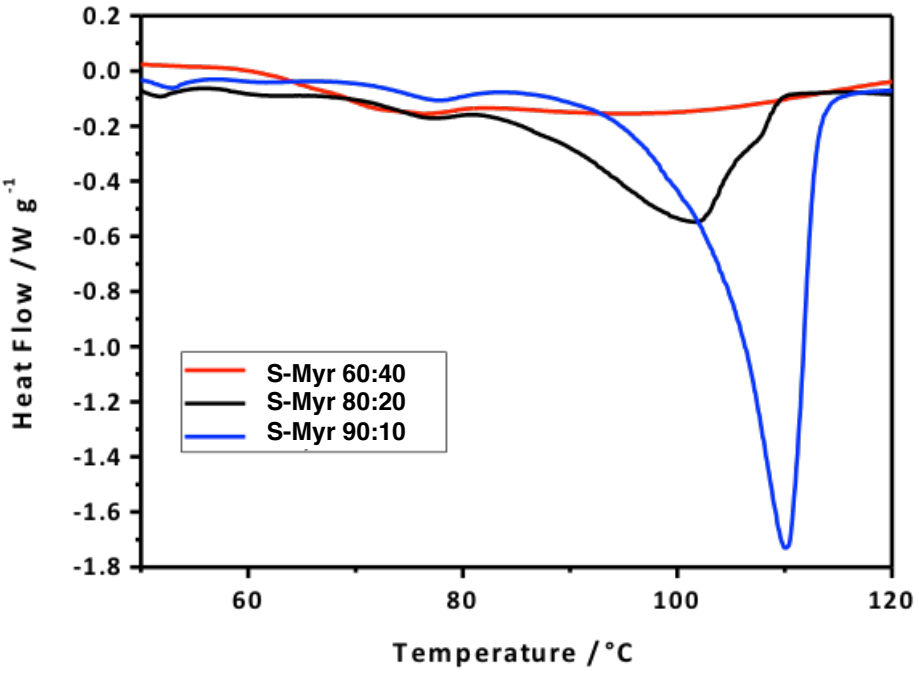

Figure 3.10: DSC thermograph showing the sulfur melt peak region for the three copolymers tested.

Purification to remove unbound sulfur Upon addition of the sulfur copolymer to the electrolyte (1,3-dioxolane and dimethoxyethane 1:1), it was possible to see a change in color from clear to light yellow (Figure 3.11), suspected to be unbound sulfur and low molecular weight organosulfur compounds. To avoid any active material from leaching into the battery while cycling, attempts were made to remove this unbound sulfur from the copolymers by extraction with carbon disulfide. The sulfur content of the purified material was analyzed by elemental analysis, DSC, and X-ray photoelectron spectroscopy (XPS). DSC curves of different purification methods were scrutinized for the disappearance of the sulfur melt peak (Figure 3.10) in the first heating cycle.

These results are in agreement with the XPS data in Figure 3.11. The experimental data was fitted with three S2p species: unreacted sulfur, S_8, sulfur bound to carbon ($S_{terminal}$), and sulfur incorporated in the S-Myr network with two sulfur neighbors ($S_{bridging}$). In both samples, the majority of the sulfur signal comes from internal S-S bonds, $S_{bridging}$ shown in blue. Upon washing with CS_2, the unreacted S_8 species present in S-Myr 80:20 (Figure 3.11, part b) disappears completely (Figure 3.11, part c). In Figure 3.11, part c, the dominance of $S_{bridging}$ signal indicates that all the polysulfides in this copolymer are contained within the polymer network and no unbound S_8 remains. The CS_2-extraction effectively removed unbound S_8 and low molecular weight organosulfur products, so that the S-Myr 80:20 was now relabeled as "purified S-Myr 60:40" to reflect the true carbon-to-sulfur composition of this copolymer as determined by elemental analysis.

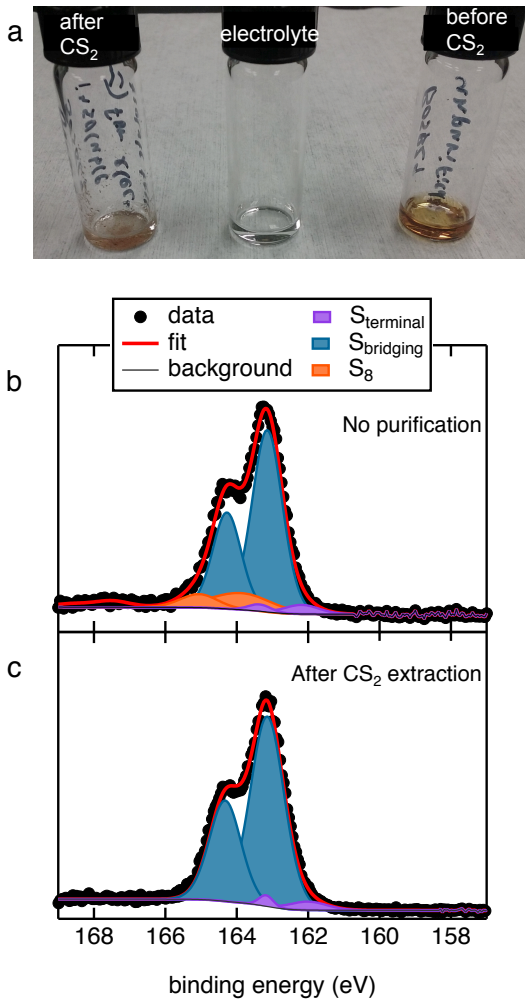

Figure 3.11: Solubility in electrolyte and purification study by XPS of S-Myr 80:20. In part a), a photo showing the solubility of the copolymers in the electrolyte, where the electrolyte does not color upon addition of CS_2-washed S-Myr copolymer (left) as it does for the unpurified S-Myr copolymer (right). In part b and c, S2p XPS spectra show purification treatment on sulfur-myrcene copolymers where b) shows unpurified S-Myr 80-20 and c) shows this same polymer after washing with CS_2.

3.4 Electrochemical Performance

Three copolymers, purified S-Myr 60:40 (Figure 3.11, part c), S-Myr 80:20 (Figure 3.11, part b), and S-Myr 90:10, were tested as the active material in Li-S coin cells for 100 cycles (Figure 3.13) and compared to an elemental sulfur reference cathode. Four cells of each copolymer and the sulfur reference were run to ensure reproducibility of the composite electrode and coin cell construction (Figure 3.12).

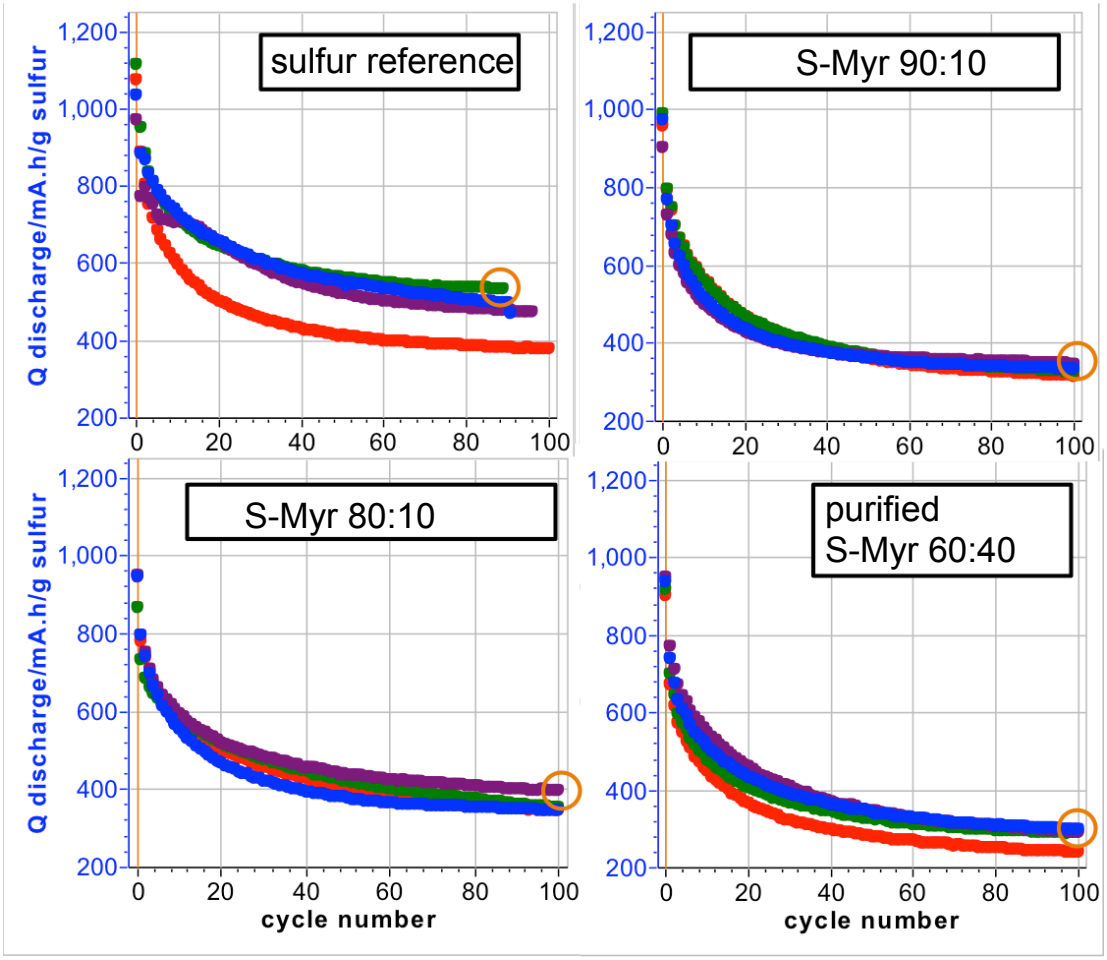

Figure 3.12: A plot showing four specific capacity versus cycle number for each polymer tested and the sulfur reference: Sulfur, S-Myr 90:10, S-Myr 80:20, purified S-Myr 60:40. Four coin cells were run of each material to ensure good reproducibility of the data.

The electrode composition for the battery tests was S-Myr:KB:CMC 55:35:10 and S:KB:CMC 55:35:10 for the reference. Galvanostatic cycling shown in Figure 3.13 was conducted at a rate of C/10 (1C is defined as 1675 $mA \cdot g^{-1}$). The initial charge capacities for the S-Myr 80:20, S-Myr 90:10 and purified S-Myr 60:40 were 895, 890 and 800 $mA \cdot g^{-1}$ respectively. These capacities faded within 100 cycles to 344, 334 and 300 $mA \cdot g^{-1}$, which corresponds to a capacity retention of 39%, 37%, and 36%. A comparable trend is observed for the sulfur reference, which performed marginally better. Beginning with an initial charge capacity of 1020 $mA \cdot g^{-1}$, over 100 cycles the capacity faded to only 380 $mA \cdot g^{-1}$, which corresponds to 37% capacity retention. The CS_2-washed copolymer was expected to perform better than the unpurified copolymers and elemental sulfur, in terms of lifetime and redox reversibility, because there was no apparent low molecular weight organosulfur compounds to leach into the electrolyte causing irreversible polysulfide dissolution and the shuttle phenomenon. Instead, this was quite different from what was found (Figure 3.13, part a). The sulfur copolymer with the best performance was S-Myr 80:20 while purified S-Myr 60:40 showed no enhancement in capacity fade. S-Myr 80:20 likely performed better than the higher sulfur loading S-Myr 90:10 due to greater homogeneity between sulfur and the comonomer.

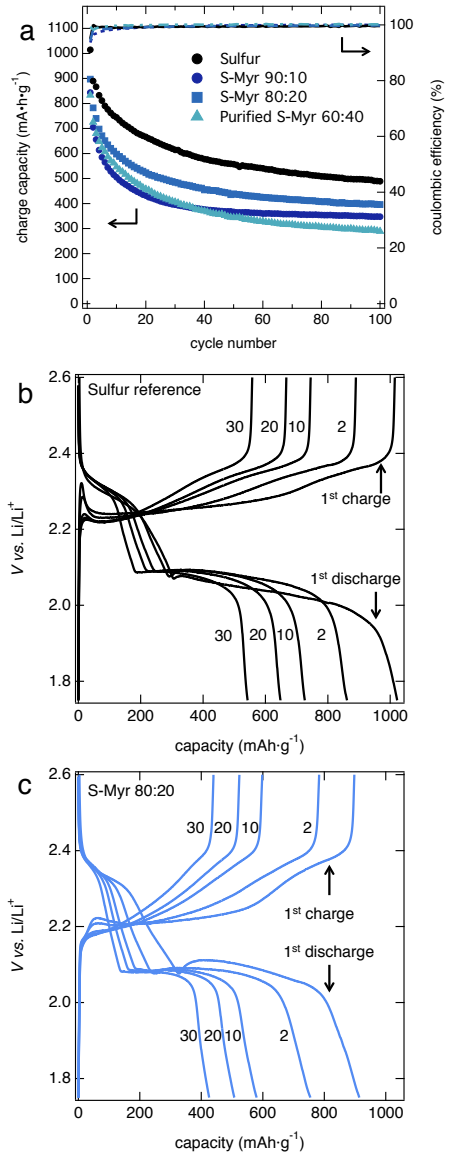

Figure 3.13: a) Galvanostatic cycling of S-Myr copolymers and the sulfur reference. Potential profiles of b) the sulfur reference and of c) the S-Myr 80:20 copolymer. The applied C-rate was C/10 and cutoff potentials were 1.7 V-2.6 V.

Notably, all of the copolymers performed worse than just using elemental sulfur on its own, although their decay occurred at a comparable rate (Figure 3.13, part a). This is in contrast to recent reports in the field of inverse vulcanization [62, 76, 77] for cathode materials: it appears that inverse vulcanization using myrcene as a comonomer does not result in improved battery performance. The potential profiles for S-Myr copolymers (Figure 3.13, part c) exhibit the features typical for sulfur cathodes (Figure 3.13, part b). The discharge-charge curves are generally similar in shape (Figure 3.13, b and c). The potentials for both plateaus were lower for the copolymers on first discharge. For the sulfur, these occur at 2.3V and 2.1V, and 2.2V and 2.0V for the sulfur copolymer. These plateaus are related to sulfur-sulfur chain scission, forming soluble polysulfides and finally the formation of insoluble discharge products including Li_2S. [78] Both plateaus have also been reported in the literature1 and show that inverse vulcanization alone does not prevent the dissolution of active material into the electrolyte. Furthermore, the plateau at 2.1 V in the first and subsequent cycles is much less pronounced for the copolymer, indicating that less insoluble discharge product is formed. The rapid capacity fade of both the sulfur reference electrode and the sulfur copolymer electrode could be related to the formation of irreversible products. XPS spectra of the cathodes after discharge showed similarities between the sulfur reference and the sulfur copolymers, indicating they underwent similar reactions with Li (Figure 3.14).

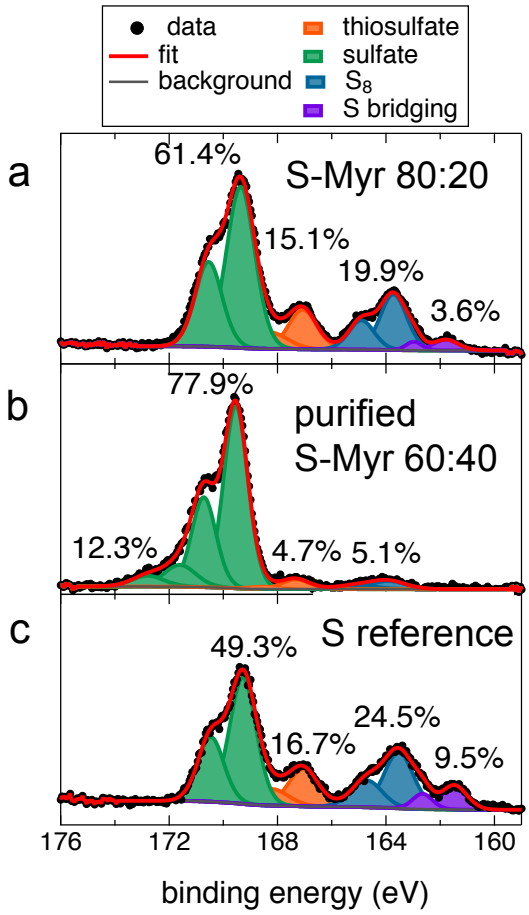

Figure 3.14: S2p XPS spectra after cycling for a) S-Myr 80:20, b) purified S-Myr 60:40, and c) the sulfur reference.

The electrochemical studies led us to important conclusions about the future of inverse vulcanization to address the shuttle phenomenon in Li-S batteries. The sulfur copolymers prepared here did not lead to a significant reduction in the shuttle phenomenon, in spite of our efforts to reduce any initial sulfur dissolution through purification of unbound sulfur with CS_2 extraction. The organosulfur compounds formed upon discharge did not act as a plasticizing agent, enabling reversible cycling, as hypothesized for poly(sulfur-*co*-1,3-diisopropenylbenzene). [50] Our results show that inverse vulcanization does not universally result in enhanced battery performance as conjectured in recent literature on inverse vulcanized material used in Li-S batteries. Ironically, the sulfur standard performed better than our copolymers, which goes against what has been surmised in the literature for other material obtained by inverse vulcanization. Indeed, it appears many other factors are at play than simply the formation of a carbon-sulfur network to develop next-generation Li-S batteries. [70] Moving forward, the choice of comonomer appears to be very crucial for battery performance. Further research is required to find correlations between comonomer structure and battery performance, to predict high performing inverse-vulcanized material for Li-S battery applications.

3.5 Conclusion

A sustainably sourced copolymer, poly(sulfur-*co*-myrcene), was synthesized via inverse vulcanization under solvent free conditions. The successful formation of the sulfur-containing copolymer was proven through FT-IR and NMR spectroscopy, and thermal studies showed similar properties to published sulfur copoly-

mers. Electrochemical studies of several poly(sulfur-*co*-myrcene) polymers were investigated and compared to elemental sulfur as the active material in Li-S coin cells. The copolymers behaved similarly to sulfur reference electrodes, indicating that inverse vulcanization is not a universal solution to the shuttle phenomenon in Li-S batteries, and other variables such as choice of comonomer, length of sulfur chain, and electrolyte additives are just as crucial to battery design.

Chapter 4

Accessing hexagonally packed cylinders morphology in diblock copolymers.

4.1 Introduction

New methodologies in polymer chemistry have enabled the preparation of discrete, monodisperse polymers with high chain-end fidelity through light mediated Cu ATRP. [9] Recent work has explored the use of fluorinated solvents to prepare acrylic and methacrylic polymers with a variety of side chain functionalities: hydrophobic, hydrophilic, and semi-fluroinated side chains. [79, 80, 81, 82, 83, 84, 85, 86, 87, 88] The work herein describes the combination of fluorinated solvent trifluoroethanol and light-mediated Cu ATRP to prepare low N diblock copolymers with an eye toward achieving interesting self-assembly behavior in bulk. Block

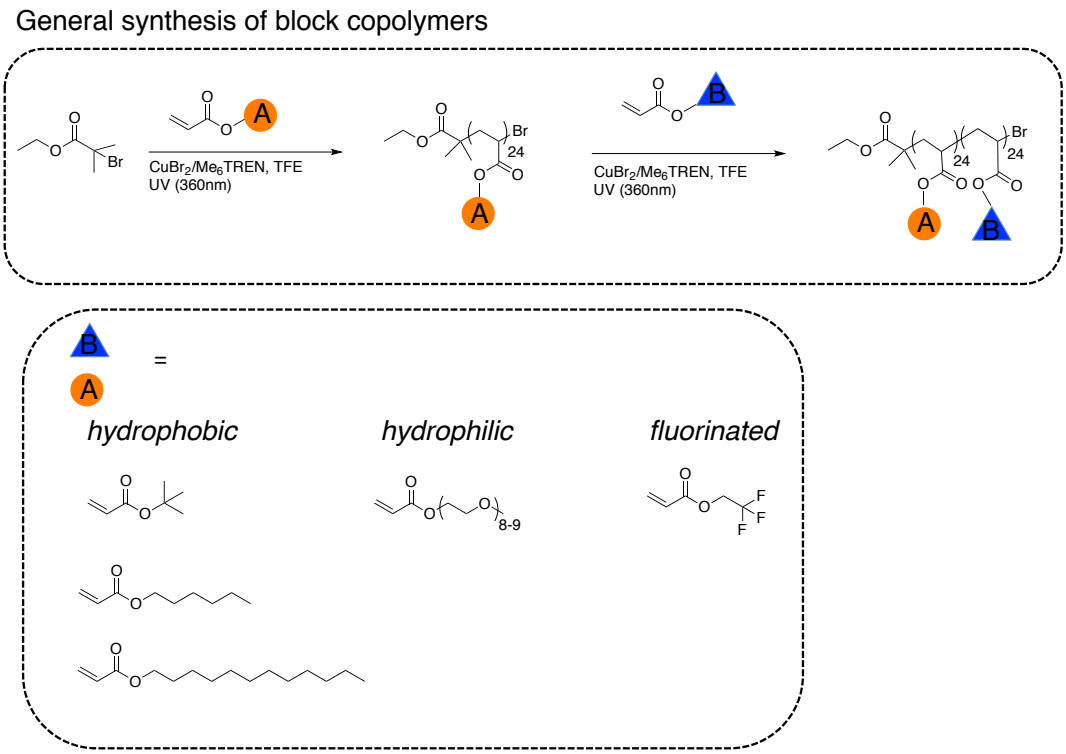

Figure 4.1: Synthetic scheme for the synthesis of the ten block copolymers.

copolymers have multiple potential and realized applications, not least in nanolithography, drug delivery, performance footwear, and therapeutics. For example, fluorinated diblock copolymers have applications as ^{19}F MRI agents [89] to track drug delivery *in vivo*.

A series of ten diblock copolymers with $N_{perblock} = 24$ were prepared using light-mediated Cu ATRP in trifluoroethanol and analyzed by Small Angle X-Ray Scattering for self-assembly behavior in bulk.

Diblocks were based on the following acrylic monomers: *tert*-butyl acrylate, hexyl acrylate, lauryl acrylate, trifluoro ethyl acrylate, and poly(ethylene glycol)$_{480}$ methyl ether acrylate. Degrees of polymerization of 24 were targeted for each block. A good comparison between length and bulkiness and chain length of the hydrophobic side chains (*tert*-butyl acrylate versus hexyl acrylate, linear C6, versus lauryl acrylate, linear C12) with the fluorinated and hydrophilic moieties permits a study of which hydrophobic monomer to select when designing materials that phase separate.

4.2 Materials and Methods

Poly(ethylene glycol)$_{480}$ methyl ether acrylate (PEGA),*tert*-butyl acrylate (tBA), hexyl acrylate (HA, 99%), and lauryl acrylate (referred to as LA or LAc, 99 %) were purchased from Sigma Aldrich and all but PEGA were passed through a column of basic alumina (150 mesh, Brockmann I grade) just prior to use. 2,2-trifluoroethyl acrylate (TFEA, 99%), copper(II) bromide ($CuBr_2$) (99 %), and tris[2 (dimethylamino)ethyl]amine (Me_6-TREN) (97 %) were purchased from TCI America and used as received. Ethyl-alpha bromoisobutyrate (Ebib, 98 %) was purchased from Sigma Aldrich. 2,2-trifluoroethanol (TFE, 99 %) and dichloromethane (DCM, Reagent Grade) were purchased from Fisher Scientific. Dialysis tubing (MWCO = 5-6 kD) was purchased from Spectral Por.

Nuclear magnetic resonance (NMR) spectra were recorded on a Varian 600 MHz spectrometer using $CDCl_3$ as the solvent to determine reaction completeness and number-average molar masses (M_n). Molar mass distributions (Đ=

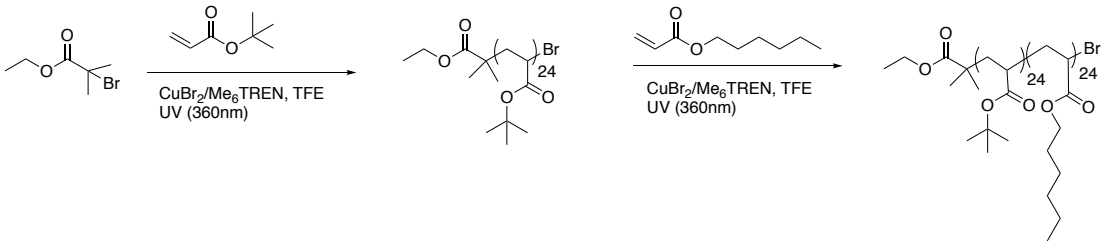

Figure 4.2: Synthetic scheme for the synthesis of $PtBA_{24}$-PHA_{24}

M_w/M_n) were measured via size exclusion chromatography (SEC), relative to linear polystyrene standards, on a Waters 2690 separation module equipped with Waters 2414 refractive index and 2996 photodiode array detectors. $CDCl_3$ containing 0.25 % triethylamine was used as the eluent at a flow rate of 1 mL $\cdot$ min^{-1}. Differential scanning calorimetry (DSC) was performed in crimped Al pans on a TA Instruments DSC, where data from three heating and cooling cycles were taken from -50°C to 150°C at a rate of 5°C or 10°C per min.

Synthesis of tBA_{24}-HA_{24}

For a target degree of polymerization = 24 per block, a typical reaction contained the following amounts of reagents, with equivalents relative to the initiator: 24 eq. tBA (1 mL, 6.8 mmol), 1 eq. Ebib (41.7 μL, 0.28 mmol), 0.02 eq. $CuBr_2$ (1.2 mg, 5.6 μmol), 0.12 eq. Me_6TREN (9.1 μL, 34.1 μmol), and 1 mL TFE (1:1 to the monomer). For the second block, additional catalyst/ligand/TFE solution was injected with the second monomer, containing: 24 eq. HA (1.2 mL, 6.8 mmol), 0.02 eq. $CuBr_2$ (1.2 mg, 5.6 μmol), 0.12 eq. Me_6TREN (9.1 μL, 34.1 μmol), and 0.6 mL TFE (50 vol% to monomer). Each reaction was prepared in the following way: $CuBr_2$, trifluoroethanol (TFE), and Me_6TREN were added to a glass reaction vial in that order and sonicated for several minutes until the mixture

turned a bright green color and all $CuBr_2$ was dissolved. To the solvent/catalyst mixture was added Ebib with microliter syringe, a stirbar, and finally capped with a rubber septum and degassed under N_2 for 5 minutes. Degassed monomer tBA was then added by syringe under N_2 atmosphere. The reaction vial was put under a UV nail curing lamp with stirring and allowed to react for up to 15 hours. At reaction completion as indicated by ^{1}H NMR, a solution containing HA and catalyst/ligand/TFE was degassed and injected into the vial. After 24 hours, the reaction was checked by ^{1}H NMR for complete monomer conversion and quenched by opening the vial to air. The reaction mixture was diluted in DCM, filtered over a column of basic alumina to remove the copper, and purified by dialysis (MWCO = 5000-6000) against DCM (1L) for several days, changing the DCM twice daily. The purified diblock copolymer was collected as a white, viscous material and analyzed by ^{1}H NMR, differential scanning calorimetry (DSC), and small angle x-ray scattering (SAXS). ^{1}H NMR (600 MHz, $CDCl_3$): δ 4.16 - 3.84 (m, 59H), 1.44 (qt, J = 5.9, 3.4 Hz, 215H), 1.13 (q, J = 5.2, 3.9 Hz, 6H). From the NMR, can conclude that $PtBA_{24}$-PHA_{29} resulted.

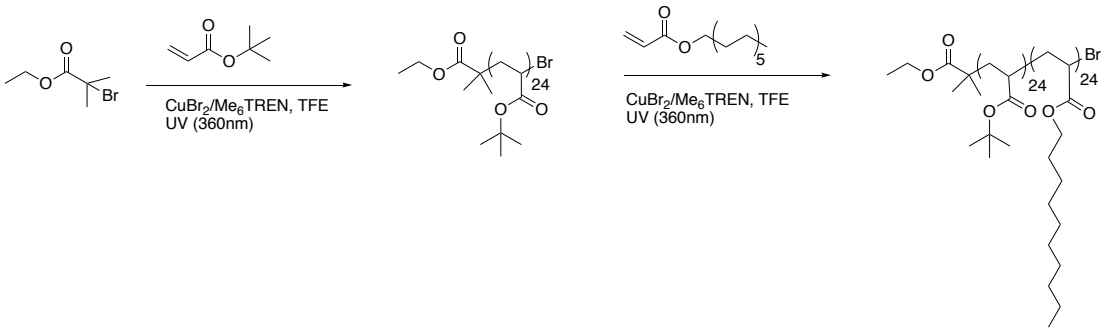

Figure 4.3: Synthetic scheme for the synthesis of $PtBA_{24}$-$PLAc_{24}$

Synthesis of tBA_{24}-LA_{24}

For a target degree of polymerization = 24 per block, a typical reaction contained the following amounts of reagents, with equivalents relative to the initiator: 24 eq. tBA (1 mL, 6.8 mmol), 1 eq. Ebib (41.7 μL, 0.28 mmol), 0.02 eq. $CuBr_2$ (1.2 mg, 5.6 μmol), 0.12 eq. Me_6TREN (9.1 μL, 34.1 μmol), and 1 mL TFE (1:1 to the monomer). For the second block, additional catalyst/ligand/TFE solution was injected with the second monomer, containing: 24 eq. LA (1.86 mL, 6.8 mmol), 0.02 eq. $CuBr_2$ (1.2 mg, 5.6 μmol), 0.12 eq. Me_6TREN (9.1 μL, 34.1 μmol), and 0.9 mL TFE (50 vol% to monomer). Each reaction was prepared in the following way: $CuBr_2$, trifluoroethanol (TFE), and Me_6TREN were added to a glass reaction vial in that order and sonicated for several minutes until the mixture turned a bright green color and all $CuBr_2$ was dissolved. To the solvent/catalyst mixture was added Ebib with microliter syringe, a stirbar, and finally capped with a rubber septum and degassed under N_2 for 5 minutes. Degassed monomer tBA was then added by syringe under N_2 atmosphere. The reaction vial was put under a UV nail curing lamp with stirring and allowed to react for up to 15 hours. At reaction completion as indicated by ^{1}H NMR, a solution containing LA and

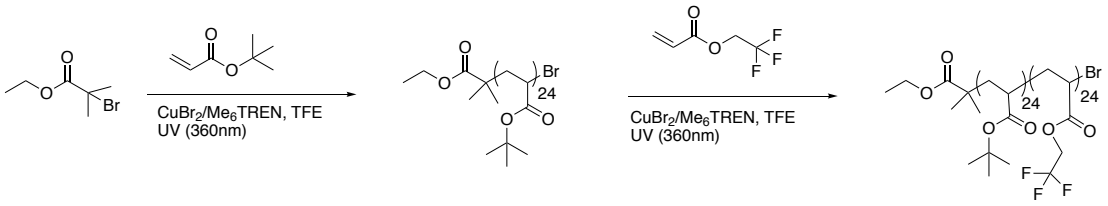

Figure 4.4: Synthetic scheme for the synthesis of $PtBA_{24}$-$PTFEA_{24}$

catalyst/ligand/TFE was degassed and injected into the vial. After 24 hours, the reaction was checked by ^{1}H NMR for complete monomer conversion and quenched by opening the vial to air. The reaction mixture was diluted in DCM, filtered over a column of basic alumina to remove the copper, and purified by dialysis (MWCO = 5000-6000) against DCM (1L) for several days, changing the DCM twice daily. The purified diblock copolymer was collected as a white, viscous material and analyzed by ^{1}H NMR, differential scanning calorimetry (DSC), and small angle x-ray scattering (SAXS). ^{1}H NMR (600 MHz, $CDCl_3$): δ 4.17 - 3.90 (m, 69H), 1.44 (d, J = 3.8 Hz, 244H), 1.14 (d, J = 7.1 Hz, 6H), 0.88 (t, J = 6.8 Hz, 95H). From the NMR, can conclude that $PtBA_{27}$-$PLAc_{34}$ resulted.

Synthesis of $PtBA_{24}$-$PTFEA_{24}$

For a target degree of polymerization = 24 per block, a typical reaction contained the following amounts of reagents, with equivalents relative to the initiator: 24 eq. tBA (1 mL, 6.8 mmol), 1 eq. Ebib (41.7 μL, 0.28 mmol), 0.02 eq. $CuBr_2$ (1.2 mg, 5.6 μmol), 0.12 eq. Me_6TREN (9.1 μL, 34.1 μmol), and 1 mL TFE (1:1 to the monomer). For the second block, additional catalyst/ligand/TFE solution was injected with the second monomer, containing: 24 eq. TFEA (0.87 mL, 6.8 mmol), 0.02 eq. $CuBr_2$ (1.2 mg, 5.6 μmol), 0.12 eq. Me_6TREN (9.1 μL, 34.1 μmol), and 0.6 mL TFE (50 vol% to monomer). Each reaction was prepared in

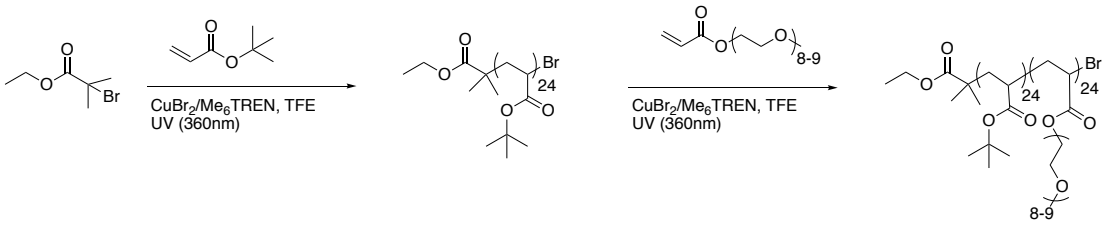

Figure 4.5: Synthetic scheme for the synthesis of $PtBA_{24}$-$PPEGA_{24}$

the following way: $CuBr_2$, trifluoroethanol (TFE), and Me_6TREN were added to a glass reaction vial in that order and sonicated for several minutes until the mixture turned a bright green color and all $CuBr_2$ was dissolved. To the solvent/catalyst mixture was added Ebib with microliter syringe, a stirbar, and finally capped with a rubber septum and degassed under N_2 for 5 minutes. Degassed monomer tBA was then added by syringe under N_2 atmosphere. The reaction vial was put under a UV nail curing lamp with stirring and allowed to react for up to 15 hours. At reaction completion as indicated by ^{1}H NMR, a solution containing TFEA and catalyst/ligand/TFE was degassed and injected into the vial. After 24 hours, the reaction was checked by ^{1}H NMR for complete monomer conversion and quenched by opening the vial to air. The reaction mixture was diluted in DCM, filtered over a column of basic alumina to remove the copper, and purified by dialysis (MWCO = 5000-6000) against DCM (1L) for several days, changing the DCM twice daily. The purified diblock copolymer was collected as a white, viscous material and analyzed by ^{1}H NMR, differential scanning calorimetry (DSC), and small angle x-ray scattering (SAXS). ^{1}H NMR (600 MHz, $CDCl_3$): δ 4.47 (s, 67H), 1.44 (d, J = 4.0 Hz, 257H), 1.13 (s, 6H). From the NMR, can conclude that $PtBA_{29}$-$PTFEA_{33}$ resulted.

Synthesis of $PtBA_{24}$-$PPEGA_{24}$

For a target degree of polymerization = 24 per block, a typical reaction contained the following amounts of reagents, with equivalents relative to the initiator: 24 eq. tBA (1 mL, 6.8 mmol), 1 eq. Ebib (41.7 μL, 0.28 mmol), 0.02 eq. $CuBr_2$ (1.2 mg, 5.6 μmol), 0.12 eq. Me_6TREN (9.1 μL, 34.1 μmol), and 1 mL TFE (1:1 to the monomer). For the second block, additional catalyst/ligand/TFE solution was injected with the second monomer, containing: 24 eq. PEGA (3.0 mL, 6.8 mmol), 0.02 eq. $CuBr_2$ (1.2 mg, 5.6 μmol), 0.12 eq. Me_6TREN (9.1 μL, 34.1 μmol), and 1.5 mL TFE (50 vol% to monomer). Each reaction was prepared in the following way: $CuBr_2$, trifluoroethanol (TFE), and Me_6TREN were added to a glass reaction vial in that order and sonicated for several minutes until the mixture turned a bright green color and all $CuBr_2$ was dissolved. To the solvent/catalyst mixture was added Ebib with microliter syringe, a stirbar, and finally capped with a rubber septum and degassed under N_2 for 5 minutes. Degassed monomer tBA was then added by syringe under N_2 atmosphere. The reaction vial was put under a UV nail curing lamp with stirring and allowed to react for up to 15 hours. At reaction completion as indicated by ^{1}H NMR, a solution containing PEGA and catalyst/ligand/TFE was degassed and injected into the vial. After 24 hours, the reaction was checked by ^{1}H NMR for complete monomer conversion and quenched by opening the vial to air. The reaction mixture was diluted in DCM, filtered over a column of basic alumina to remove the copper, and purified by dialysis (MWCO = 5000-6000) against DCM (1L) for several days, changing the DCM twice daily. The purified diblock copolymer was collected as a white, viscous material and analyzed by ^{1}H NMR, differential scanning calorimetry (DSC), and small angle

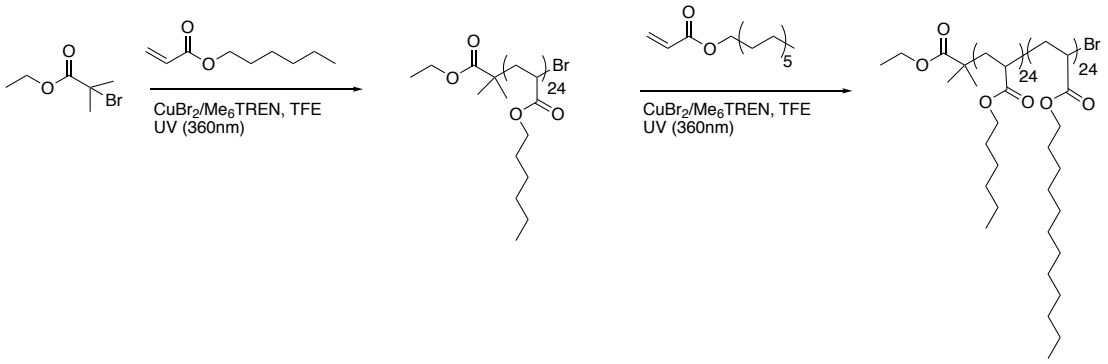

Figure 4.6: Synthetic scheme for the synthesis of PHA_{24}-$PLAc_{24}$

x-ray scattering (SAXS). ^{1}H NMR (600 MHz, $CDCl_3$): δ 3.37 (s, 83H), 1.50 - 1.37 (m, 229H), 1.13 (d, J = 5.9 Hz, 6H). From the NMR, can conclude that $PtBA_{25}$-$PPEGA_{28}$ resulted.

Synthesis of PHA_{24}-$PLAc_{24}$

For a target degree of polymerization = 24 per block, a typical reaction contained the following amounts of reagents, with equivalents relative to the initiator: 24 eq. HA (1 mL, 5.68 mmol), 1 eq. Ebib (34.8 μL, 0.236 mmol), 0.02 eq. $CuBr_2$ (1.1 mg, 4.74 μmol), 0.12 eq. Me_6TREN (7.6 μL, 28.42 μmol), and 1 mL TFE (1:1 to the monomer). For the second block, additional catalyst/ligand/TFE solution was injected with the second monomer, containing: 24 eq. LA (1.55 mL, 5.68 mmol), 0.02 eq. $CuBr_2$ (1.1 mg, 4.74 μmol), 0.12 eq. Me_6TREN (7.6 μL, 28.42 μmol), and 1 mL TFE (50 vol% to monomer). Each reaction was prepared in the following way: $CuBr_2$, trifluoroethanol (TFE), and Me_6TREN were added to a glass reaction vial in that order and sonicated for several minutes until the mixture turned a bright green color and all $CuBr_2$ was dissolved. To the solvent/catalyst mixture was added Ebib with microliter syringe, a stirbar, and finally capped with a rubber septum and degassed under N_2 for 5 minutes. Degassed monomer HA was then added by syringe under N_2 atmosphere. The reaction vial was put under a UV nail curing lamp with stirring and allowed to react for up to 15 hours. At reaction completion as indicated by ^{1}H NMR, a solution containing LA and catalyst/ligand/TFE was degassed and injected into the vial. Upon addition of the lauryl acrylate to the first block, the solution becomes very viscous and turns milky white. After 24 hours, the reaction was checked by ^{1}H NMR for complete monomer conversion and quenched by opening the vial to air. The reaction mixture was diluted in DCM, filtered over a column of basic alumina to remove the copper, and purified by dialysis (MWCO = 5000-6000) against DCM (1L) for several days, changing the DCM twice daily. The purified diblock copolymer was

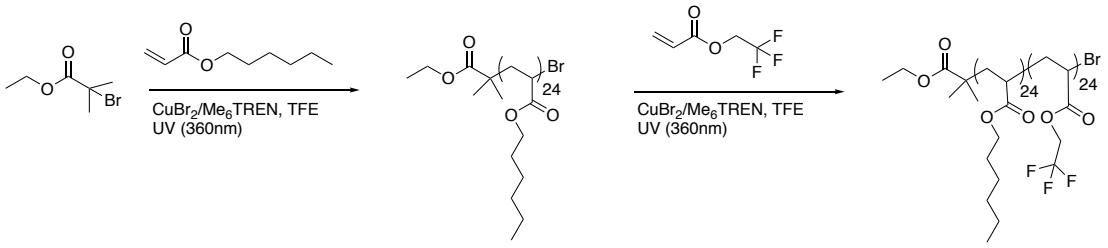

Figure 4.7: Synthetic scheme for the synthesis of PHA_{24}-$PTFEA_{24}$

collected as a white, viscous material and analyzed by ^{1}H NMR, differential scanning calorimetry (DSC), and small angle x-ray scattering (SAXS). ^{1}H NMR (600 MHz, $CDCl_3$): δ 4.18 - 3.85 (m, 109H), 1.17 - 1.08 (m, 6H). From the NMR, can conclude that PHA_{30}-$PLAc_{25}$ resulted. The integral of the polymer peak from the NMR of block 1 was subtracted from the NMR of both blocks to get individual DPs for each block, since the polymer peak overlaps in the diblock.

Synthesis of PHA_{24}-$PTFEA_{24}$

For a target degree of polymerization = 24 per block, a typical reaction contained the following amounts of reagents, with equivalents relative to the initiator: 24 eq. HA (1 mL, 5.68 mmol), 1 eq. Ebib (34.8 μL, 0.236 mmol), 0.02 eq. $CuBr_2$ (1.1 mg, 4.74 μmol), 0.12 eq. Me_6TREN (7.6 μL, 28.42 μmol), and 1 mL TFE (1:1 to the monomer). For the second block, additional catalyst/ligand/TFE solution was injected with the second monomer, containing: 24 eq. TFEA (0.72 mL, 5.68 mmol), 0.02 eq. $CuBr_2$ (1.1 mg, 4.74 μmol), 0.12 eq. Me_6TREN (7.6 μL, 28.42 μmol), and 0.6 mL TFE (50 vol% to monomer). Each reaction was prepared in the following way: $CuBr_2$, trifluoroethanol (TFE), and Me_6TREN were added to a glass reaction vial in that order and sonicated for several minutes until the mixture turned a bright green color and all $CuBr_2$ was dissolved. To the solvent/catalyst

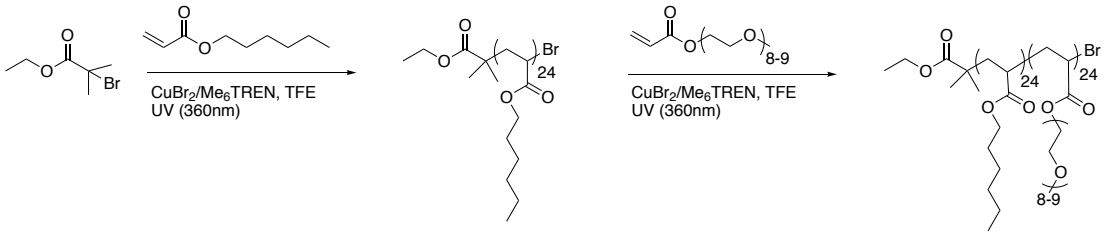

Figure 4.8: Synthetic scheme for the synthesis of PHA_{24}-$PPEGA_{24}$

mixture was added Ebib with microliter syringe, a stirbar, and finally capped with a rubber septum and degassed under N_2 for 5 minutes. Degassed monomer HA was then added by syringe under N_2 atmosphere. The reaction vial was put under a UV nail curing lamp with stirring and allowed to react for up to 15 hours. At reaction completion as indicated by ^{1}H NMR, a solution containing TFEA and catalyst/ligand/TFE was degassed and injected into the vial. After 24 hours, the reaction was checked by ^{1}H NMR for complete monomer conversion and quenched by opening the vial to air. The reaction mixture was diluted in DCM, filtered over a column of basic alumina to remove the copper, and purified by dialysis (MWCO = 5000-6000) against DCM (1L) for several days, changing the DCM twice daily. The purified diblock copolymer was collected as a white, viscous material and analyzed by ^{1}H NMR, differential scanning calorimetry (DSC), and small angle x-ray scattering (SAXS). ^{1}H NMR (600 MHz, $CDCl_3$): δ 4.62 - 4.33 (m, 55H), 4.17 - 3.81 (m, 46H), 1.18 - 1.04 (m, 6H). From the NMR, can conclude that PHA_{23}-$PTFEA_{27.5}$ resulted.

Synthesis of PHA_{24}-$PPEGA_{24}$

For a target degree of polymerization = 24 per block, a typical reaction contained the following amounts of reagents, with equivalents relative to the initiator:

24 eq. HA (1 mL, 5.68 mmol), 1 eq. Ebib (34.8 μL, 0.236 mmol), 0.02 eq. $CuBr_2$ (1.1 mg, 4.74 μmol), 0.12 eq. Me_6TREN (7.6 μL, 28.42 μmol), and 1 mL TFE (1:1 to the monomer). For the second block, additional catalyst/ligand/TFE solution was injected with the second monomer, containing: 24 eq. PEGA (2.50 mL, 5.68 mmol), 0.02 eq. $CuBr_2$ (1.1 mg, 4.74 μmol), 0.12 eq. Me_6TREN (7.6 μL, 28.42 μmol), and 1.5 mL TFE (50 vol% to monomer). Each reaction was prepared in the following way: $CuBr_2$, trifluoroethanol (TFE), and Me_6TREN were added to a glass reaction vial in that order and sonicated for several minutes until the mixture turned a bright green color and all $CuBr_2$ was dissolved. To the solvent/catalyst mixture was added Ebib with microliter syringe, a stirbar, and finally capped with a rubber septum and degassed under N_2 for 5 minutes. Degassed monomer HA was then added by syringe under N_2 atmosphere. The reaction vial was put under a UV nail curing lamp with stirring and allowed to react for up to 15 hours. At reaction completion as indicated by ^{1}H NMR, a solution containing PEGA and catalyst/ligand/TFE was degassed and injected into the vial. After 24 hours, the reaction was checked by ^{1}H NMR for complete monomer conversion and quenched by opening the vial to air. The reaction mixture was diluted in DCM, filtered over a column of basic alumina to remove the copper, and purified by dialysis (MWCO = 5000-6000) against DCM (1L) for several days, changing the DCM twice daily. The purified diblock copolymer was collected as a white, viscous material and analyzed by ^{1}H NMR, differential scanning calorimetry (DSC), and small angle x-ray scattering (SAXS). ^{1}H NMR (600 MHz, $CDCl_3$): δ 4.06 - 3.92 (m, 44H), 3.36 (s, 68H), 1.16 - 1.08 (m, 6H). From the NMR, can conclude that PHA_{22}-$PPEGA_{22}$ resulted.

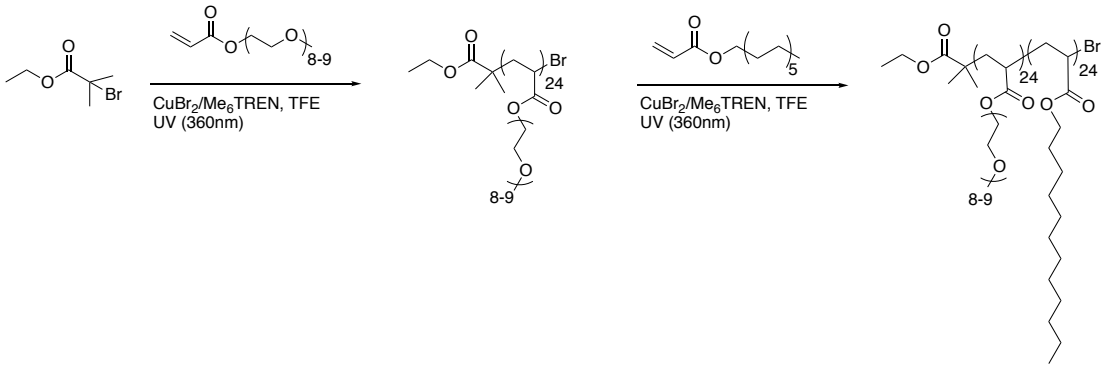

Figure 4.9: Synthetic scheme for the synthesis of $PPEGA_{24}$-$PLAc_{24}$

Synthesis of $PTFEA_{24}$-$PLAc_{24}$

Discussed in length in the subsequent chapter.

Synthesis of $PPEGA_{24}$-$PLAc_{24}$

For a target degree of polymerization = 24 per block, a typical reaction contained the following amounts of reagents, with equivalents relative to the initiator: 24 eq. PEGA (1 mL, 2.27 mmol), 1 eq. Ebib (13.8 μL, 0.0946 mmol), 0.02 eq. $CuBr_2$ (0.4 mg, 1.89 μmol), 0.12 eq. Me_6TREN (3.0 μL, 11.35 μmol), and 1 mL TFE (1:1 to the monomer). For the second block, additional catalyst/ligand/TFE solution was injected with the second monomer, containing: 24 eq. LA (0.62 mL, 2.27 mmol), 0.02 eq. $CuBr_2$ (0.4 mg, 1.89 μmol), 0.12 eq. Me_6TREN (3.0 μL, 11.35 μmol), and 0.5 mL TFE (50 vol% to monomer). Each reaction was prepared in the following way: $CuBr_2$, trifluoroethanol (TFE), and Me_6TREN were added to a glass reaction vial in that order and sonicated for several minutes until the mixture turned a bright green color and all $CuBr_2$ was dissolved. To the solvent/catalyst mixture was added Ebib with microliter syringe, a stirbar, and finally capped with a rubber septum and degassed under N_2 for 5 minutes.

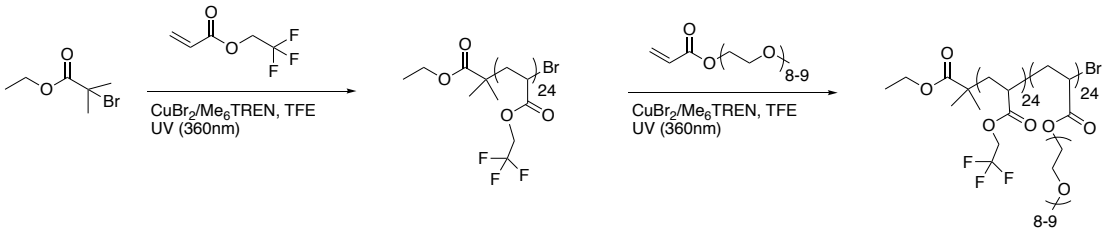

Figure 4.10: Synthetic scheme for the synthesis of $PTFEA_{24}$-$PPEGA_{24}$

Degassed monomer PEGA was then added by syringe under N_2 atmosphere. The reaction vial was put under a UV nail curing lamp with stirring and allowed to react for up tp 15 hours. The first block resulted in a very viscous white solution, but solubility was good as the PEGA polymer helped to solubilize the lauryl acrylate monomer during reaction. Simply swirling the solution together after addition of lauryl acrylate was sufficient, and ensuring good stirring during the reaction. At reaction completion as indicated by ^{1}H NMR, a solution containing LA and catalyst/ligand/TFE was degassed and injected into the vial. After 24 hours, the reaction was checked by ^{1}H NMR for complete monomer conversion and quenched by opening the vial to air. The reaction mixture was diluted in DCM, filtered over a column of basic alumina to remove the copper, and purified by dialysis (MWCO = 5000-6000) against DCM (1L) for several days, changing the DCM twice daily. The purified diblock copolymer was collected as a white, viscous material and analyzed by ^{1}H NMR, differential scanning calorimetry (DSC), and small angle x-ray scattering (SAXS). ^{1}H NMR (600 MHz, $CDCl_3$): δ 3.97 (dd, J = 19.6, 10.9 Hz, 48H), 3.38 (s, 68H), 1.13 (d, J = 11.7 Hz, 6H). From the NMR, can conclude that $PPEGA_{23}$-$PLAc_{24}$ resulted.

Synthesis of $PTFEA_{24}$-$PPEGA_{24}$

For a target degree of polymerization = 24 per block, a typical reaction con-

tained the following amounts of reagents, with equivalents relative to the initiator: 24 eq. TFEA (1 mL, 7.89 mmol), 1 eq. Ebib (48.2 μL, 0.328 mmol), 0.02 eq. $CuBr_2$ (1.4 mg, 6.57 μmol), 0.12 eq. Me_6TREN (10.5 μL, 39.45 μmol), and 1 mL TFE (1:1 to the monomer). For the second block, additional catalyst/ligand/TFE solution was injected with the second monomer, containing: 24 eq. PEGA (3.47 mL, 2.27 mmol), 0.02 eq. $CuBr_2$ (1.4 mg, 6.57 μmol), 0.12 eq. Me_6TREN (10.5 μL, 39.45 μmol), and 2.0 mL TFE (50 vol% to monomer). Each reaction was prepared in the following way: $CuBr_2$, trifluoroethanol (TFE), and Me_6TREN were added to a glass reaction vial in that order and sonicated for several minutes until the mixture turned a bright green color and all $CuBr_2$ was dissolved. To the solvent/catalyst mixture was added Ebib with microliter syringe, a stirbar, and finally capped with a rubber septum and degassed under N_2 for 5 minutes. Degassed monomer TFEA was then added by syringe under N_2 atmosphere. The reaction vial was put under a UV nail curing lamp with stirring and allowed to react for up to 15 hours. At reaction completion as indicated by ^{1}H NMR, a solution containing PEGA and catalyst/ligand/TFE was degassed and injected into the vial. After 24 hours, the reaction was checked by ^{1}H NMR for complete monomer conversion and quenched by opening the vial to air. The reaction mixture was diluted in DCM, filtered over a column of basic alumina to remove the copper, and purified by dialysis (MWCO = 5000-6000) against DCM (1L) for several days, changing the DCM twice daily. The purified diblock copolymer was collected as a white, viscous material and analyzed by ^{1}H NMR, differential scanning calorimetry (DSC), and small angle x-ray scattering (SAXS). ^{1}H NMR (600 MHz, $CDCl_3$): δ 4.27 - 4.02 (m, 52H), 3.36 (s, 64H), 1.21 - 1.07 (m, 6H).

From the NMR, can conclude that $PTFEA_{26}$-$PPEGA_{22}$ resulted.

4.3 Results and Discussion

The diblock copolymers were synthesized with attention to high conversion and reaction completion, to ensure no block mixing. A characterization summary is shown in tabular form in Figure 4.11. From the NMRs, degrees of polymerization were close to 24, with a degree of error ± 10. The real degrees of polymerization calculated by NMR are: $PTFEA_{26}$-$PPEGA_{22}$, $PPEGA_{23}$-PLA_{24}, PHA_{22}-$PPEGA_{22}$, PHA_{23}-$PTFEA_{27.5}$, PHA_{30}-PLA_{25}, $PtBA_{25}$-$PPEGA_{28}$, $PtBA_{29}$-$PTFEA_{33}$, $PtBA_{27}$-PLA_{34}, $PtBA_{24}$-PHA_{29}. For ease of comparison, the target degrees of polymerization will be labeled on subsequent discussion of the diblock copolymers. GPC traces of each reaction are including in the following discussion.

Polymer$_{\text{DP target}}$	**M**$_{\text{n(theor.) block A, blockB}}$	**M**$_{\text{n(GPC)}}$	**Đ**$_{\text{block A,block B}}$	**Self assembly**
tBA_{24}-HA_{24}	3.2K, 6.9K	3.5K, 7.5K	1.09,1.08	No
tBA_{24}-LA_{24}	3.3K, 9.2K	3.3K, 8.2K	1.09, 1.10	No
tBA_{24}-$TFEA_{24}$	3.2K, 6.9K	3.1K, 7.9K	1.10, 1.07	No
tBA_{24}-$PEGA_{24}$	3.2K, 14.7K	3.2K, 13.2K	1.09, 1.10	Disordered
HA_{24}-LA_{24}	3.9K, 9.7K	3.3K, 7.8K	1.10, 1.14	No
HA_{24}-$TFEA_{24}$	3.9K, 7.6K	3.3K, 6.8K	1.10, 1.05	Disordered
HA_{24}-$PEGA_{24}$	3.9K, 15.5K	3.2K, 11.5K	1.09, 1.12	Hex
$TFEA_{24}$-LA_{24}	3.8K, 9.6K	2.6K, 7.0K	1.09, 1.14	A15 + Hex
$PEGA_{24}$-LA_{24}	11.7K, 17.4	8.8, 13K	1.13, 1.16	Hex
$TFEA_{24}$-$PEGA_{24}$	3.8K, 15.4K	2.6K, 13.6K	1.10, 1.10	No

Figure 4.11: Table showing molar masses, polydispersities, and identified self--assembly behavior of the ten diblocks

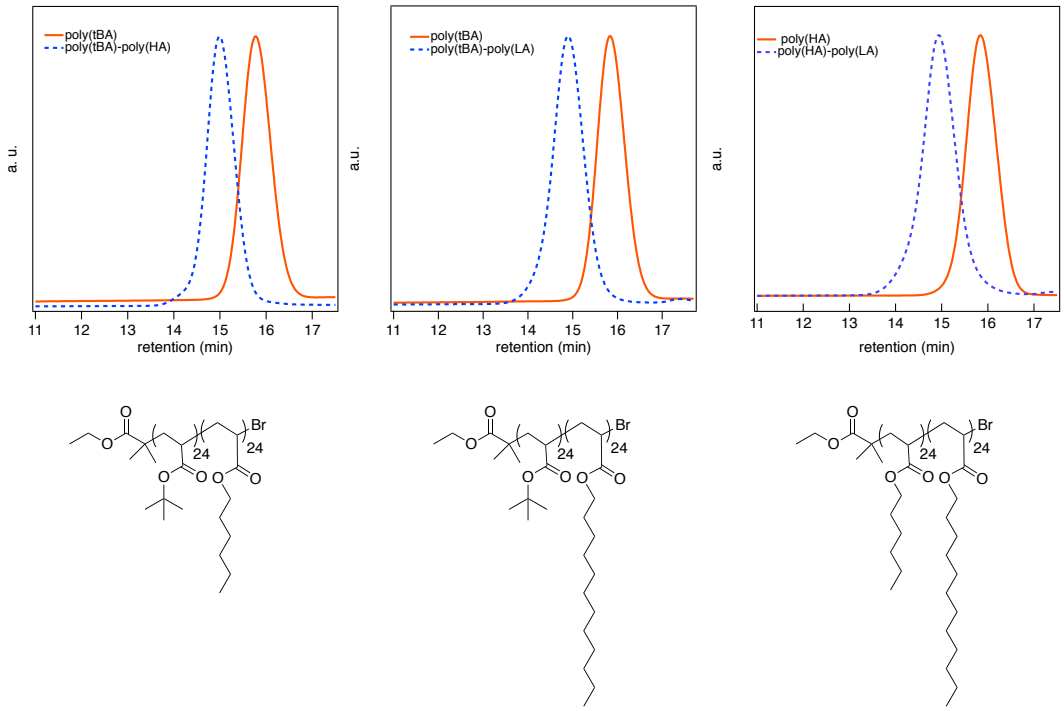

hydrophobic-hydrophobic block copolymers

Figure 4.12: GPCs of hydrophobic-hydrophobic block copolymers show monodisperse curves.

GPC curves of each polymer indicate highly uniform, monodisperse blocks were achieved from the synthesis, with average molar mass dispersity of $Đ = 1.1$ for the first block and $Đ \leq 1.2$ after addition of the second block.

The hydrophobic copolymers are shown in Figure 4.12. tBA-HA showed a $M_{n,GPC}$ of 7.5K and a final $Đ$ of 1.08. tBA-LA showed a $M_{n,GPC}$ of 8.2K and a final $Đ$ of 1.10. HA-LA showed a $M_{n,GPC}$ of 7.8K and a final $Đ$ of 1.14.

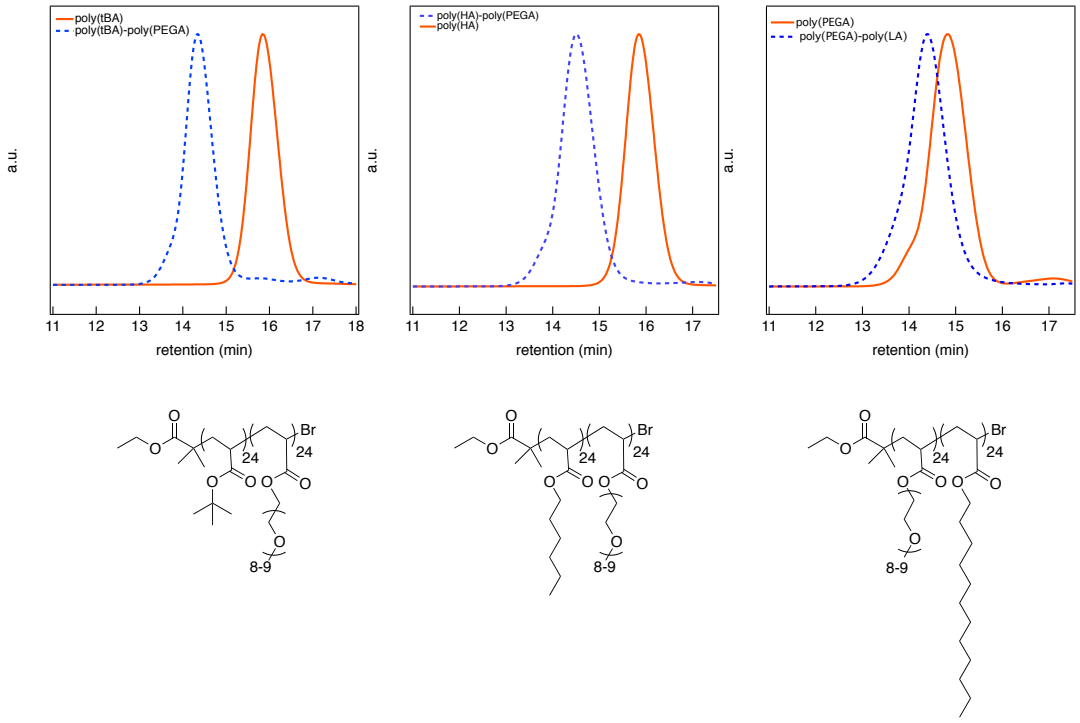

Figure 4.13: GPCs of hydrophobic-hydrophilic block copolymers show monodisperse curves.

The hydrophobic-hydrophilic copolymers are shown in Figure 4.13. PtBA-PPEGA showed a $M_{n,GPC}$ of 13.2K and a final $Đ$ of 1.10. PHA-PPEGA showed a $M_{n,GPC}$ of 11.5K and a final $Đ$ of 1.12. PPEGA-PLAc showed a $M_{n,GPC}$ of 13K and a final $Đ$ of 1.16. The PEG-diblocks shows a broader peak than the other diblock copolymers, possibly due to differences in how the PEG side chain interacts with the column compared to the PS standards.

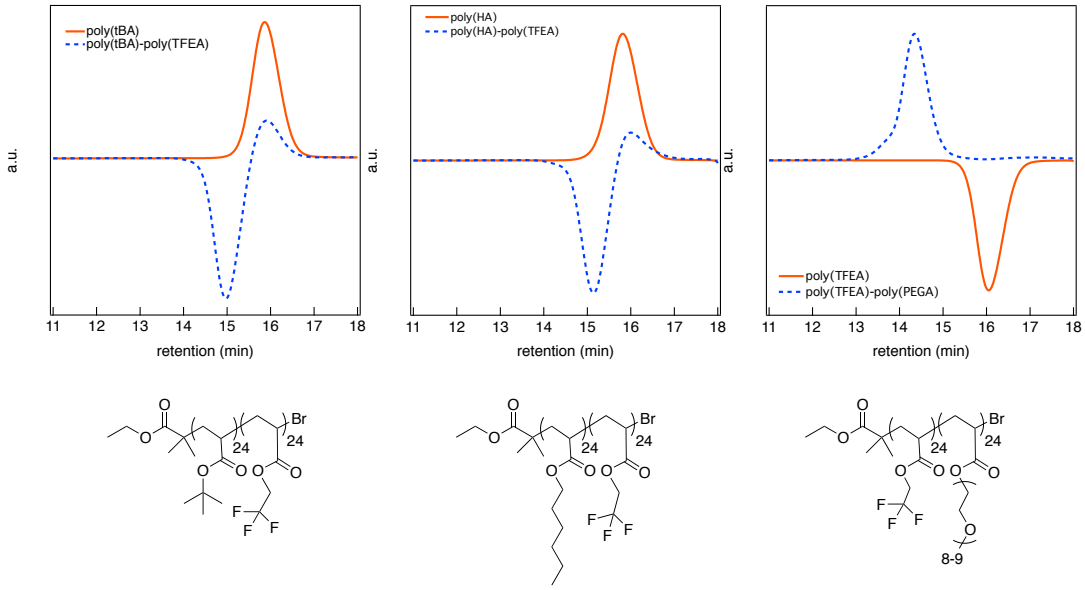

semi-fluorinated block copolymers

Figure 4.14: GPCs of semi-fluorinated block copolymers show monodisperse curves. The fluorinated blocks have a negative refractive index compared to the chloroform eluent. The polymer PTFEA-PLAc is shown in the following chapter.

The semi-fluorinated copolymers are shown in Figure 4.14. PtBA-PTFEA showed a $M_{n,GPC}$ of 7.9K and a final $Đ$ of 1.07. PHA-PTFEA showed a $M_{n,GPC}$ of 6.8K and a final $Đ$ of 1.05. PTFEA-PPEGA showed a $M_{n,GPC}$ of 13.6K and a final $Đ$ of 1.10.

4.4 SAXS Measurements

Small angle x-ray scattering (SAXS) measurements

Samples were prepared by dropcasting the diblock copolymers from DCM into steel washers fitted with kapton tape, where they were annealed under vacuum at 150° for 18h prior to analysis and allowed to return to room temperature by ambient cooling. SAXS measurements were performed first using a custom-built SAXS diffractometer at the Materials Research Laboratory (MRL) X-ray facility at the University of California, Santa Barbara. As described previously [10], 1.54 $\mathring{A}$ Cu K α X-rays were generated using a Genix 50 W X-ray microsource (50 μ m micro-focus) equipped with FOX2D collimating multilayer optics (Xenocs, France) and high efficiency scatterless single crystal/metal hybrid slits. 2D SAXS data were collected on a DECTRIS EIGER R 1M area detector with a 1030 x 1065 resolution (DECTRIS, Switzerland). Sample to detector distances were 1.7 m and calibrated with an Ag behenate standard. 2D-data were reduced to a one-dimensional form as a function of the magnitude of the wave vector q,

$$\mathbf{q} \quad = \mid \mathrm{q} \mid = 4\pi \ sin(\theta/2)/\lambda$$

w here λ is the X-ray wavelength and θ is the scattering angle. Data was converted from 1D to 2D using the NIKA Igor package [90].

Hydrophobic-hydrophobic polymers

No phase separation was discernable for the hydrophobic-hydrophobic polymers, PtBA-PLAc, PtBA-PHA, and PHA-PLAc (Figure 4.16,4.15, 4.17). This is to be expected, as there are no forces acting on these polymers (Figure 4.18). A

glass transition temperature (T_g) as measured by DSC was found for PtBA-PHA at -27.4°C. Melting temperatures were found for the lauryl acrylate diblocks: for PtBA-PLAc, T_m at 1.4°C, and for PHA-PLAc T_m at 20.1°C.

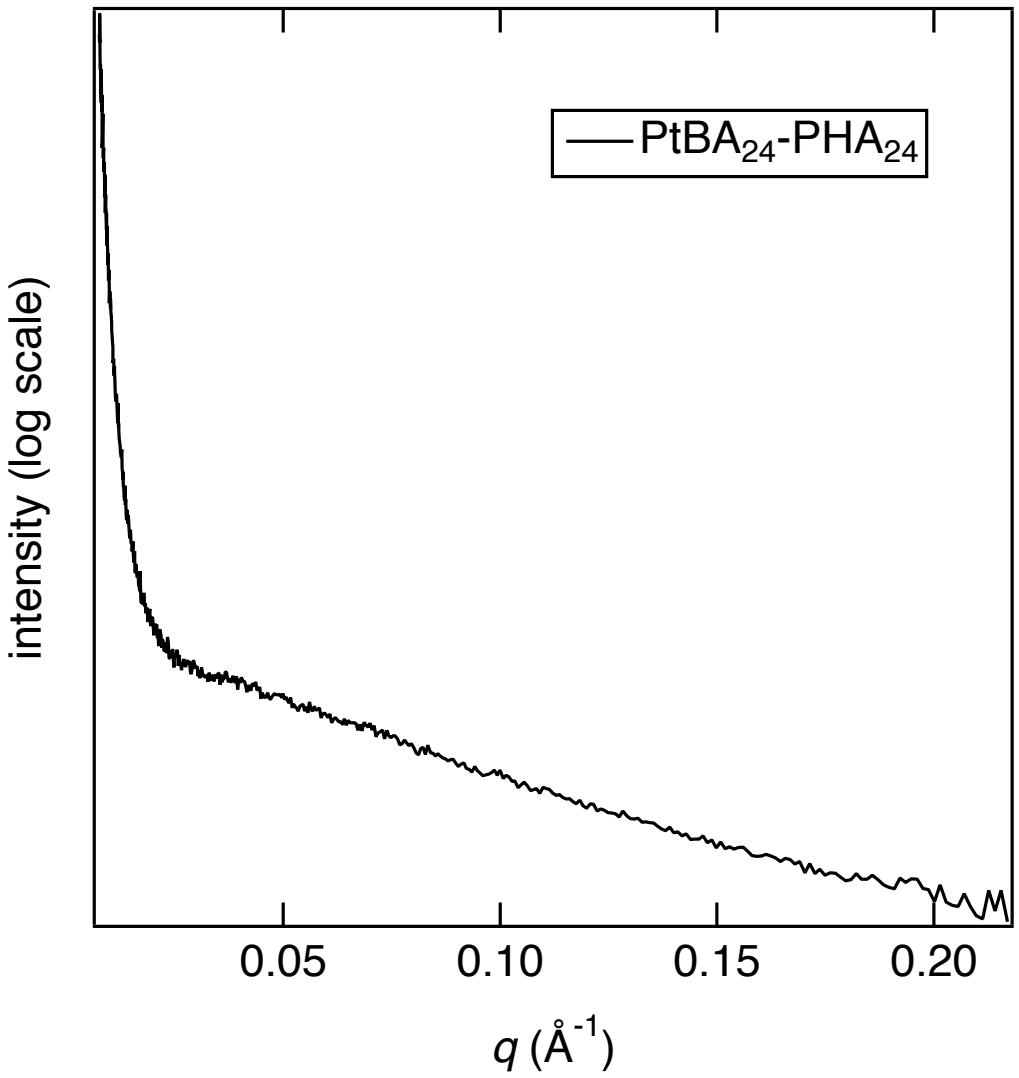

Figure 4.15: SAXS patterns show no phase separation or self-assembly in the hydrophobic block copolymer PtBA-PHA.

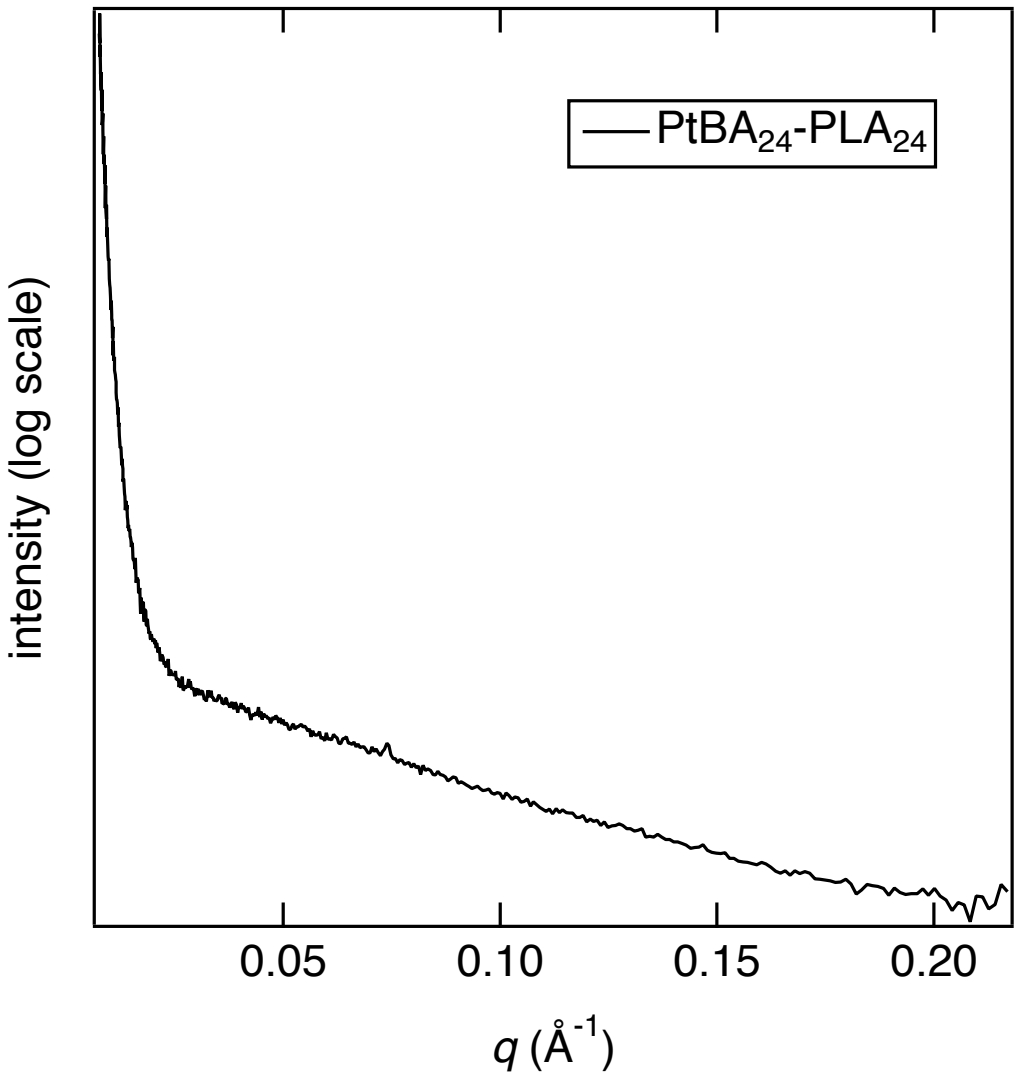

Figure 4.16: SAXS patterns show no phase separation or self- assembly in the hydrophobic block copolymer PtBA-PLAc.

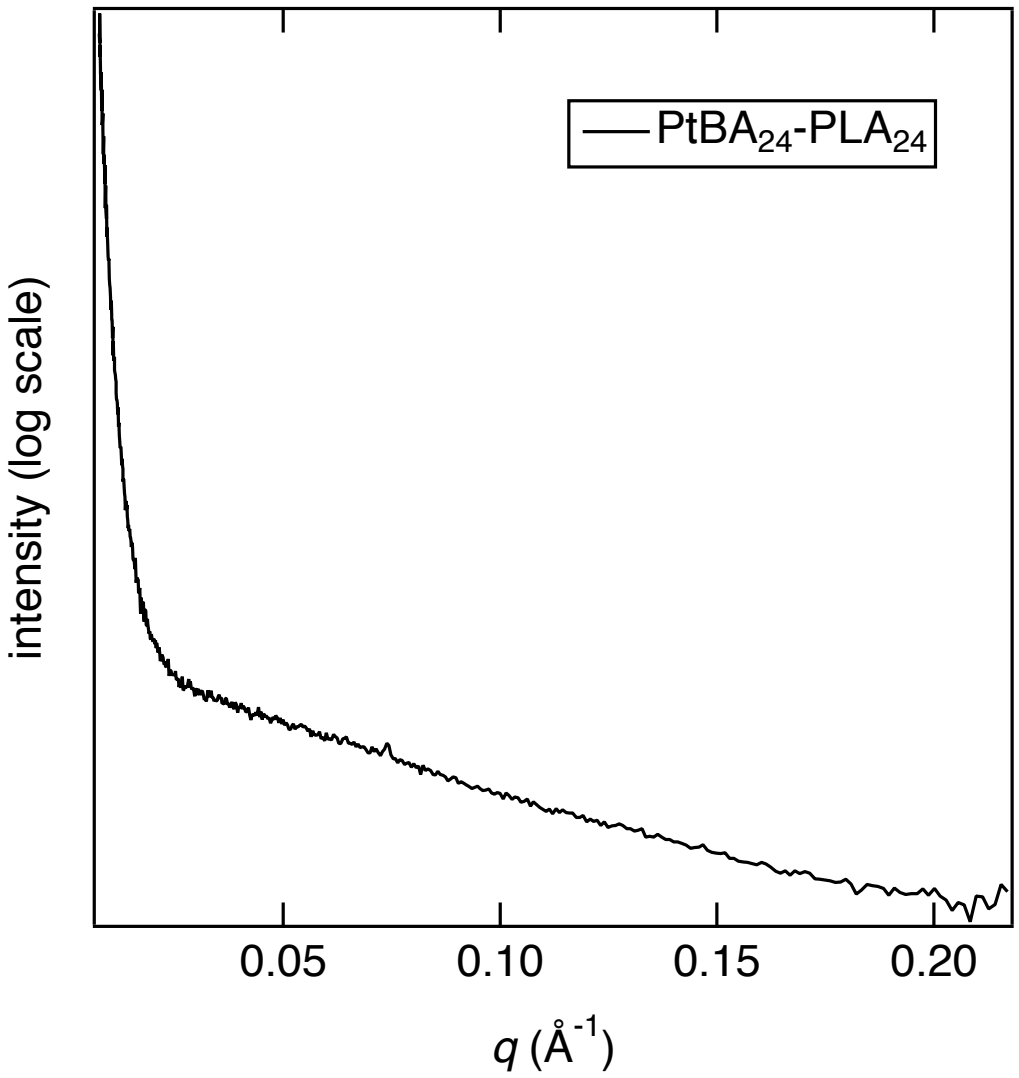

Figure 4.17: SAXS patterns show no phase separation or self- assembly in the hydrophobic block copolymer PHA-PLAc.

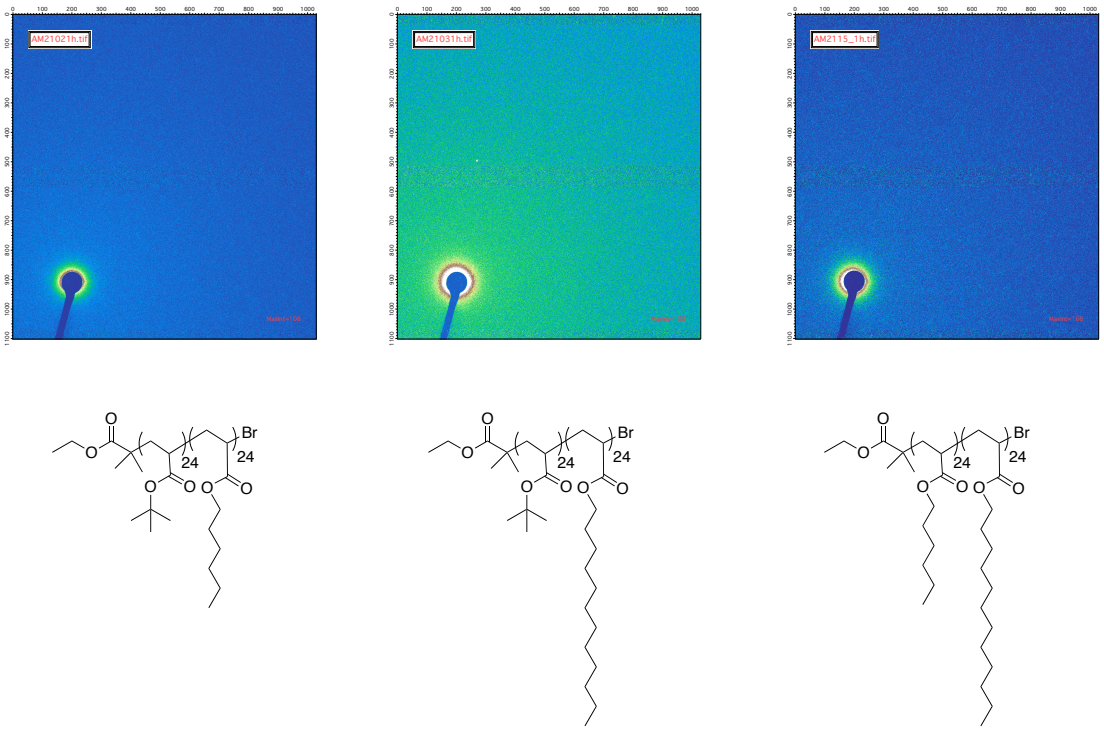

Figure 4.18: SAXS images show no self-assembly behavior for the hydrophobic-hydrophobic diblock copolymers.

Hydrophobic-hydrophilic polymers

Self-assembly behavior was evident for hydrophobic-hydrophilic polymers, PtBA-PPEGA, PHA-PPEGA, and PPEGA-PLAc. For PtBA-PPEGA (Figure 4.19, 4.20), a small bump in the SAXS pattern indicates undefined structures were formed, such as disordered spheres or micelles. The PPEGA-PLAc diblocks formed well ordered, hexagonally packed cylinders (Figure 4.21, 4.22). The PHA-PPEGA diblocks also formed hexagonally packed cylinders, but with fewer peaks (Figure 4.23, 4.24). Thermal transitions were measured by DSC for some of the polymers. PtBA-PPEGA showed a T_m at 21.23°C while PTFEA-PPEGA showed a T_m at 19.6°C. PLAc-PPEGA showed a T_m at 6.7°C.

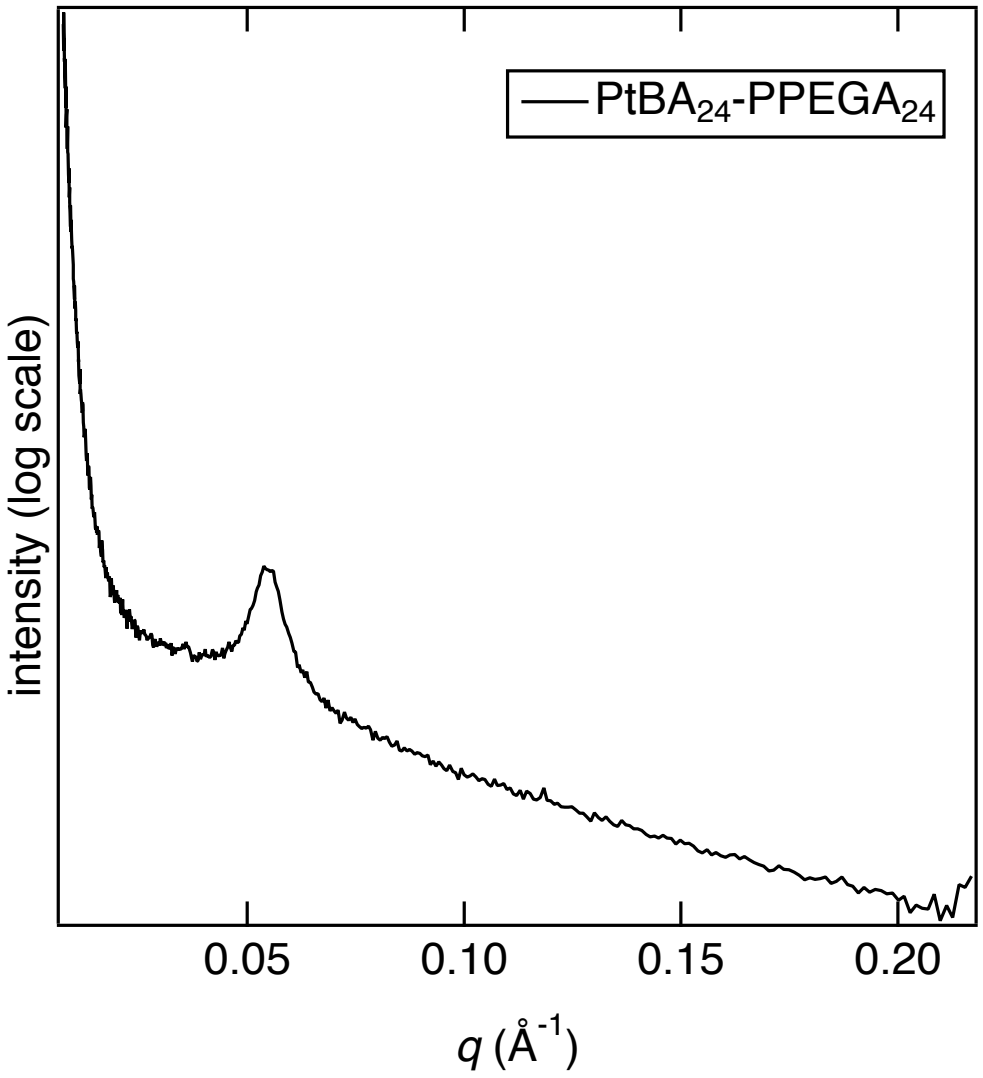

Figure 4.19: SAXS patterns show some degree of phase separation and spherical micelle formation in PtBA-PPEGA.

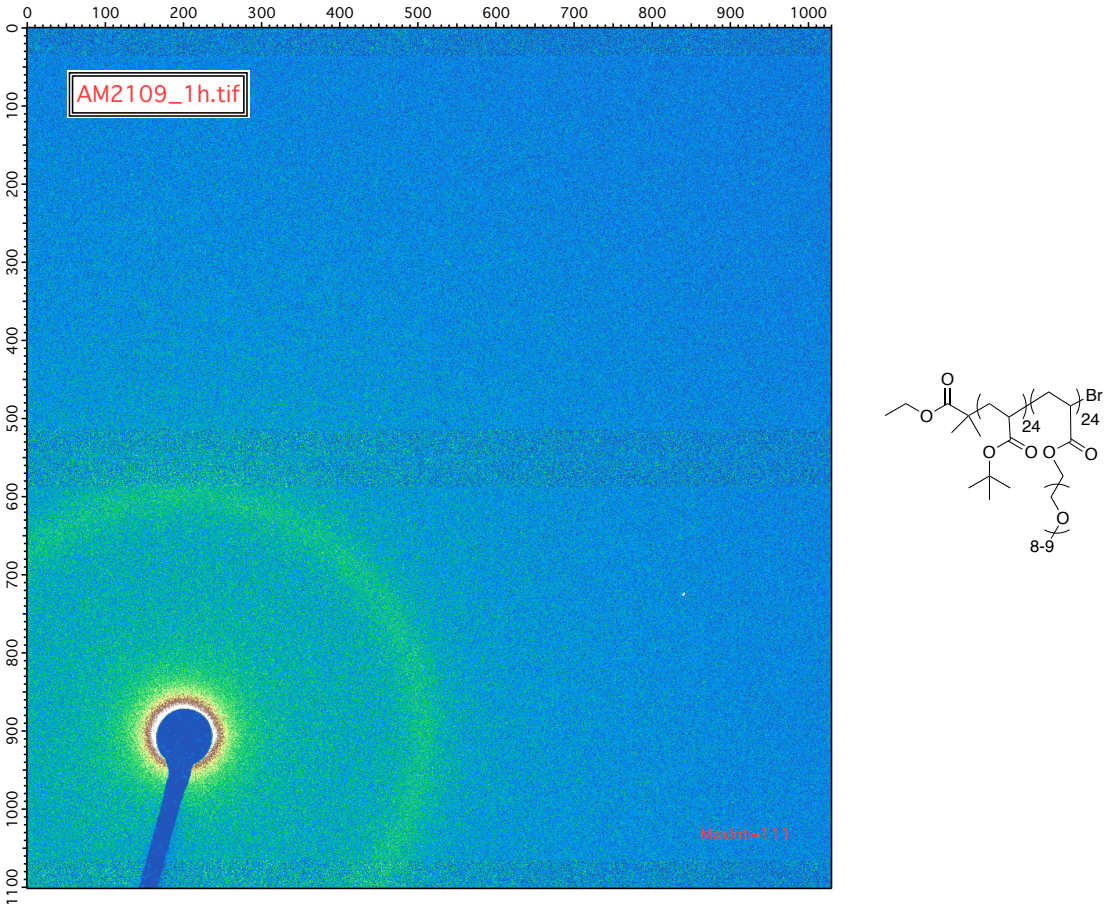

Figure 4.20: SAXS image shows phase separation for PtBA-PPEGA.

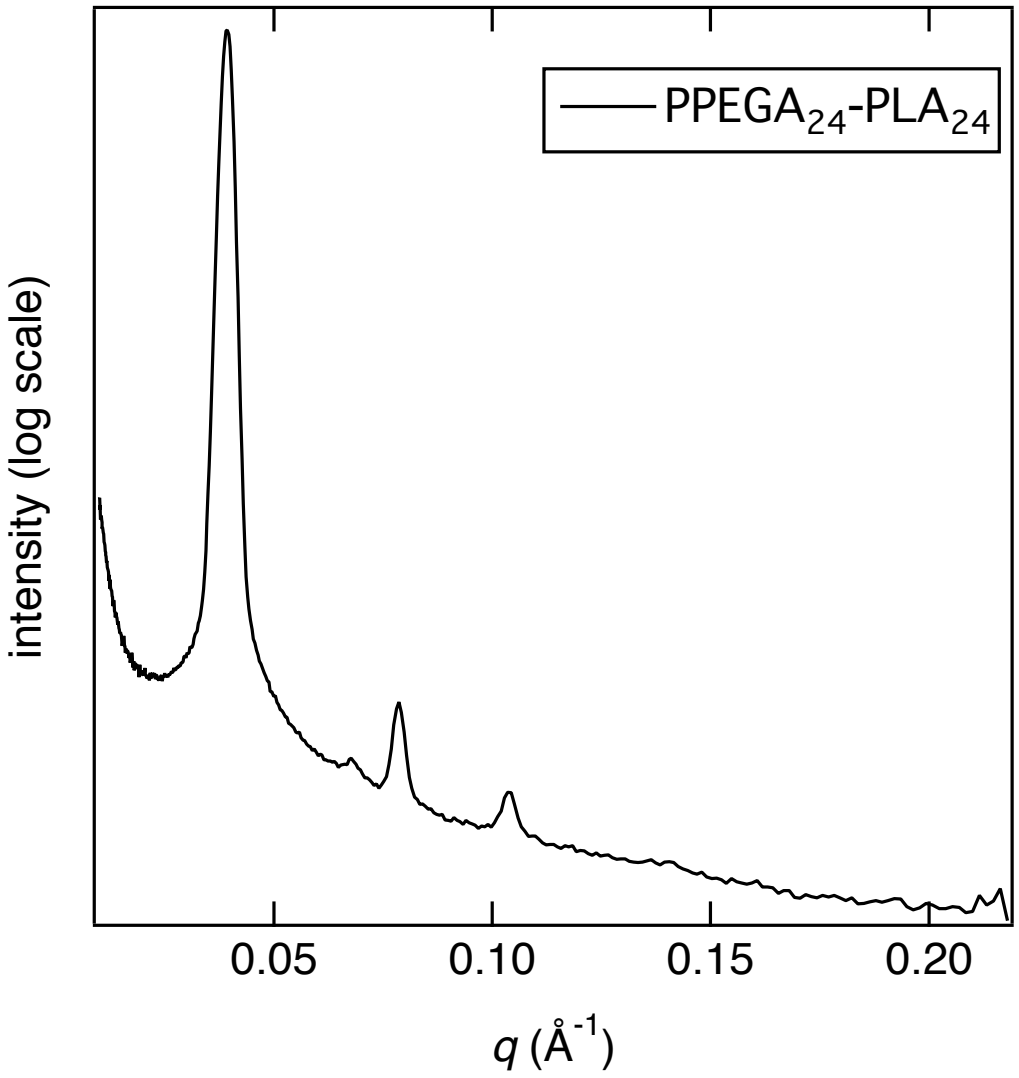

Figure 4.21: SAXS patterns shows the formation of hexagonally packed cylinders (hcp), where the reflections given q* is the most intense peak, the higher q peaks correspond to $\sqrt{3}$,$\sqrt{4}$, and $\sqrt{7}$.

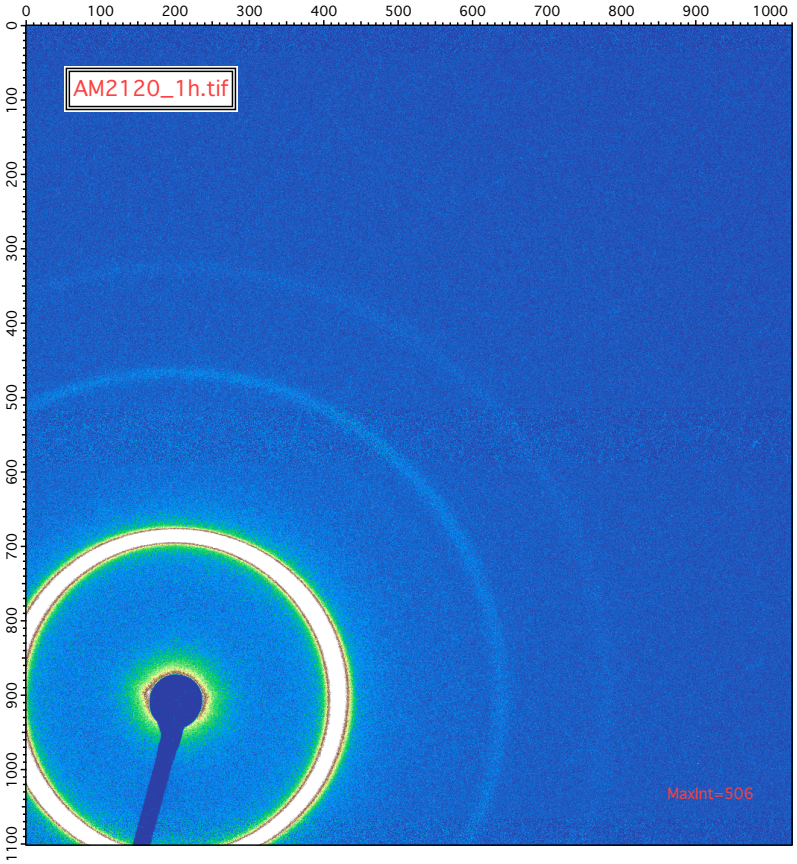

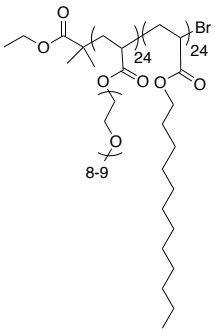

Figure 4.22: SAXS image shows well-ordered, multiple reflections indicative of hexagonally packed cylinders for PPEGA-PLAc.

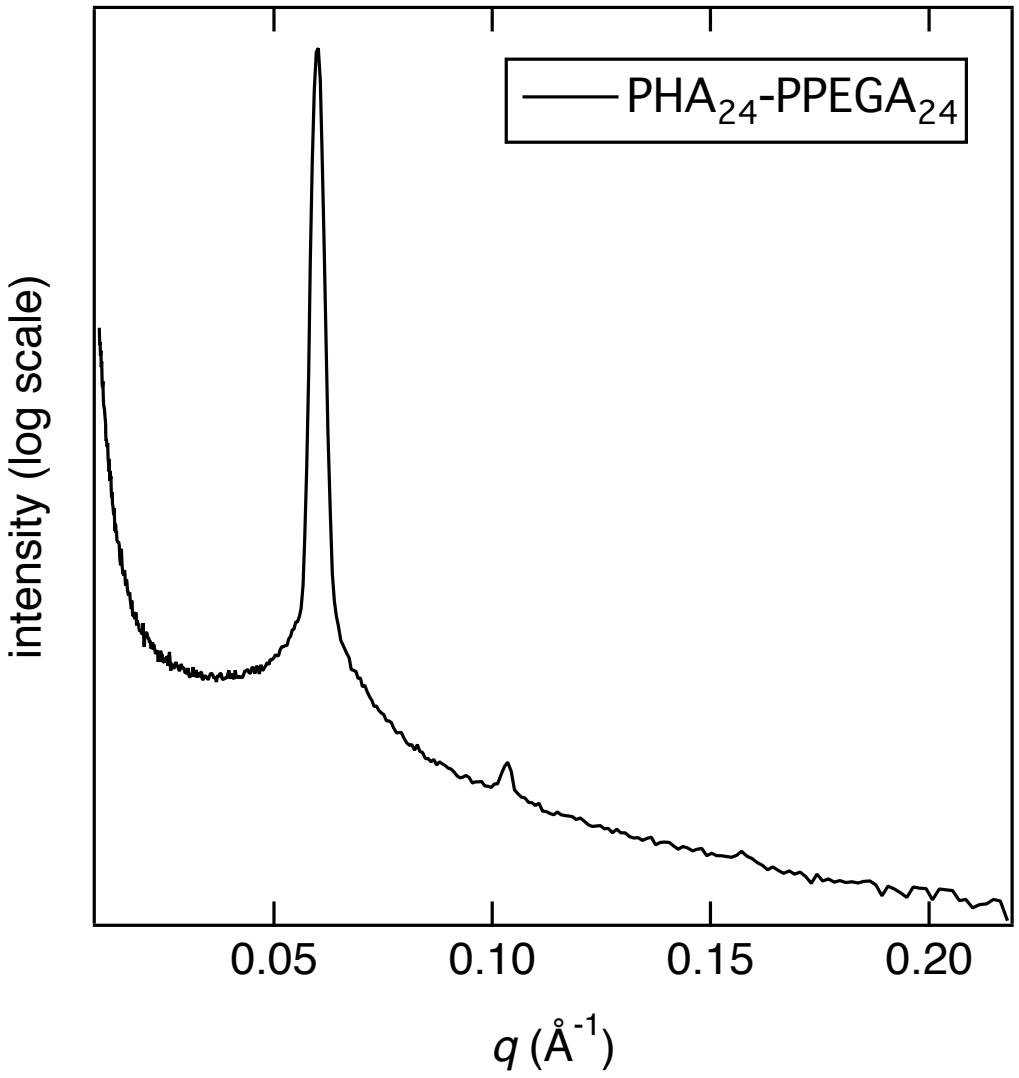

Figure 4.23: SAXS patterns shows the formation of hexagonally packed cylinders (hcp), where the reflections given q* is the most intense peak, the higher q peaks correspond to $\sqrt{3}$ and $\sqrt{7}$.

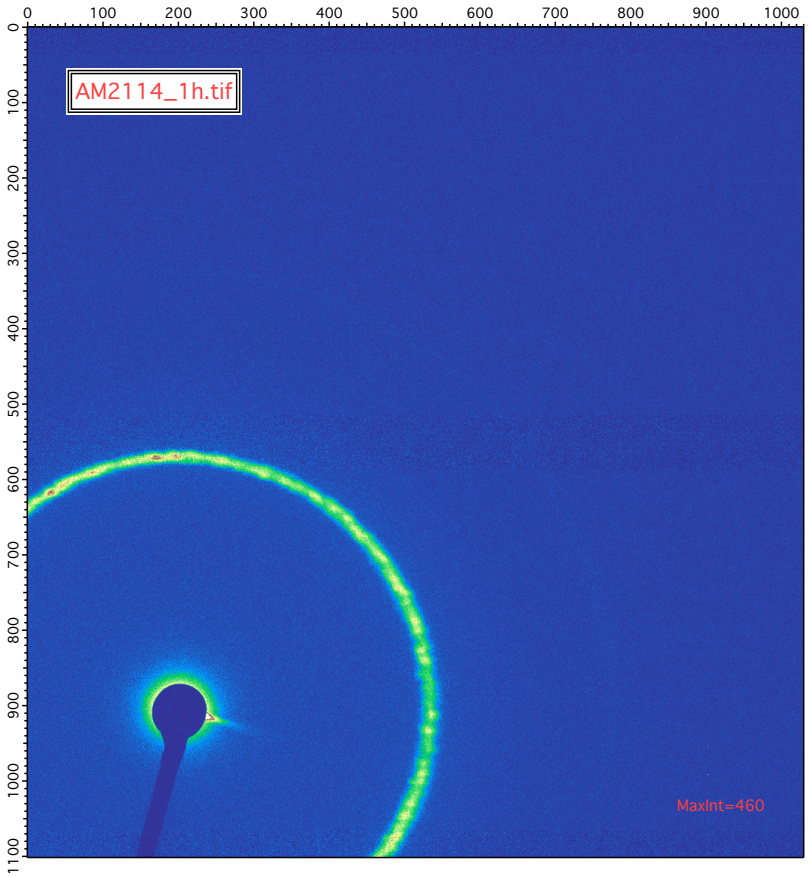

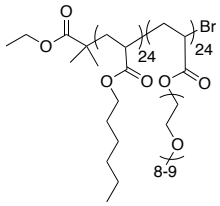

Figure 4.24: SAXS image shows reflections indicative of hexagonally packed cylinders for PHA-PPEGA.

Semi-fluorinated diblock polymers

Self-assembly behavior was evident for hydrophobic-hydrophilic polymers, PtBA-PTFEA, PHA-PTFEA, PTFEA-PLAc (discussed in the following chapter), and PTFEA-PPEGA. For PtBA-PTFEA (Figure 4.25), a small bump in the SAXS pattern possibly indicates undefined structures were formed, but appears that no notable phase separation occurred (Figure 4.26). Similarly, the PHA-PTFEA diblocks did not form ordered structures, but some small degree of phase separation did occur (Figure 4.27, 4.28). The PTFEA-PPEGA diblocks also displayed some degree of phase separation into spherical micelles (Figure 4.29, 4.30). Thermal transitions were found in some of the semi-fluorinated polymers. For PtBA-PTFEA, a T_m was found at 8.6°C. PTFEA-PPEGA showed a T_m at 19.6°C.

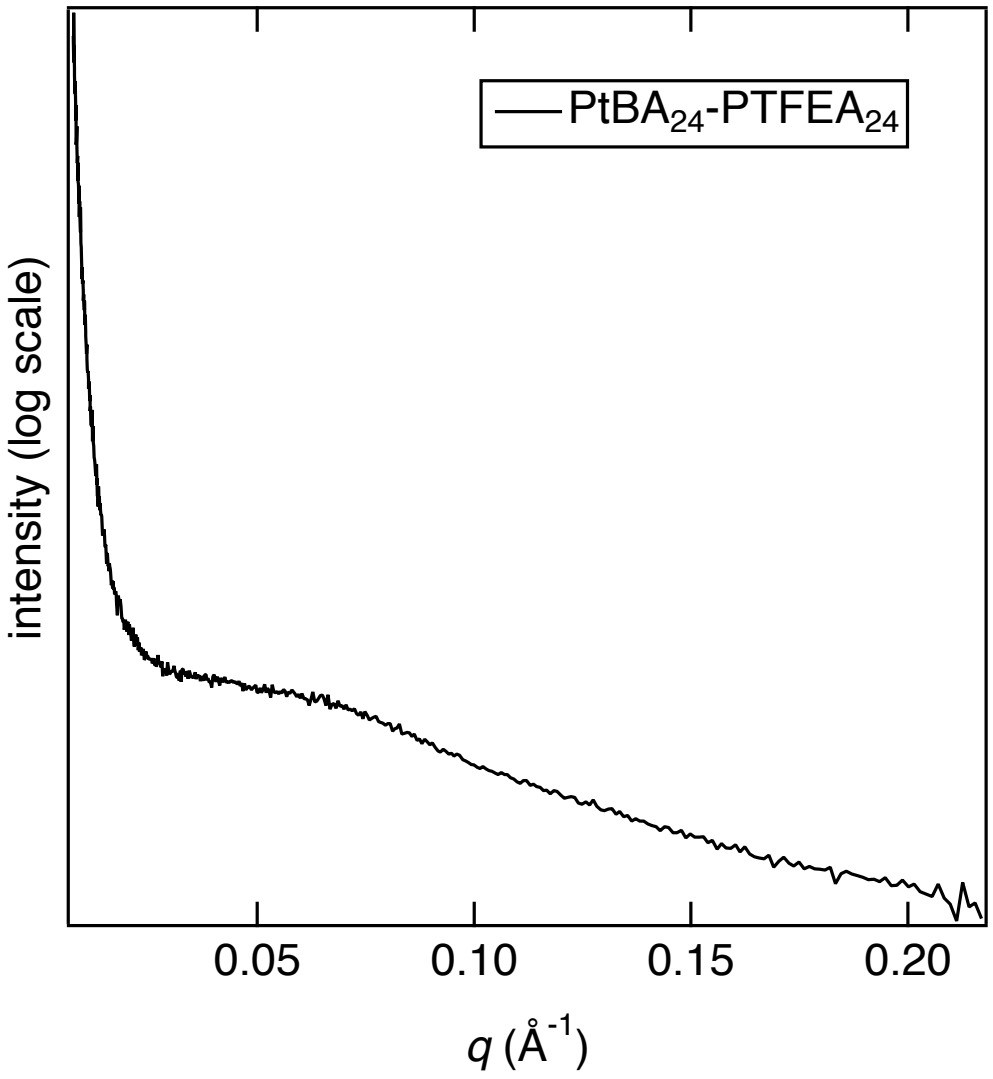

Figure 4.25: SAXS patterns shows no notable phase separation for PtBA-PTFEA.

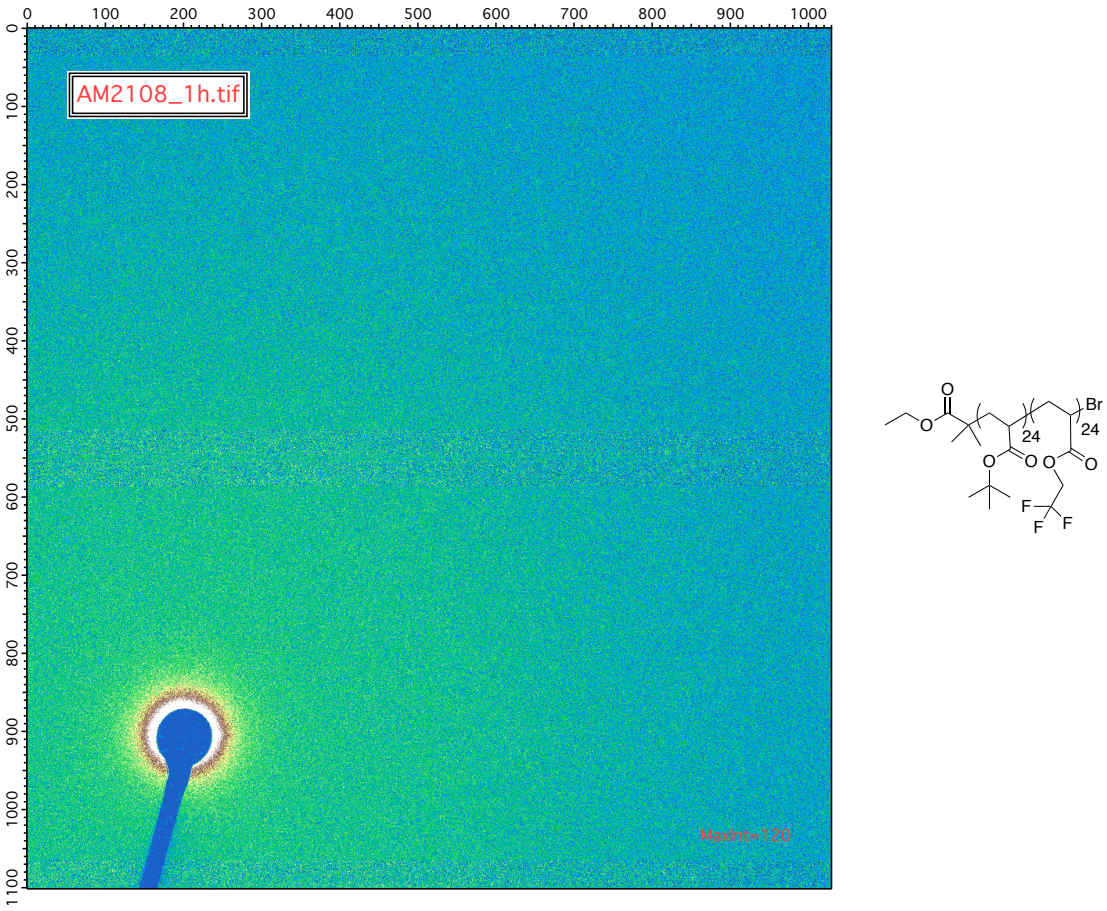

Figure 4.26: SAXS image shows no notable phase separation for PtBA-PTFEA.

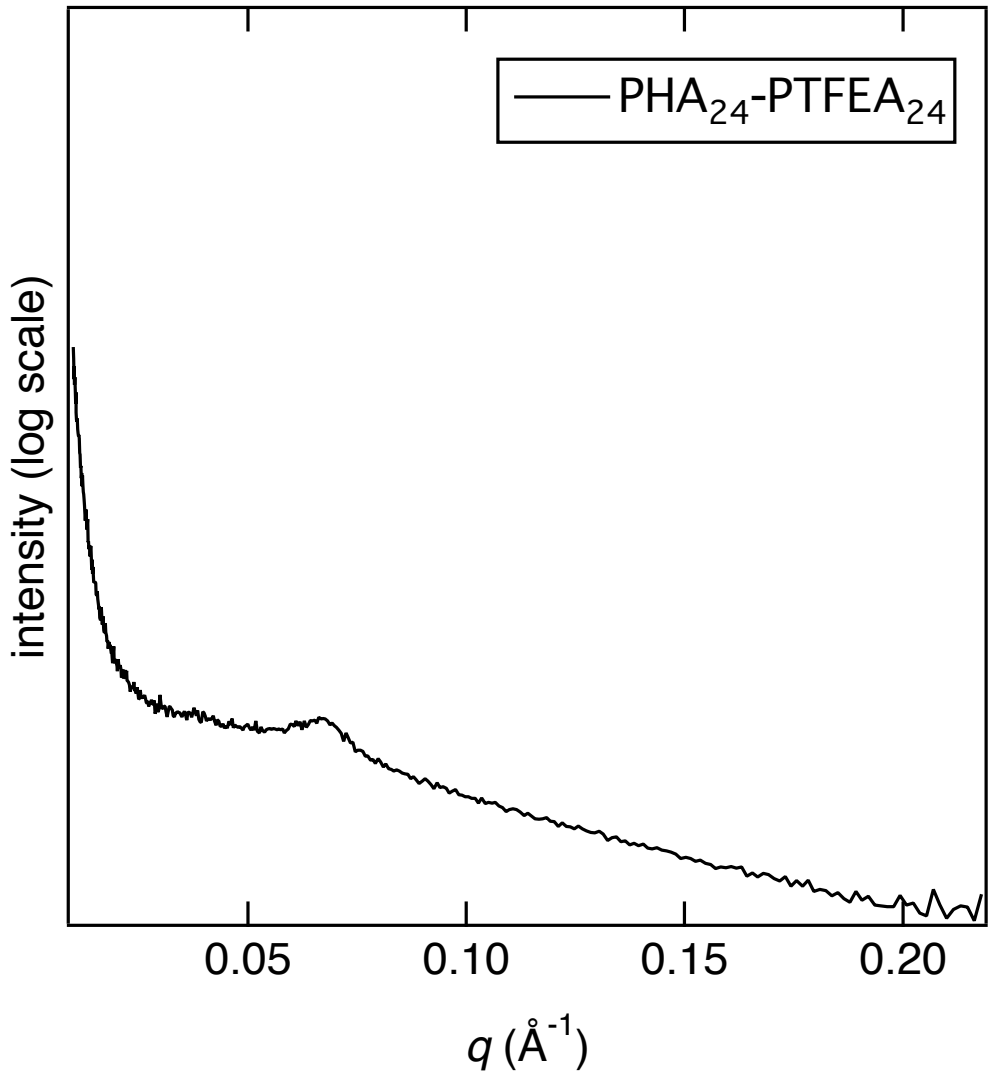

Figure 4.27: SAXS patterns shows minor phase separation into an spherical micelles for PHA-PTFEA.

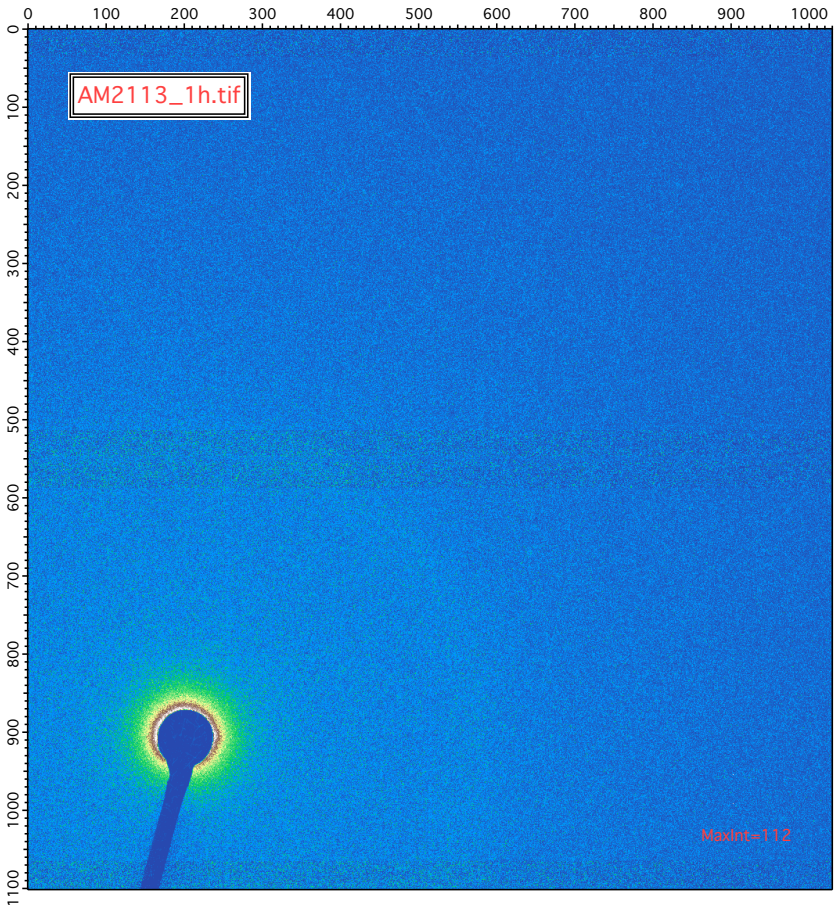

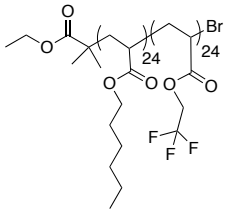

Figure 4.28: SAXS image shows a light, broad reflection indicating minor phase separation for PHA-PTFEA.

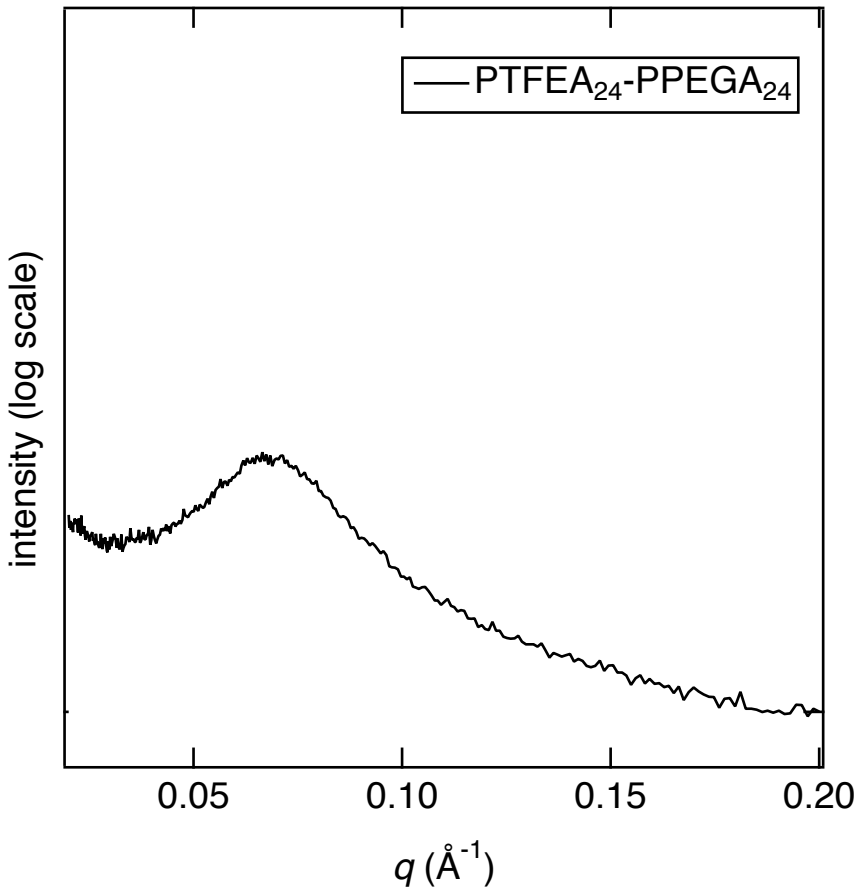

Figure 4.29: SAXS patterns shows some degree of phase separation occurred for PTFEA-PPEGA into spherical micelles.

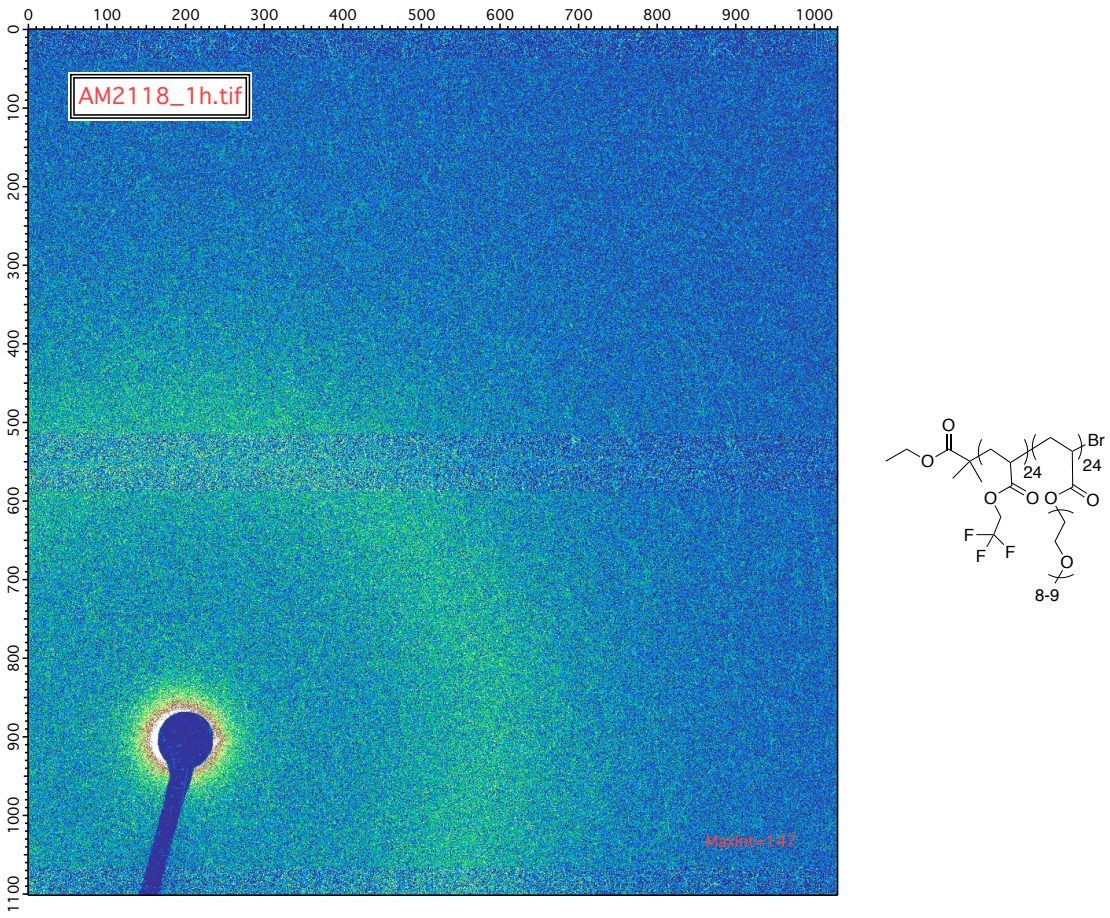

Figure 4.30: SAXS image shows a large ring reflection indicating phase separation occurred for PTFEA-PPEGA.

4.5 Conclusion

A family of ten acrylic diblocks were synthesized using light mediated Cu ATRP in trifluoroethanol, affording monodisperse polymers and high chain end fidelity as evident from the ability to chain extend with a second monomer. These diblock copolymers were tested for phase separation behavior by SAXS. Around N = 24, hexagonally packed cylinders were found in PHA_{22}-$PPEGA_{22}$ and $PPEGA_{23}$-$PLAc_{24}$. The diblocks with the longer alkyl chain, C12, showed the most pronounced self-assembly behavior by SAXS. Future work in designing polymers that self-assemble into interesting morphology can expand on three areas: increasing the library of hydrophobic and hydrophilic functionalities, increasing N of each diblock, and targeting mismatch between the block lengths (i.e. A_{24}-B_{48}) to force the phase diagram in one direction.

Chapter 5

Discovery of A15 phase in semi-fluorinated diblock copolymers

5.1 Introduction

The packing and self-assembly of matter into organized shapes and morphologies dictates long-range spatial order and physical properties. In the realm of polymer morphology, traditional views of equilibrium phases in polymer self-assembly, spherical, cylindrical, gyroid, and lamellar, are beginning to be challenged by the discovery of new phases predicted by self-consistent field theory (SCFT) and increasingly found experimentally [91,92,93,94,95]. The ability to predict and select particular self-assembly behavior in designer diblock copolymers will revolutionize their applications in nanotechnology. Recent work in polymer science has shown

the existence of non-canonical Frank Kasper phases and Laves Phases in spherical diblock copolymers [96], opening up the field to more available morphologies for applications ranging from adhesives to nanolithography. In particular, temperature dependence appears to play a crucial role in the exhibition of these phases, in addition to polymer architecture. [91]

Displayed polymer morphology in AB diblock systems is dependent on three main factors: the Flory Huggins interaction parameter, χ, which is a measure of the repulsive interactions between the A and B monomers, the volume fraction of the A block, ϕ, and the degree of polymerization, N. Recent theoretical work [97, 98] using SCFT has shown the close existence of A15, hcp, and σ in highly asymmetric AB diblock copolymers Figure 5.1, 5.2. Experimental work has shown A15 (cubic $Pm\tilde{3}n$ symmetry) in small molecule surfactants. [99] Recent theoretical work has shown both sigma and A15 phases (Figure 5.3) possible in AB diblock copolymers alternatively represented as "core-corona" or "rod-coil" [100, 101] and conformationally asymmetric polymers [97].

Others [102, 103] have recognized the importance of long, squishy alkyl chains in promoting self-assembly into the A15 phase in dendrimers and small molecule surfactants, as these chains reduce steric interactions and contact between spheres– indeed, increasing the relative sphere size of one of the blocks pushes the governing forces towards polyhedra shapes (Figure 5.4). [97] In particular, as Grason and coworkers pointed out in the early 2000s, the A15 morphology becomes the preferred minimal free energy state, the ground state, as long as the hexagonally packed phase does not interfere [98]. In our work, we find that A15 is the preferred morphology at room temperature following a slow cool from disordered

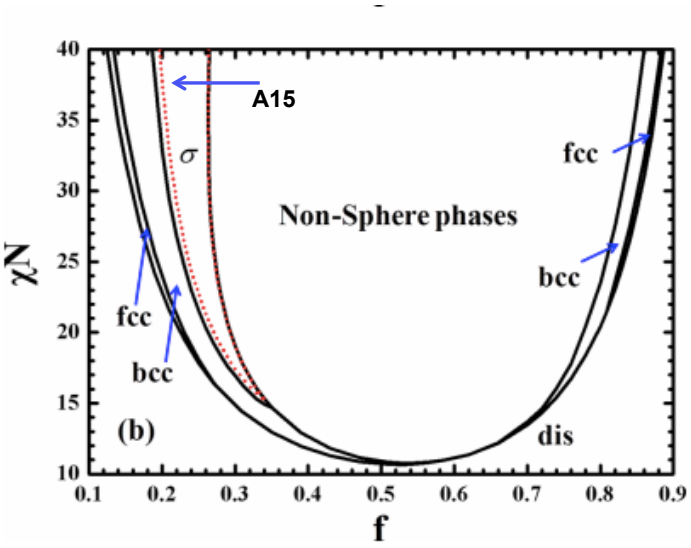

Figure 5.1: Reproduced from reference [97]. Phase diagram of sphere phases for miktoarm AB_m block copolymers, where m = 2. The boundaries between the metastable phase A15 and the bcc and the hexagonal phases are plotted in red dashed lines.

state at 150°C. However, when there is rapid cooling in the span of several minutes from above the ODT (90°C), the hexagonal phase is formed. This indicates the material can be classified as thermotropic liquid crystals.

We report the discovery of the A15 phase in a diblock copolymer, which had only been theorized to exist in AB_2 diblock systems. A unique aspect that stabilizes the existence of the A15 morphology is related to the conformational asymmetry of the blocks, which affects the volume densities that the polymers take up in space and therefore the three dimensional structures. This is due to the very different polymer densities of each block. Literature reports PTFEA has a density of $\rho = 1.411$ g·mL^{-1} while PLAc is much less dense, exhibiting $\rho = 0.94$ g·mL^{-1}. [105] To calculate where each diblock sits on the phase diagram, the volume fraction of each block is taken into account with the following equation,

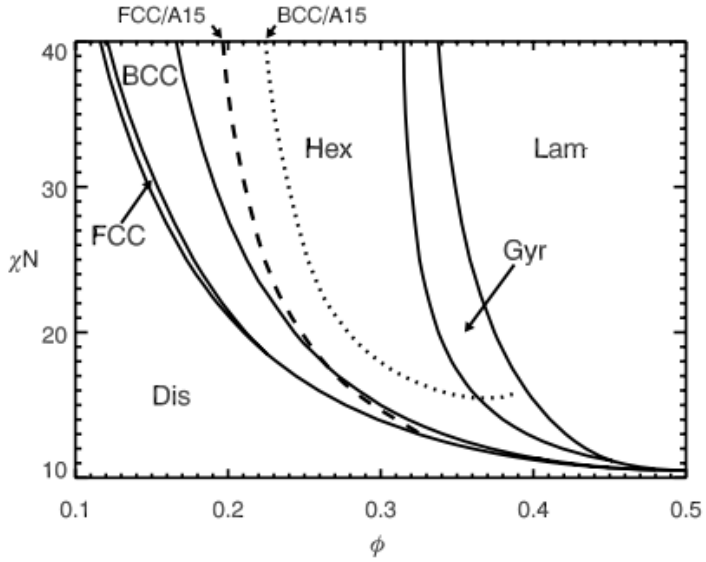

Figure 5.2: Reproduced from reference [98]. Phase diagram of AB linear diblock copolymers, showing the A15 phase coexistence curves with bcc and hexagonal phases. The A15 phase region is between the dashed lines

using both the polymer molecular weight, M_n, and the polymer density, ρ:

f =

$$\frac{Va}{Va + Vb}$$

where Va =

$$\frac{Mn}{\rho}$$

At a degree of polymerization (DP) = 20 for both blocks of PTFEA-PLAc, the volume fraction is f = 0.32 for the fluorinated block. The A15 phase, stabilized by a small mix of hexagonally packed cylinders, was found reproducibly for these polymers across multiple samples (different syntheses). Increasing the DP just slightly to DP $\approx$ 25, the f = 3.0, the PTFEA-PLAc diblock displayed σ

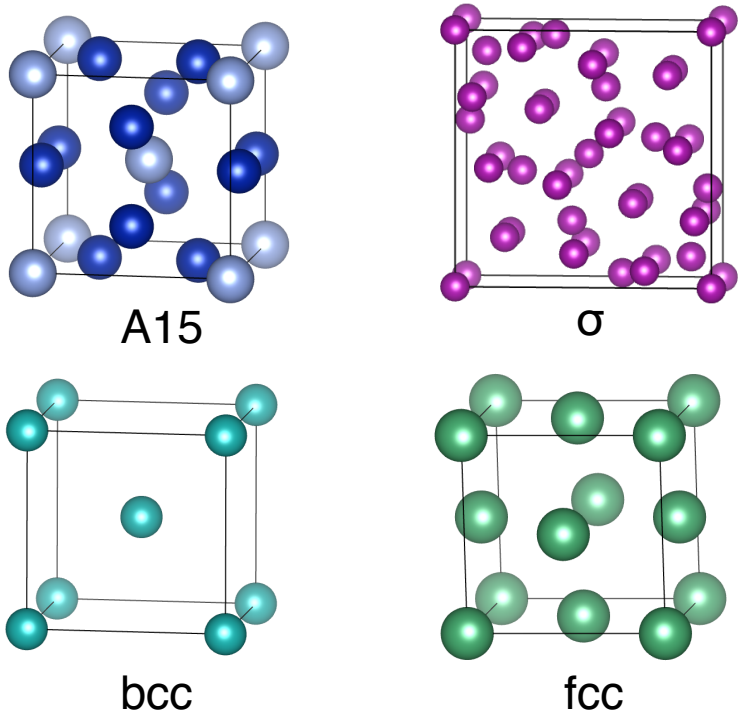

Figure 5.3: Cubic unit cells for A15, sigma (σ), body centered cubic (bcc), and face centered cubic (fcc) lattices.

morphology. Increasing M_n to almost double, DP *approx* 42 for both blocks of PTFEA-PLAc and f = 0.31, hexagonally packed cylinders was the sole morphology.

Small angle x-ray scattering was used to determine the morphology of a series of diblock copolymers poly(trifluoro ethyl acrylate-b-lauryl acrylate) (herein referred to as PTFEA-PLAc) where f $\sim$ 0.3 for the fluorinated moiety (Figure 5.5).

5.2 Materials and Methods

Materials

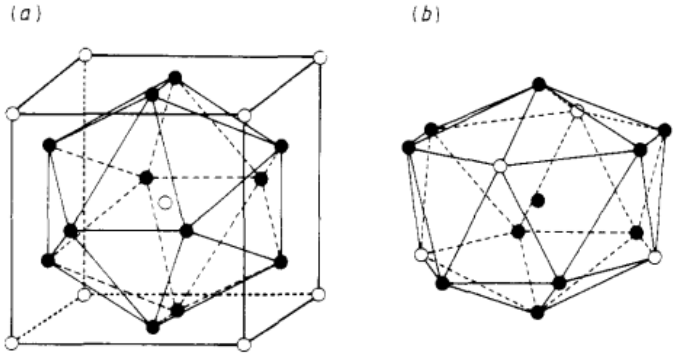

Figure 5.4: Figure and caption reproduced from reference [104]. Primitive unit cell and coordination polyhedra of the A15 structure: (a) polyhedron centred on a B atom; (b) on an A atom.

Lauryl acrylate (LA or LAc, 99 %) was purchased from Sigma Aldrich and passed through a column of basic alumina (150 mesh, Brockmann I grade) just prior to use. 2,2-trifluoroethyl acrylate (TFEA, 99%), copper(II) bromide ($CuBr_2$) (99 %), and tris[2 (dimethylamino)ethyl]amine (Me_6-TREN) (97 %) were purchased from TCI America and used as received. Ethyl-α bromoisobutyrate (Ebib, 98 %) was purchased from Sigma Aldrich. 2,2-trifluoroethanol (TFE, 99 %) and dichloromethane (DCM, Reagent Grade) were purchased from Fisher Scientific. Dialysis tubing (MWCO = 5-6 kD) was purchased from Spectral Por.

Methods

Nuclear magnetic resonance (NMR) spectra were recorded on a Varian 600 MHz spectrometer using $CDCl_3$ as the solvent to determine reaction completeness and number-average molar masses (M_n). Molar mass distributions (Đ= M_w/M_n) were measured via size exclusion chromatography (SEC), relative to linear polystyrene standards, on a Waters 2690 separation module equipped with Waters 2414 refractive index and 2996 photodiode array detectors. $CHCl_3$ con-

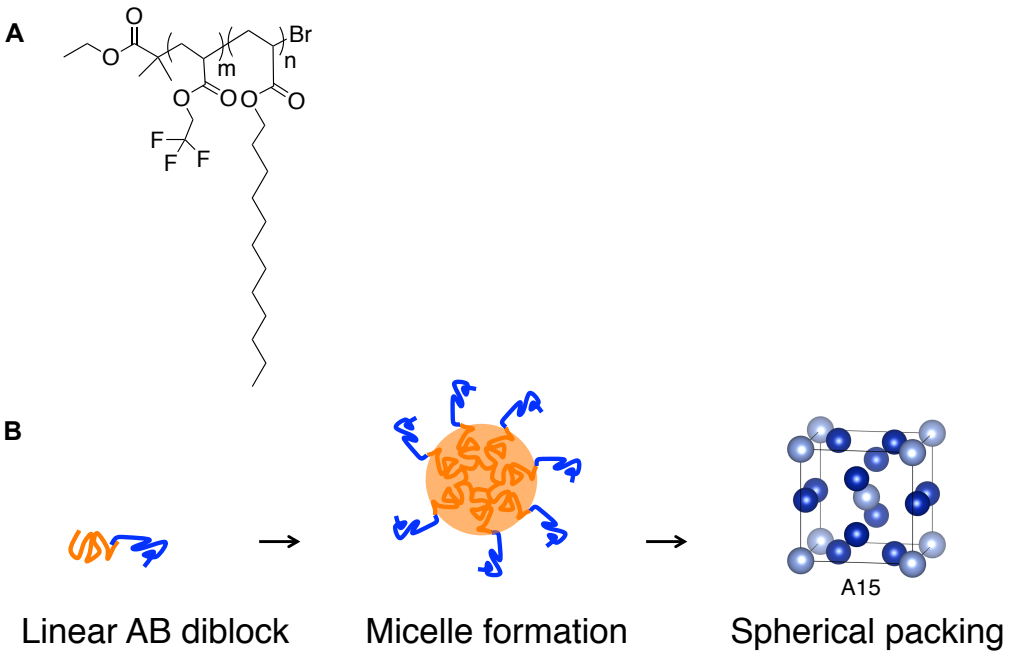

Figure 5.5: (A) Chemical composition of diblock poly(trifluoro ethyl acrylate-b-lauryl acrylate) where m and n range from 15-42. (B) Schematic showing polymer self-assembly to A15.

taining 0.25 % triethylamine was used as the eluent at a flow rate of 1 mL·min^{-1}. Thermogravimetric Analysis (TGA) was performed on a Discovery (TA Instruments), using a heating rate of 10°C per min from 25°C to 600°C and nitrogen purge gas. Differential scanning calorimetry (DSC) was performed in crimped Al pans on a TA Instruments DSC, where data from three heating and cooling cycles were taken from -50°C to 150°C at a rate of 5°C or 10°C per min.

General Synthesis of $PTFEA_{20}$-b-$PLAc_{20}$

For a target degree of polymerization = 20 per block, a typical reaction contained the following amounts of reagents, with equivalents relative to the initiator: 20 eq. TFEA (1 mL, 7.89 mmol), 1 eq. Ebib (57.9 μL, 0.394 mmol), 0.02 eq.

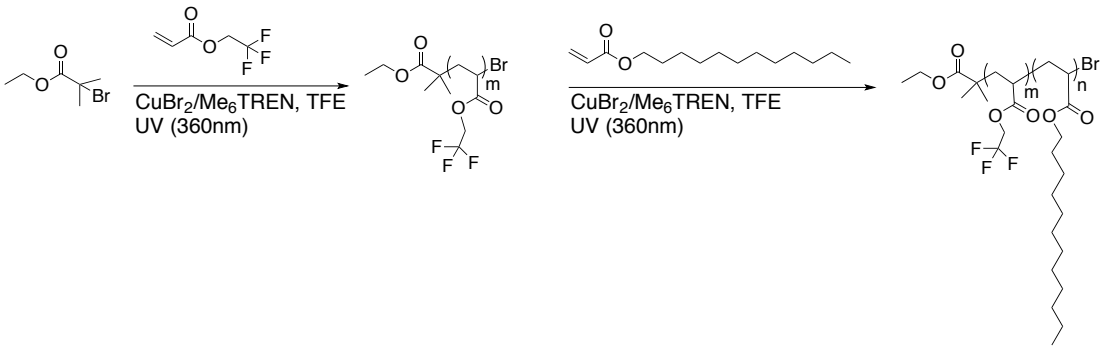

Figure 5.6: Synthetic scheme depicting diblock formation of poly(trifluoro ethyl acrylate-b-lauryl acrylate), where m and n range from 15-40.

$CuBr_2$ (1.7 mg, 7.89 μmol), 0.12 eq. Me_6TREN (12.6 μL, 47.3 μmol), and 1 mL TFE (1:1 to the monomer). For the second block, additional catalyst/ligand/TFE solution was injected with the second monomer, containing: 20 eq. LAc (2.14 mL, 7.89 mmol), 0.02 eq. $CuBr_2$ (1.7 mg, 7.89 μmol), 0.12 eq. Me_6TREN (12.6 μL, 47.3 μmol), and 1.07 mL TFE (50 vol% to monomer). Each reaction was prepared in the following way: $CuBr_2$, trifluoroethanol (TFE), and Me_6TREN were added to a glass reaction vial in that order and sonicated for several minutes until the mixture turned a bright green color and all $CuBr_2$ was dissolved. To the solvent/catalyst mixture was added Ebib with microliter syringe, a stirbar, and finally capped with a rubber septum and degassed under N_2 for 5 minutes. Degassed monomer TFEA was then added by syringe under N_2 atmosphere. The reaction vial was put under a UV nail curing lamp with stirring and allowed to react for 15 hours. At reaction completion as indicated by NMR, a solution containing LAc and catalyst/ligand/TFE was degassed and injected into the vial. Upon addition of the lauryl acrylate to the macroinitiator, the polymer became very viscous and turned milky white. After 24 hours, the reaction was checked

by NMR for complete monomer conversion and quenched by opening the vial to air. The reaction mixture was diluted in DCM, filtered over a column of basic alumina to remove the copper, and purified by dialysis (MWCO = 5-6000) against DCM (1L) for several days, changing the DCM twice daily. The purified diblock copolymer was collected as a white, viscous material and analyzed by ^{1}H NMR, differential scanning calorimetry (DSC), thermogravimetric analysis (TGA), and small angle x-ray scattering (SAXS). ^{1}H NMR (600 MHz, $CDCl_3$): δ 4.48 (d, J= 10.8 Hz, 2H), 4.06 (m, 2H), 2.55-1.72 (d, 3H), 1.57 (d, J =31.6 Hz, 4H), 1.28 (d, J = 18.4 Hz, 16H), 1.19-1.11 (m, 1H), 0.88 (t, J = 6.9 Hz, 3H).

Small angle x-ray scattering (SAXS) measurements

Samples were prepared by dropcasting the diblock copolymers from DCM into steel washers fitted with kapton tape, where they were annealed under vacuum at 150° for 18h prior to analysis and allowed to return to room temperature by ambient cooling. SAXS measurements were performed first using a custom-built SAXS diffractometer at the Materials Research Laboratory (MRL) X-ray facility at the University of California, Santa Barbara. As described previously [10], 1.54 ÅCu K α X-rays were generated using a Genix 50 W X-ray microsource (50 μ m micro-focus) equipped with FOX2D collimating multilayer optics (Xenocs, France) and high efficiency scatterless single crystal/metal hybrid slits. 2D SAXS data were collected on a DECTRIS EIGER R 1M area detector with a 1030 x 1065 resolution (DECTRIS, Switzerland). Sample to detector distances were 1.7 m and calibrated with an Ag behenate standard. 2D-data were reduced to a one-dimensional form as a function of the magnitude of the wave vector q,

$\mathbf{q} = \mid \mathrm{q} \mid = 4\pi\ sin(\theta/2)/\lambda$

w here λ is the X-ray wavelength and θ is the scattering angle. Data was converted from 1D to 2D using the NIKA Igor package [90].

SAXS pattern analysis via crystallographic matching

Inorganic crystal structures were obtained from the Inorganic Structure Crystal Database (ICSD) hosted by FIZ Karlsruhe as .cif files and analyzed by Visualization for Electronic and Structural Analysis (VESTA). Briefly, powder diffraction patterns were simulated for each phase of interest and reflections were calculated for a given inorganic analogue (e.g. FeCr for σ phase) in d (Å). The scattering wave vector q was calculated for each reflection through the equation q $= 2\pi/\mathrm{d}$ to yield q^{calc} in $\mathrm{Å}^{-1}$. By dividing q/q^*, relative ratios between each reflection, regardless of unit cell size, were obtained to compare small inorganic atomic structures to large polymer molecule-sized structures. $\mathrm{q}/\mathrm{q}^{*calc}$ was compared to $\mathrm{q}/\mathrm{q}^{*exp}$ to match diffraction patterns of Frank Kasper phases to those obtained experimentally.

5.3 Results and Discussion

Nine linear diblock copolymers (Figure 5.8) were synthesized via controlled radical polymerization around a window of interest, with targeted degrees of polymerization of 15-40 per block, of even composition with the block lengths scaling together. Of the linear diblocks studied extensively by SAXS, all have volume fractions of PTFEA based on homopolymer densities between 28-32 %. The degree of polymerization (DP_{NMR}) was determined by NMR, as in Figure 5.7. Briefly,

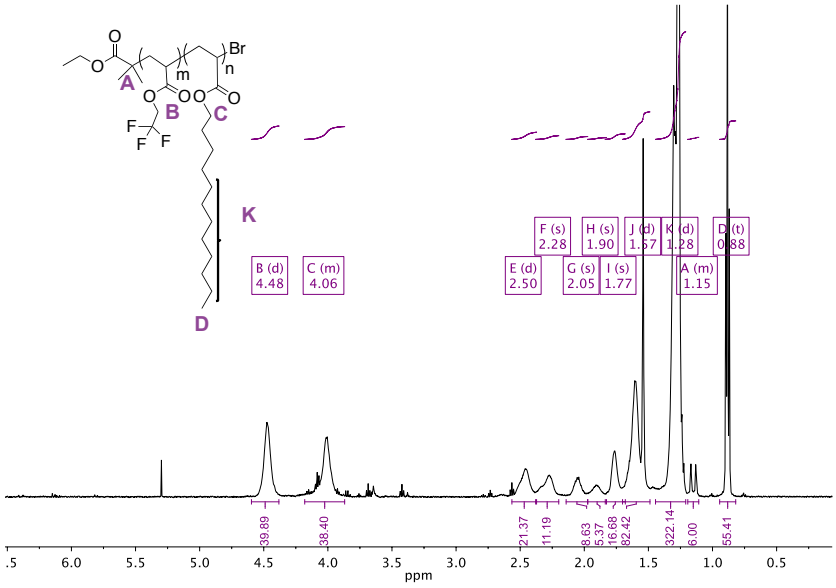

Figure 5.7: Representative NMR showing determination of degree of polymerization of each block of the crude product. ^{1}H NMR (600 MHz, $CDCl_3$): δ 4.48 (m, 39H), 4.06 (m, 38H), 2.50 (d, 21H), 2.28 (s, 11H), 2.05 (s, 9H), 1.90 (s, 5H), 1.77 (d, 17H), 1.57 (d, J =31.6 Hz, 82H), 1.28 (d, J = 18.4 Hz, 322H), 1.19-1.11 (m, 6H), 0.88 (t, J = 6.9 Hz, 55H).

AM2119, where DP_{NMR} of PTFEA-PLAc = 20:19, has a molar mass of M_n = 7.0 kg $\cdot$ mol^{-1} and molar mass distributions of Đ= 1.14. AM2132-2 differs by just a single degree of polymerization, where DP_{NMR} of PTFEA-PLAc = 20:20, has a molar mass of M_n = 7.2 kg $\cdot$ mol^{-1} and molar mass distributions of Đ= 1.11. AM2132-3, is PTFEA-PLAc, with a DP_{NMR} = 24:25, a molar mass of M_n = 8.5 kg $\cdot$ mol^{-1}, and molar mass distributions of Đ= 1.11. The final polymer of this study, AM2132-7, has a molar mass of M_n = 11.0 kg $\cdot$ mol^{-1} and PTFEA-PLAc has DP_{NMR} = 42:41.

Entry	Sample code	f_{PTFEA}[a]	DP_{NMR}[b]	$M_{n,\,NMR}$[c] (block 1, block 2)	$M_{n,\,SEC}$ (block 1, total)	$Đ_{SEC}$ (block 1, total)
1	AM2119	0.32	20:19	3.3, 4.5	2.6, 7.0	1.09, 1.14
2	AM2132-1	0.28	15:17	2.5, 4.1	2.0, 6.2	1.11, 1.10
3	AM2132-2	0.31	20:20	3.3, 4.7	2.5, 7.2	1.09, 1.11
4	AM2132-3	0.30	24:25	3.6, 6.0	2.7, 8.5	1.09, 1.12
5	AM2132-4	0.29	21:22	3.4, 5.3	3.9, 9.2	1.08, 1.14
6	AM2132-5	0.28	29:33	4.7, 7.9	3.2, 10.0	1.08, 1.14
7	AM2132-6	0.28	34:37	5.4, 8.9	3.4, 9.5	1.08, 1.15
8	AM2132-7	0.31	42:41	6.7, 9.8	3.8, 11.0	1.08, 1.15
9	AM2132-8	0.30	38:38	4.2, 11.8	6.0, 9.2	1.07, 1.12

Figure 5.8: Characterization data of poly(trifluoro ethyl acrylate-b-lauryl acrylate). [a]Volume fraction of PTFEA determined by densities of homopolymers PTFEA ($\rho = 1.411$ g $\cdot$ mL^{-1}) and PLAc ($\rho = 0.94$ g $\cdot$ mL^{-1})as reported in the literature. [b]Number-average degree of polymerization of each block determined by ^{1}H NMR end-group analysis. [c]Number-average molar mass determined by ^{1}H NMR.

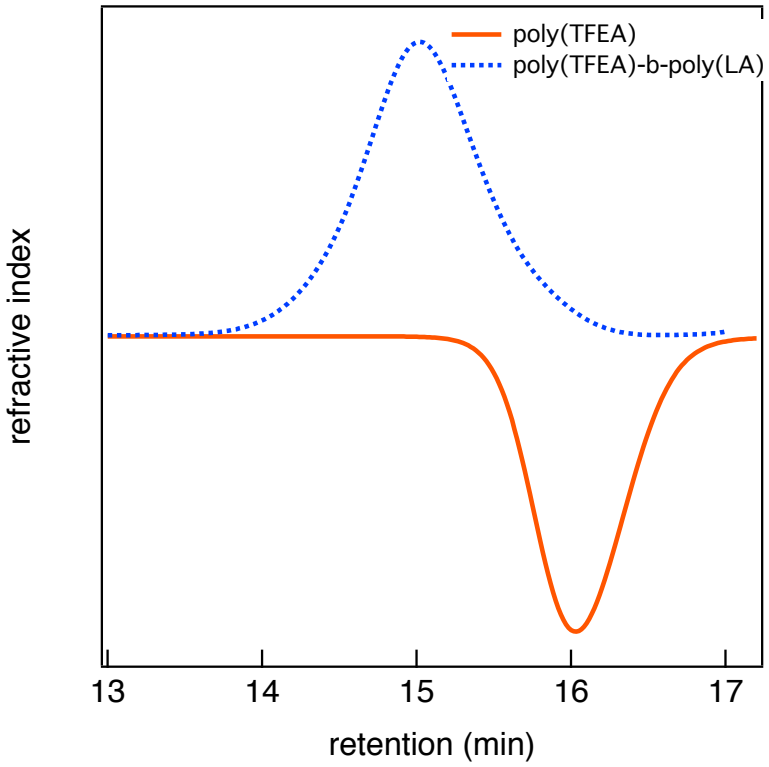

Figure 5.9: Representative SEC traces showing narrow, monodisperse curves for $PTFEA_{20}$-$PLAc_{19}$. The fluorinated block shows a negative refractive index relative to the eluting solvent, chloroform.

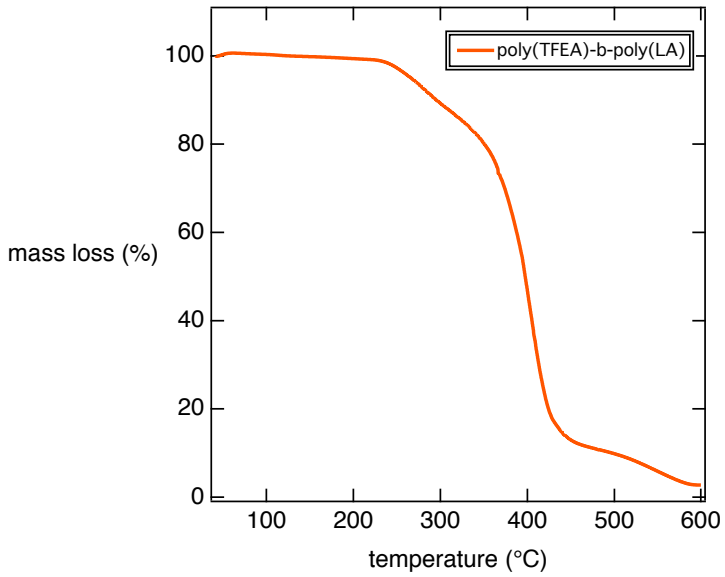

Figure 5.10: TGA of poly(trifluoro ethyl acrylate-b-lauryl acrylate)

5.4 Polymer Characterization

Thermogravimetric analysis (Figure 5.10) shows decomposition of the diblock beginning at 240°C, well below the annealing temperature. TGA experiments were performed under a nitrogen atmosphere at a rate of $10°C \cdot min^{-1}$.

Differential scanning calorimetry (Figure 5.11) indicates a combined melt and crystallization temperature of both PTFEA and PLAc at -2°C and -10°C, respectively. These semi-crystalline polymers exhibit no glass transition temperature. The polymers were viscous and exhibited Frank Kasper phases at room temperature after annealing above the ODT, determined from experiment to be 90°C.

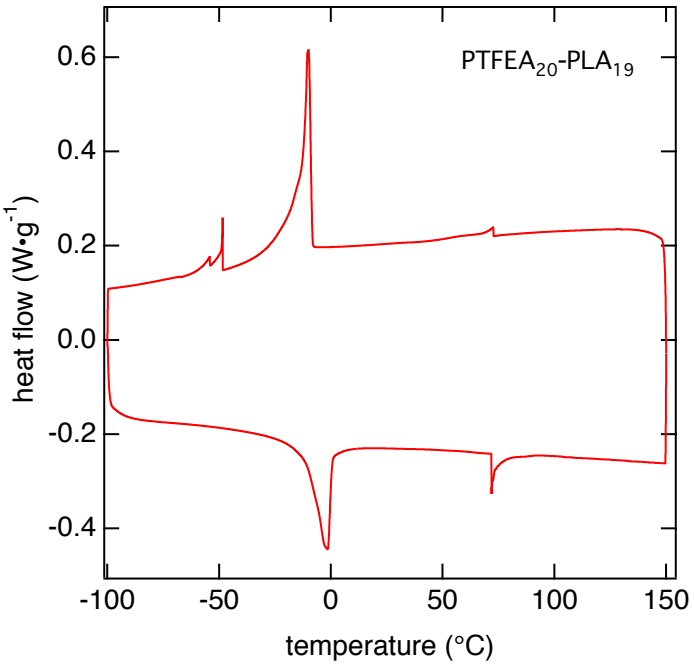

Figure 5.11: DSC of poly(trifluoro ethyl acrylate-b-lauryl acrylate). Data were taken at a scan rate of $5°C \cdot min^{-1}$, data shown from the third cycle (endo down).

Polarizing optical microscopy (POM) was performed on $PTFEA_{20}$-b-$PLAc_{19}$. POM indicates sample crystallinity and orientation by placing a sample between two polarizers that are oriented at a 90° from one another. The absence of an image, such as a completely dark image, indicates the sample is isotropic, with no orientation and lack of crystallinity. The polymer sample was spread on a glass slide and smeared between a coverslip and the slide. The sample was not annealed and contained some air bubbles (the larger circular features seen in some of the optical micrographs, like Figure 5.12. $PTFEA_{20}$-b-$PLAc_{19}$ shows evidence of monoaxial orientation (Figure 5.13). Upon closer magnification, some needle-like crystals can be seen (Figure 5.14). The difference in brightness of the images here is not due to lack of orientation but to the brightness settings on the camera.

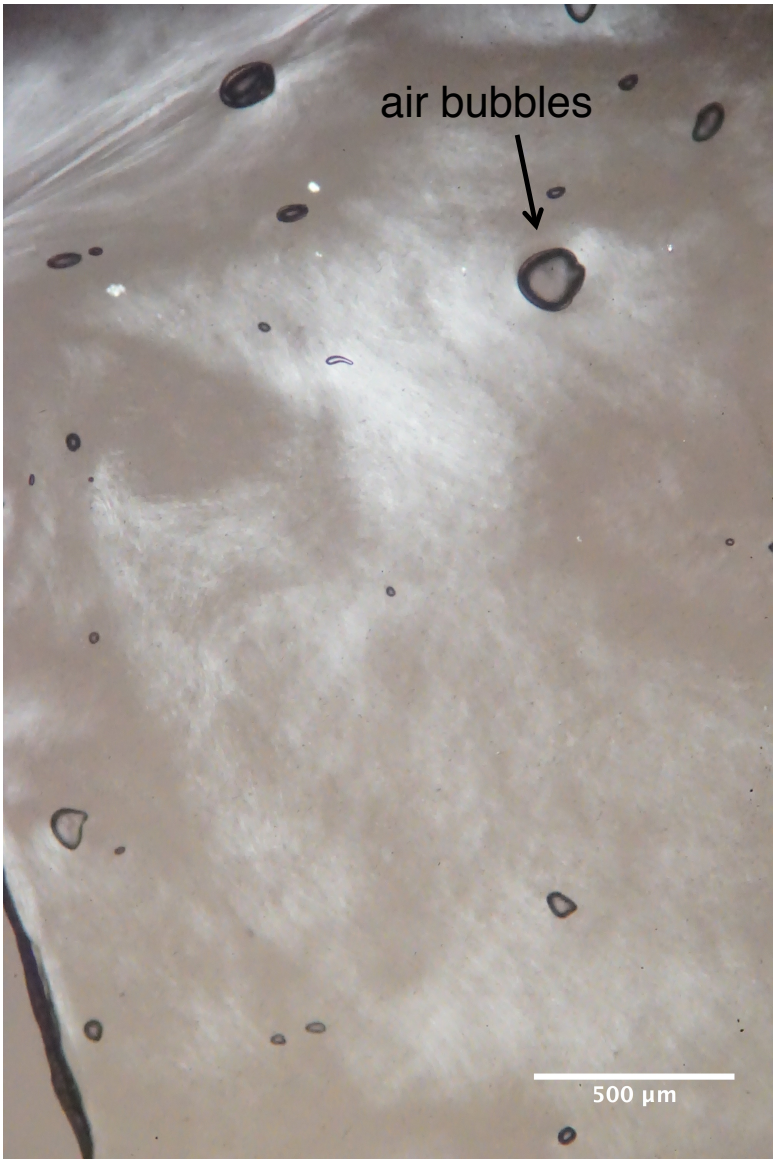

Figure 5.12: A polarizing optical micrograph of $PTFEA_{20}$-b-$PLAc_{19}$ at 5x magnification and room temperature.

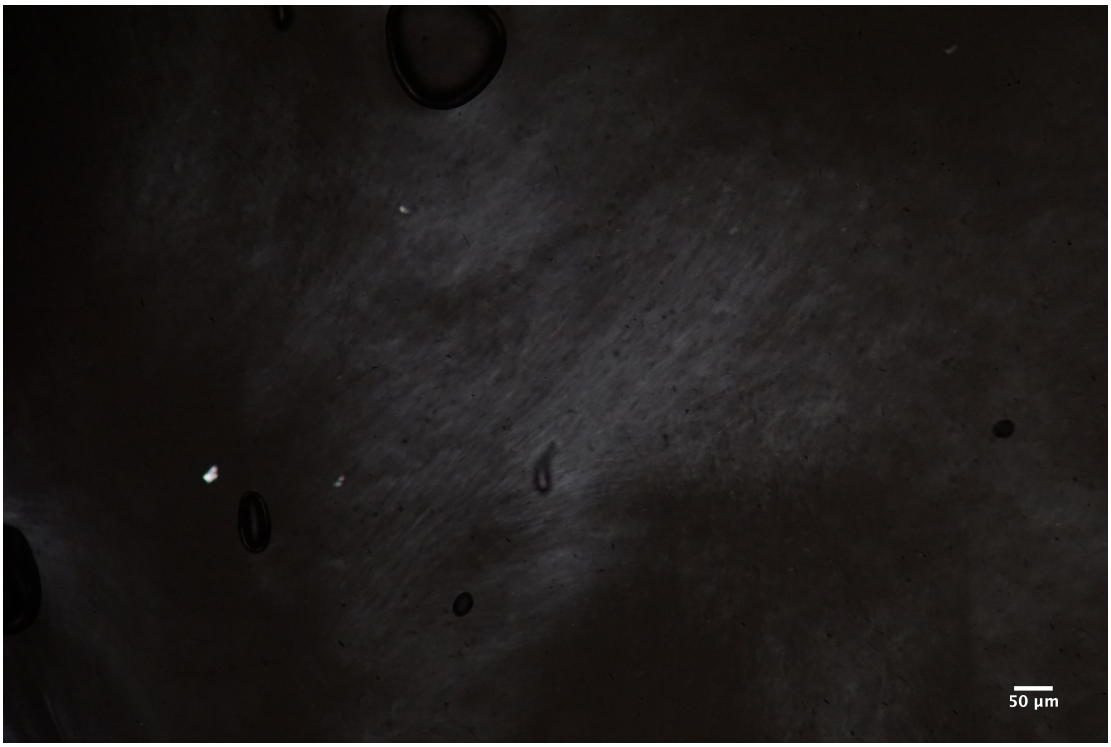

Figure 5.13: A polarizing optical micrograph of $PTFEA_{20}$-b-$PLAc_{19}$ at 10x magnification and room temperature. The sample is anisotropic, shows monoaxial orientation and needle-like crystals.

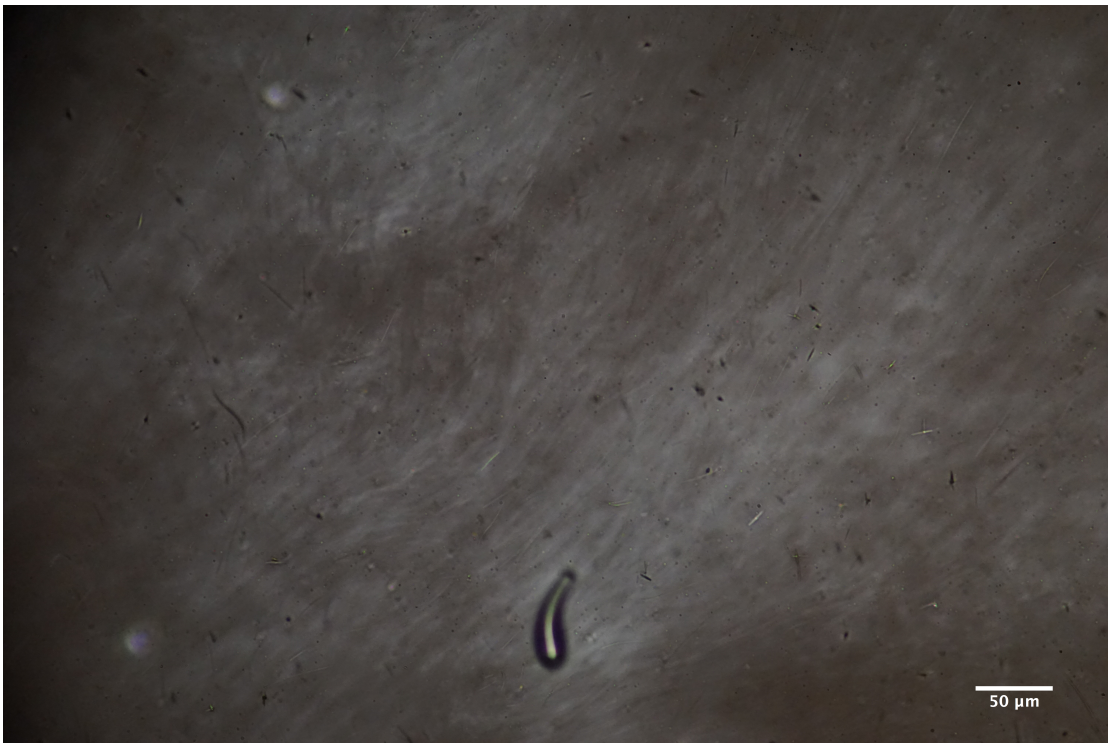

Figure 5.14: A polarizing optical micrograph of $PTFEA_{20}$-b-$PLAc_{19}$ at 20x magnification and room temperature. A dust particle is present in the bottom quadrant.

Small Angle X-Ray Experiments

Small angle x-ray scattering experiments were performed on a home built instrument at the University of California, Santa Barbara as well as on the Stanford Synchrotron Radiation Light Source and Argonne National Laboratory. All samples were annealed at 150°C under vacuum for 18 hours and allowed to return to room temperature through ambient cooling. Figure 5.15 shows $PTFEA_{20}$-b-$PLAc_{20}$ (AM2132-2) diffraction patterns where the lowest-order reflection is q^* = 0.033276 Å. The diffraction pattern calculated for this q/q^* matched q/q^* for A15, with three reflections corresponding to hexagonally packed spheres (hcp) (all allowed reflections in Figure 5.17). Repeat experiments, including a different polymer ($PTFEA_{20}$-b-$PLAc_{19}$) was synthesized and showed the same mixed morphology of A15 phase also stabilized by hcp (Figure 5.24, Figure 5.16 and Figure 5.22). The pattern was stable over time at room temperature.

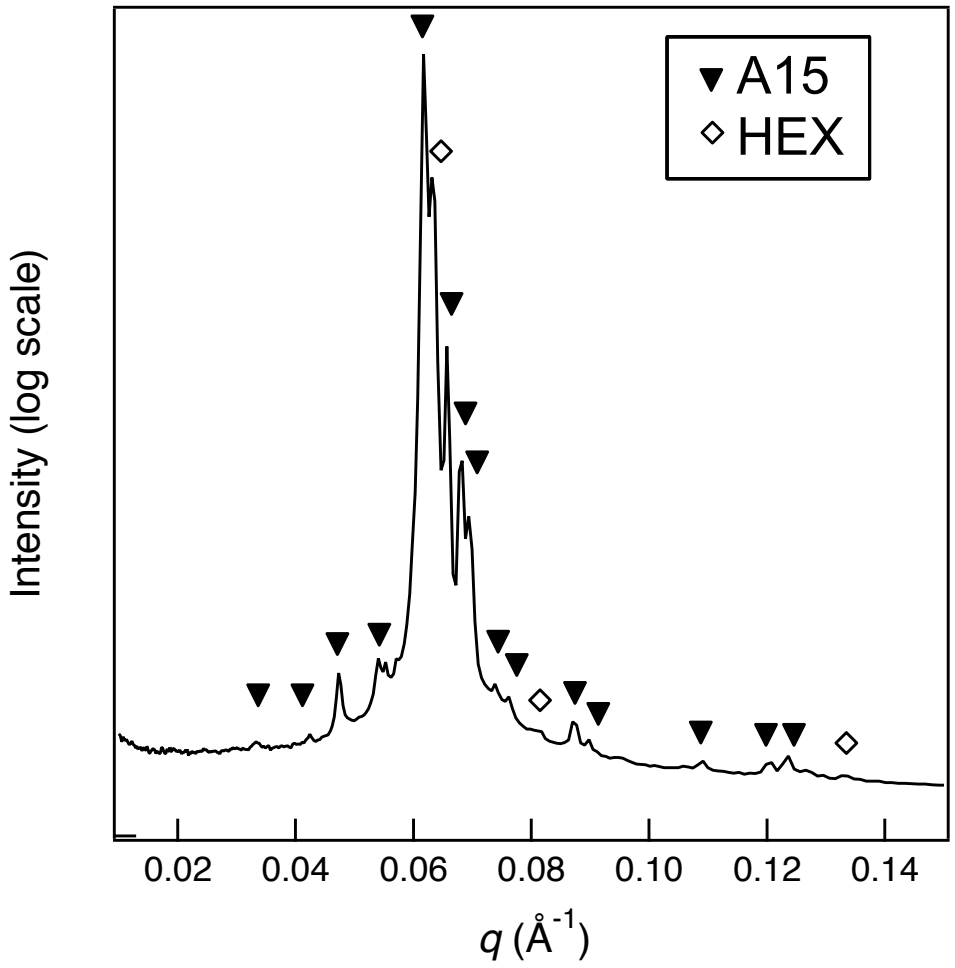

Figure 5.15: Synchrotron SAXS patterns showing A15-hex phase obtained from sample $PTFEA_{20}$-b-$PLAc_{20}$ (AM2132-2) at room temperature.

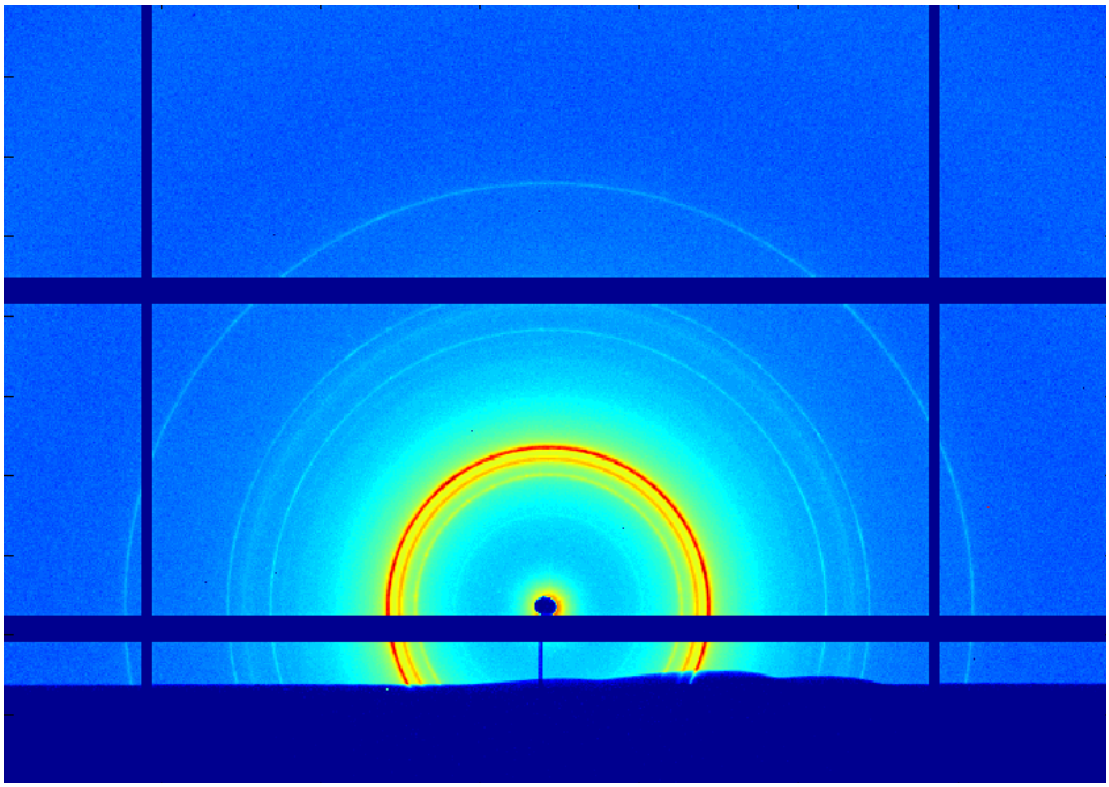

Figure 5.16: Synchrotron SAXS image showing A15 phase in sample $PTFEA_{20}$-b-$PLAc_{19}$ (AM2119) at room temperature°C. SAXS taken at Argonne National Laboratory

hkl	q (calc)	q (obs)
110	0.44721366	--
200	0.632455663	--
210	0.70710684	0.70359877
211	0.774596904	--
220	0.89442732	0.896392777
310	1	1
	1.095445188	--
220	1.140175403	1.142026473
321	1.183215957	1.169091217
440	1.264911325	--
410	1.30384067	1.304203493
330, 411	1.341641338	1.33513765
	--	1.388315643
420	1.414214277	--
421	1.449138503	1.443629213
332	1.483239463	1.466359369
422	1.54919309	1.560916818
430	1.581139157	--
510, 431	1.612452254	1.610457986
432, 520	1.70293837	--
521	1.73205093	1.727766736
440	1.788854639	--
433, 530	1.843909307	1.839197361
531	1.870829437	--
442, 600	1.897366988	1.897555715
610	1.923539343	--
532, 611	1.949359491	--

Figure 5.17: Figure showing all allowed reflections for $PTFEA_{20}$-b-$PLAc_{20}$ (AM2132-2). List of peak positions and peak indices

It appears that $PTFEA_{42}$-b-$PLAc_{41}$ (AM2132-7) forms a majority of hexagonally packed cylinders (hex or p6mm) with a small amount of another phase (minor peaks). At 60°C, major Bragg peak positions where q^* is the tallest peak at 0.043 $Å^{-1}$ show the ratio of q/q^* to be 1, $\sqrt{3}$, $\sqrt{4}$, $\sqrt{7}$, $\sqrt{9}$. At 70°C, the last q/q^* of $\sqrt{9}$ disappears. By 80°C, there is a small peak at low q which is not present at any other temperature, possibly an artifact. Additionally, the presence of some minor intensity peaks, including the significant shoulder peak to the left of the main peak appearing after heating to 50°C (indicating that there is some degree of mixing of another phase), would need longer temperature holds to ascertain whether they are kinetically trapped phases. The steady show of hexagonally packed cylinders through 90°C indicates that this polymer has a different ODT temperature than lower molar mass polymers and that the hexagonally packed cylinders are thermodynamically favored equilibrium for this N.

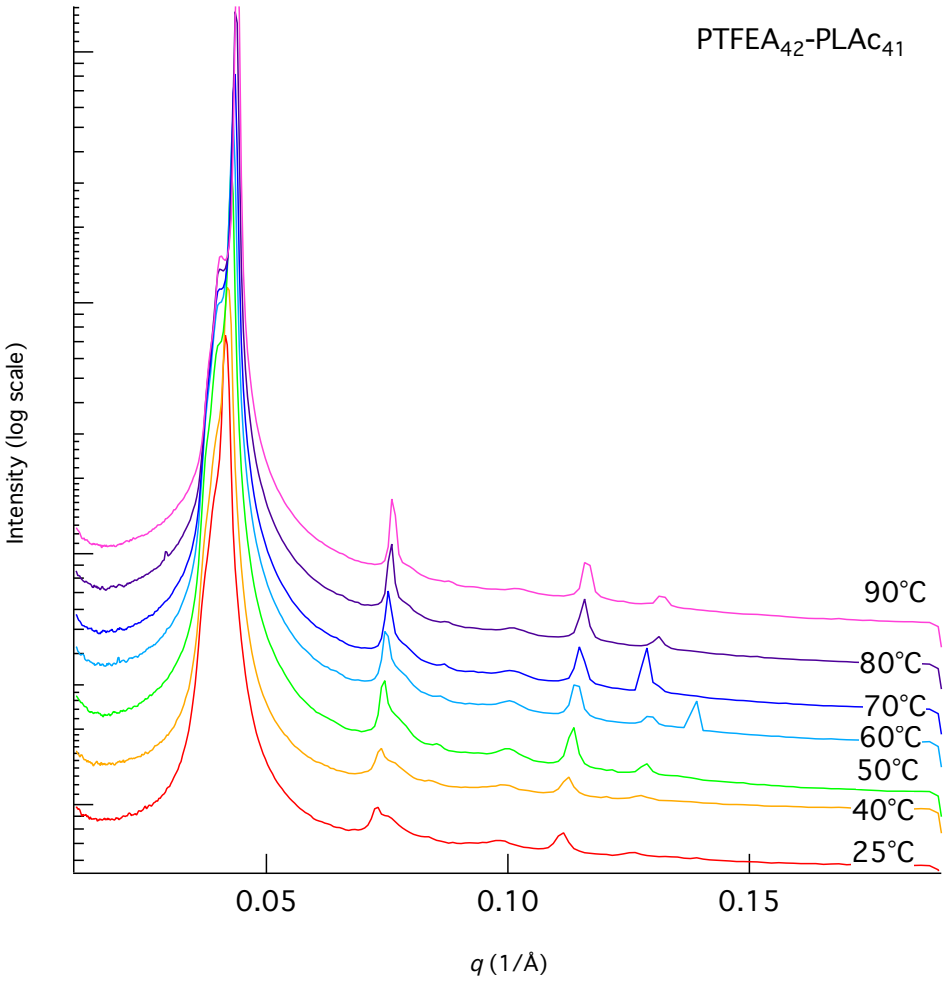

Figure 5.18: SAXS pattern of $PTFEA_{42}$-b-$PLAc_{41}$ (AM2132-7) shows hexagonally packed cylinders, with some variation of peak size based on heating, but no ODT through 90°C.

5.5 Temperature studies

Heating the $PTFEA_{20}$-b-$PLAc_{19}$ (AM2119) sample through 100°C revealed A15-hex from 25°C through 40°C, then some loss of definition to reveal solely hex from 50°C (Figure 5.22) through 80°C, then the ODT to disorder by 100°C (Figure 5.23). Repeat samples of the same composition underwent similar treatment but on first pass by SAXS showed two broad peaks, indicative of trapped morphology. For example, at 25°C $PTFEA_{25}$-b-$PLAc_{24}$ (AM2132-3) showed kinetically arrested liquid-like packing (LLP), Figure 5.19. Minimal heating through 90°C then back down to 45°C revealed a growth of the sigma (σ) phase (Figure 5.20 and Figure 5.21). Figure 5.15 shows a repeat sample run of DP = 20:20 AM2132-2 at SSRL, exhibiting A15-hcp at room temperature without additional heating. High resolution patterns were taken of that sample to confirm the morphology.

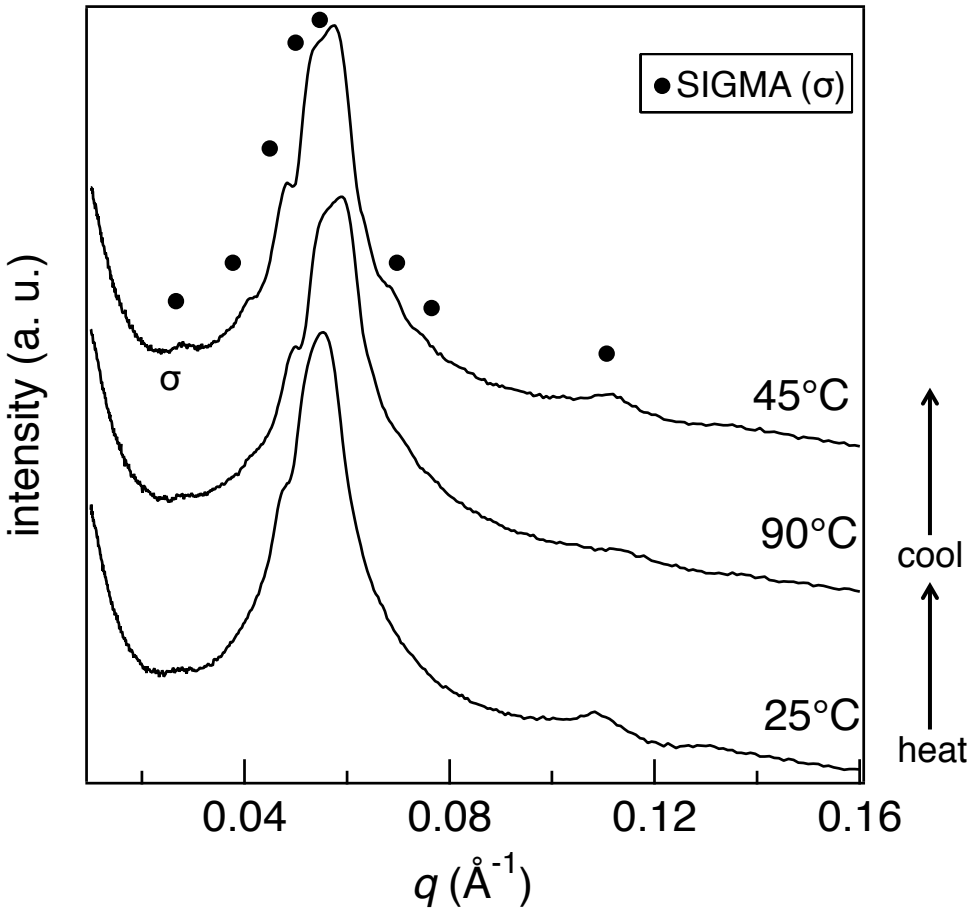

Figure 5.19: SAXS patterns obtained from sample $PTFEA_{25}$-b-$PLAc_{24}$ (AM2132-3) at room temperature and after applying heat and cooling.

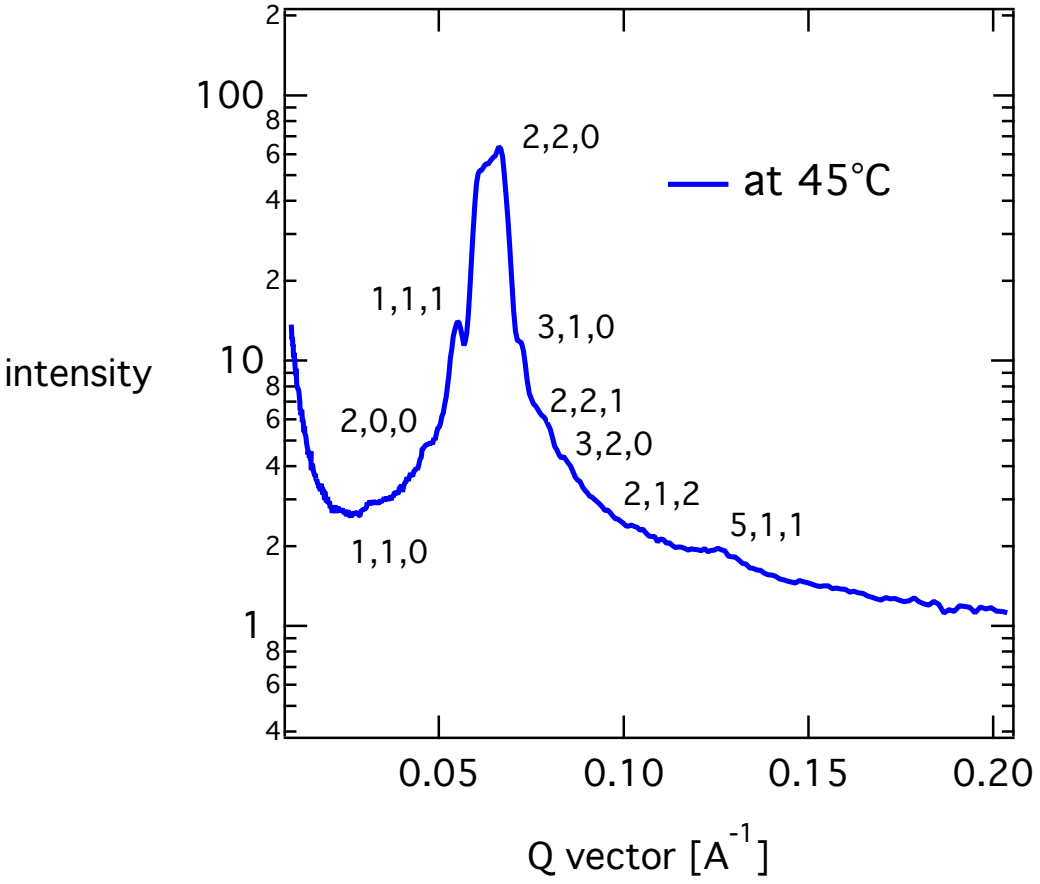

Figure 5.20: SAXS patterns obtained from sample $PTFEA_{25}$-b-$PLAc_{24}$ (AM2132-3) show sigma phase after applying heat, with crystallographic indices listed.

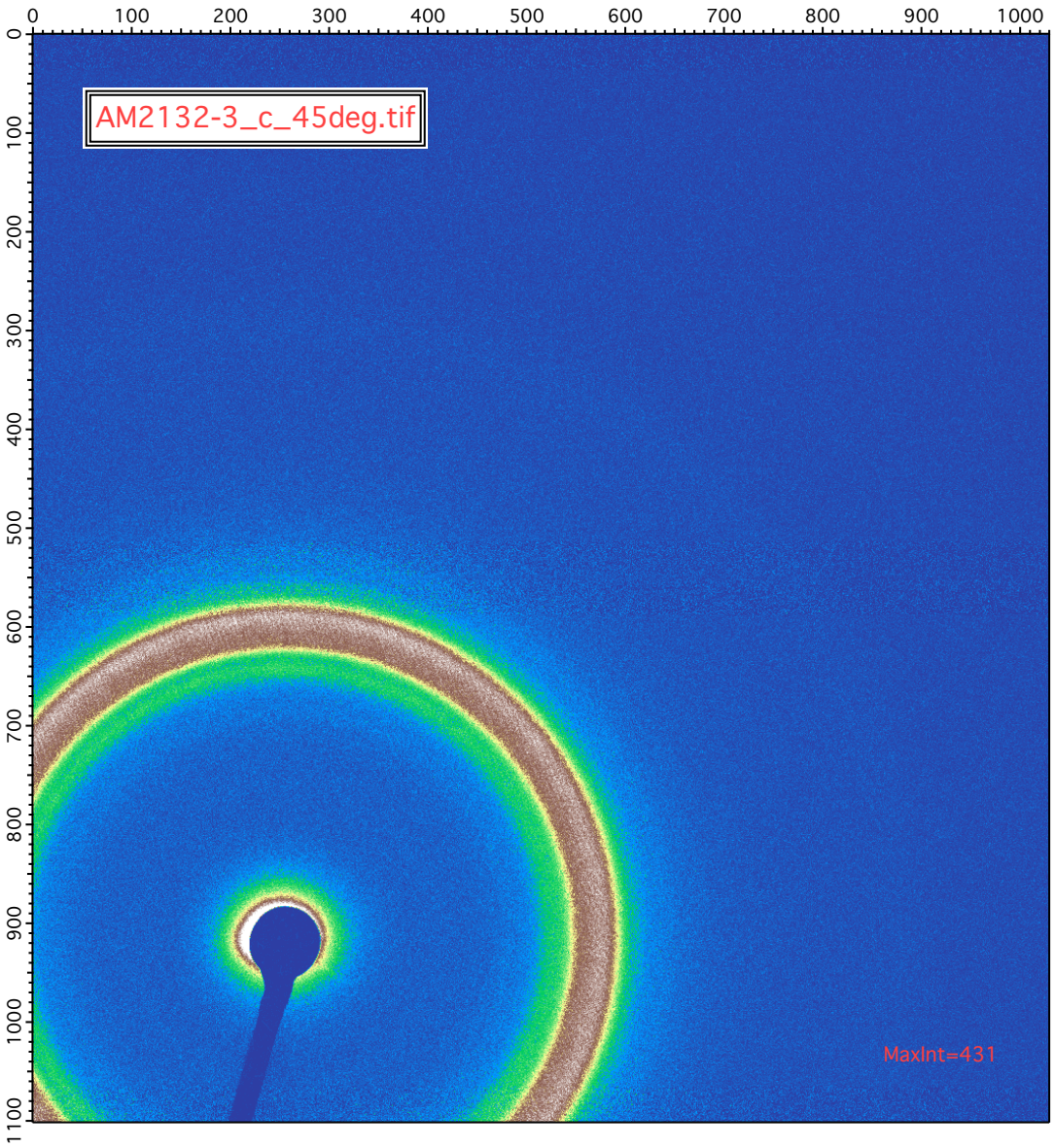

Figure 5.21: SAXS image of $PTFEA_{25}$-b-$PLAc_{24}$ (AM2132-3) at 45°C after cooling from 90°C, 1 hour exposure.

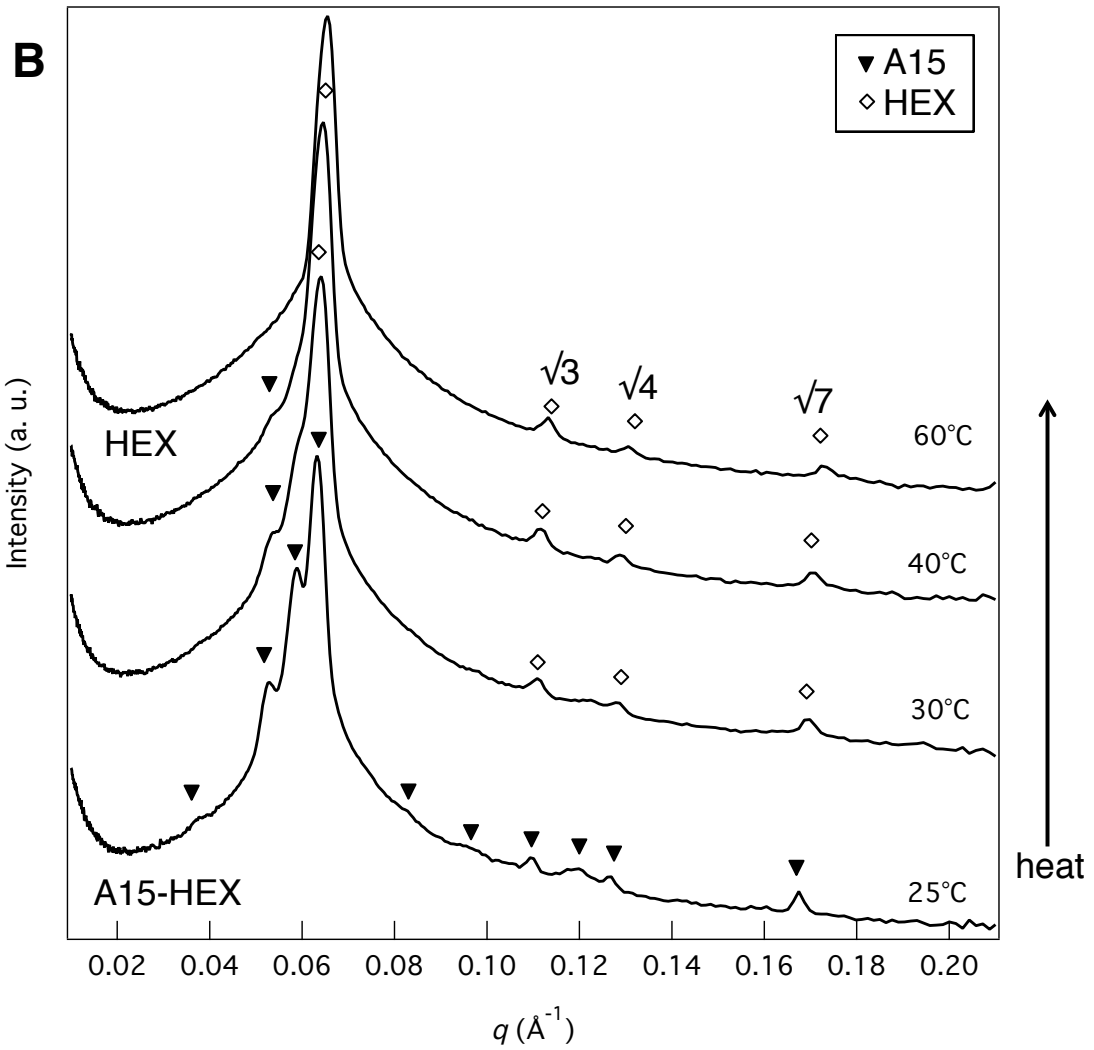

Figure 5.22: SAXS patterns obtained from sample $PTFEA_{20}$-b-$PLAc_{19}$ (AM2119) in part B, heating from 25°C to 60°C shows transition from A15-HEX

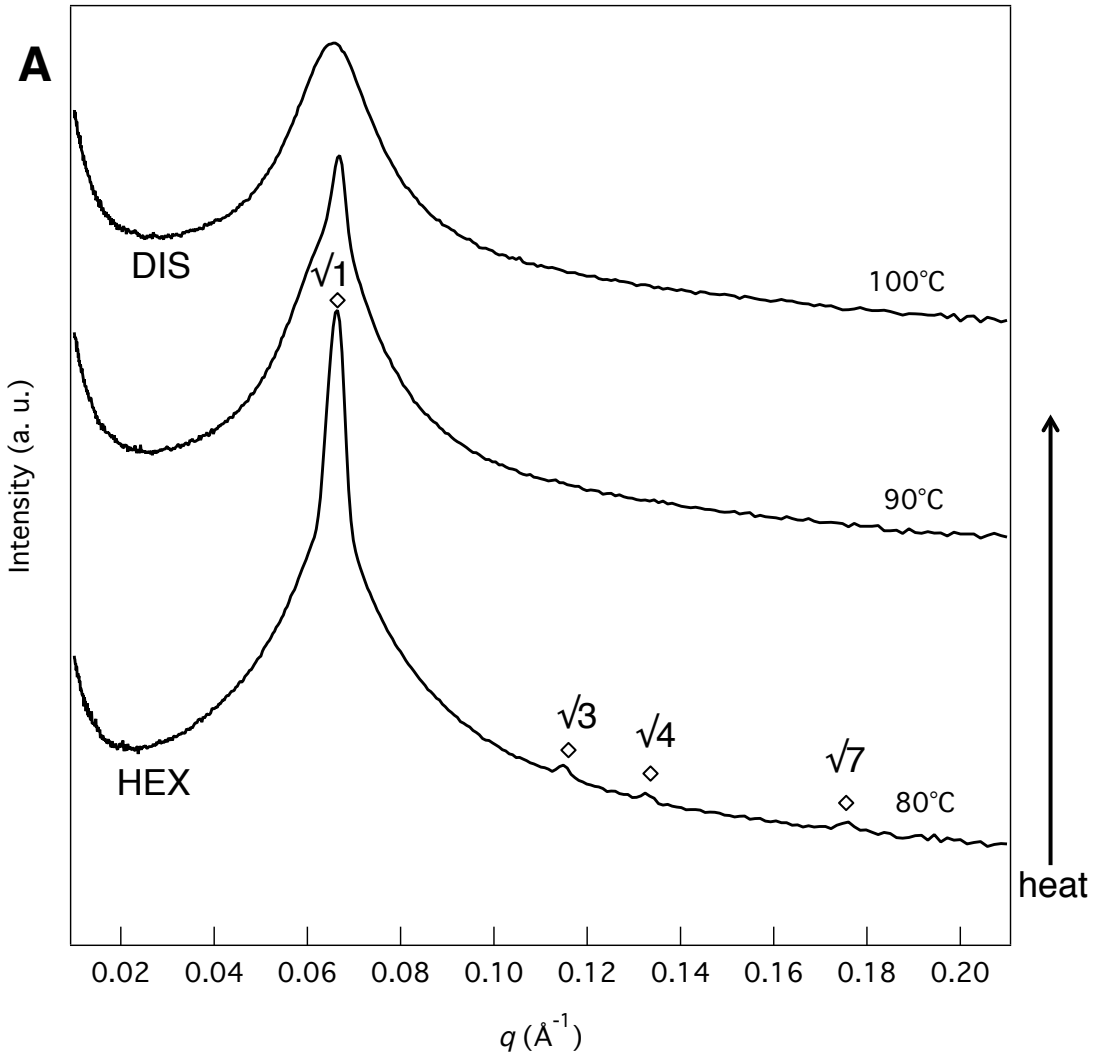

Figure 5.23: SAXS patterns obtained from sample $PTFEA_{20}$-b-$PLAc_{19}$ (AM2119). In part A, heating from 80°C to 100°C shows order-disorder-transition ODT from HEX to disorder

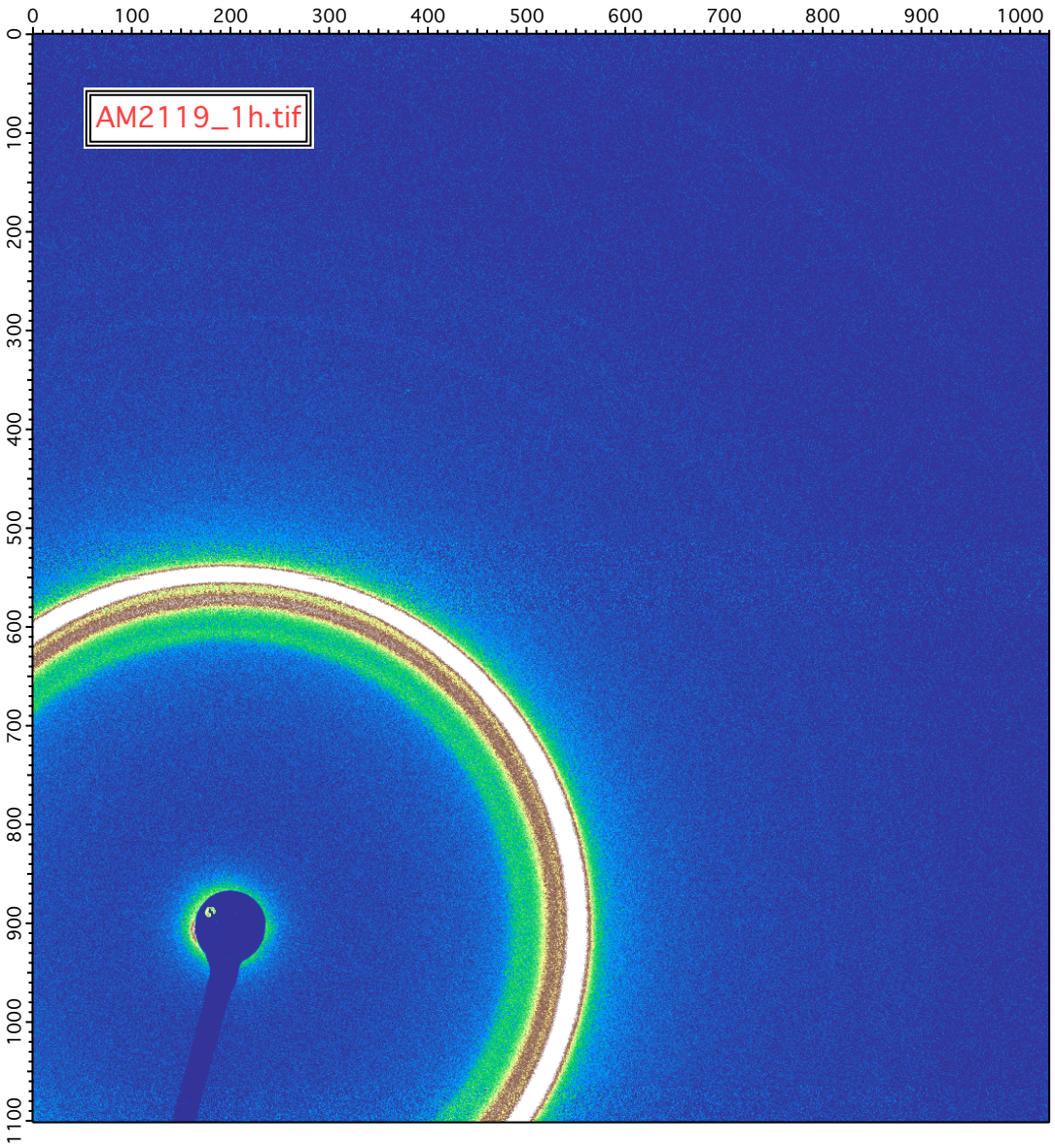

Figure 5.24: Home built SAXS image showing A15-hex phase obtained from sample $PTFEA_{20}$-b-$PLAc_{19}$ (AM2119) at room temperature.

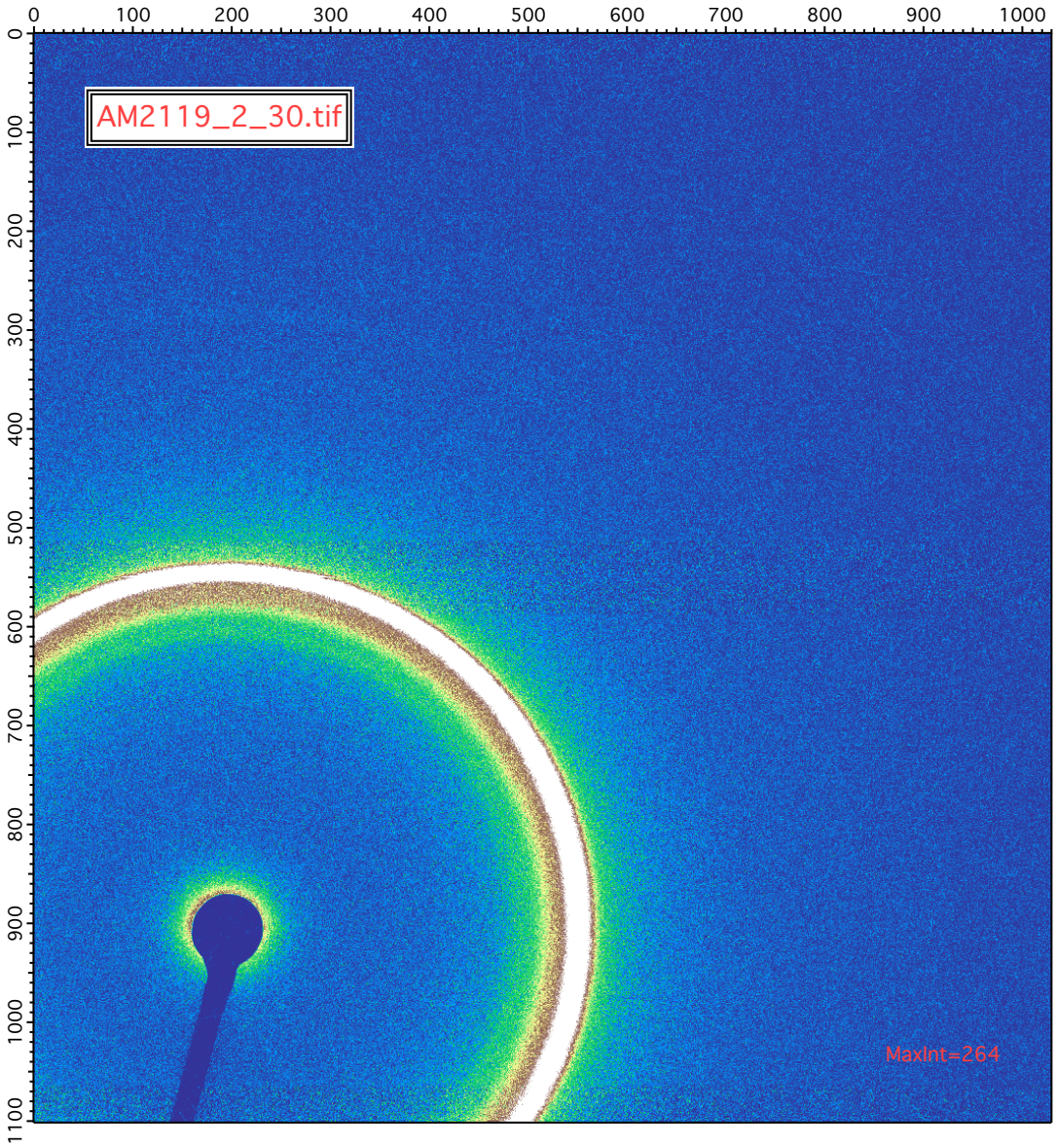

Figure 5.25: Home built SAXS image showing the beginning of morphology changes in sample $PTFEA_{20}$-b-$PLAc_{19}$ (AM2119) at 30°C.

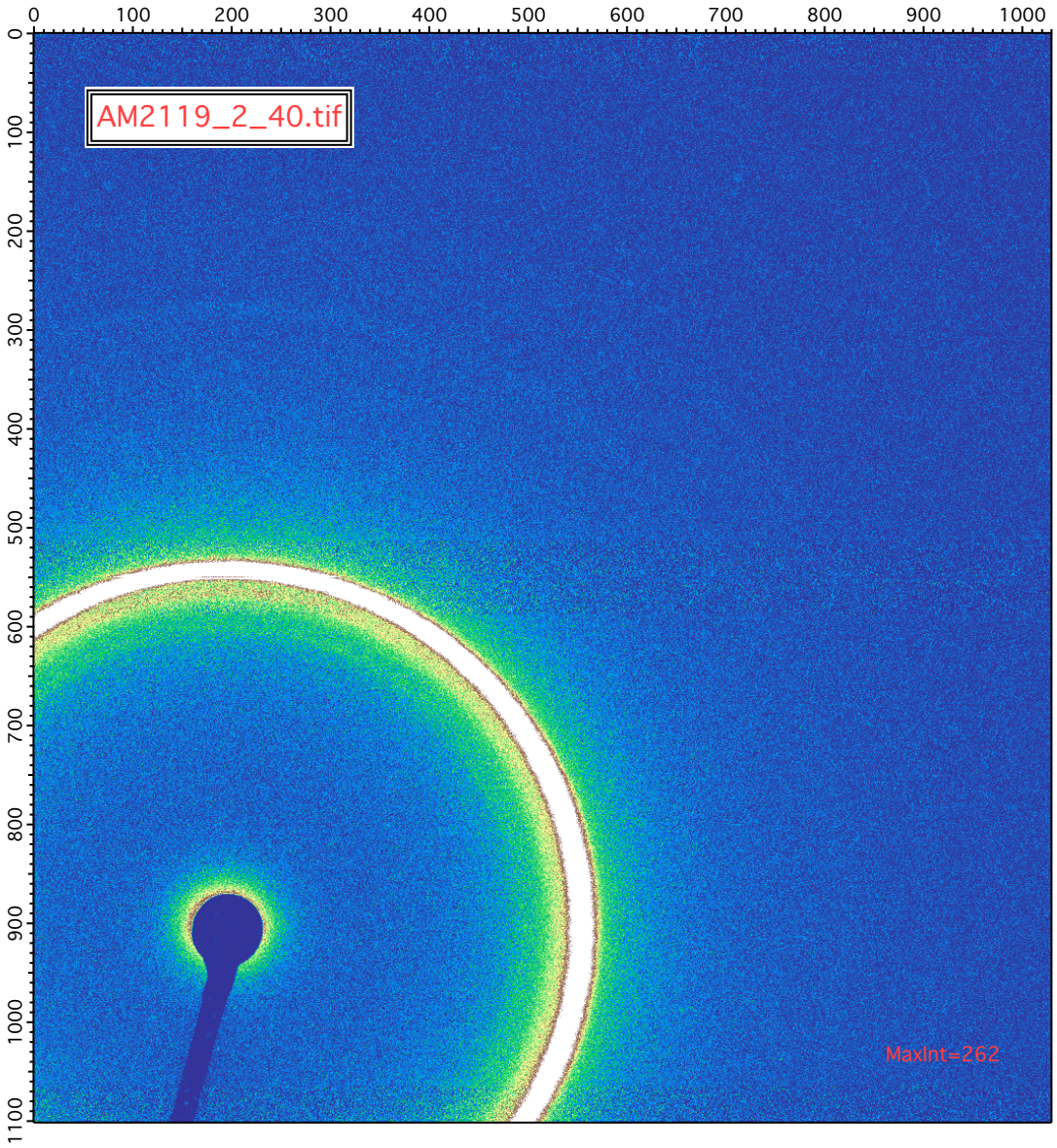

Figure 5.26: Home built SAXS image showing the beginning of morphology changes in sample $PTFEA_{20}$-b-$PLAc_{19}$ (AM2119) at 40°C.

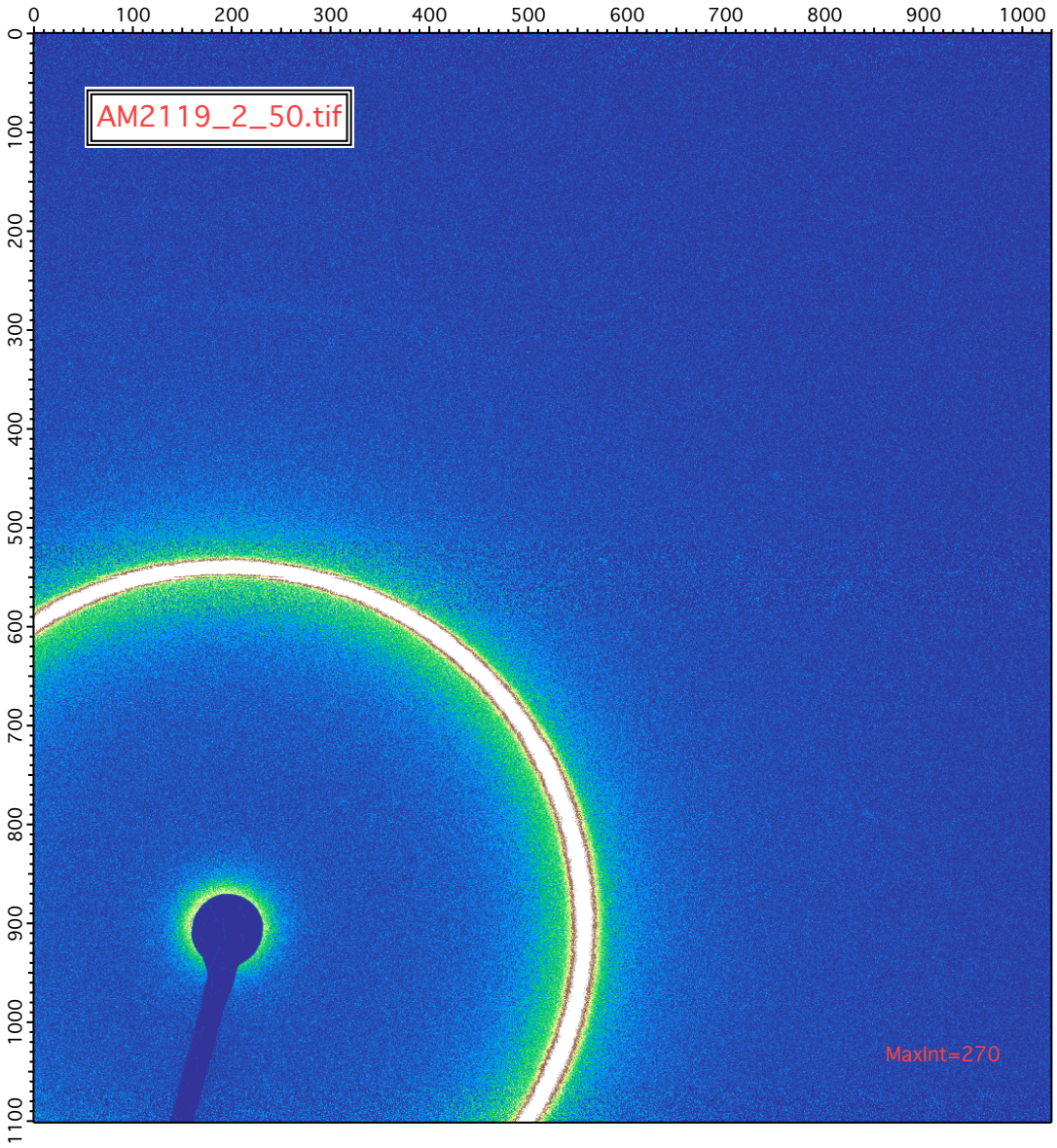

Figure 5.27: Home built SAXS image showing loss of morphology in sample $PTFEA_{20}$-b-$PLAc_{19}$ (AM2119) at 50°C.

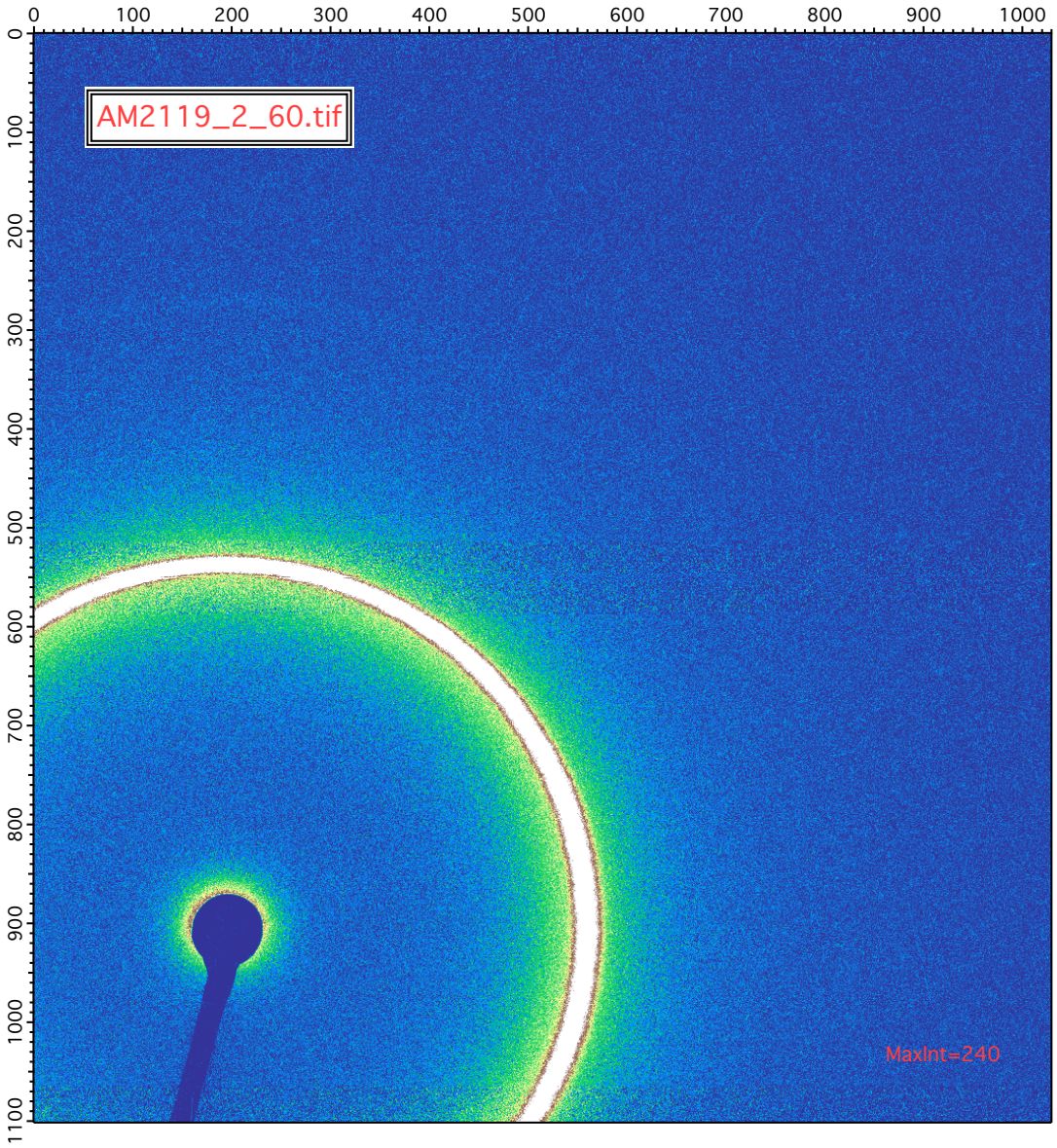

Figure 5.28: Home built SAXS image showing loss of morphology in sample $PTFEA_{20}$-b-$PLAc_{19}$ (AM2119) at 60°C.

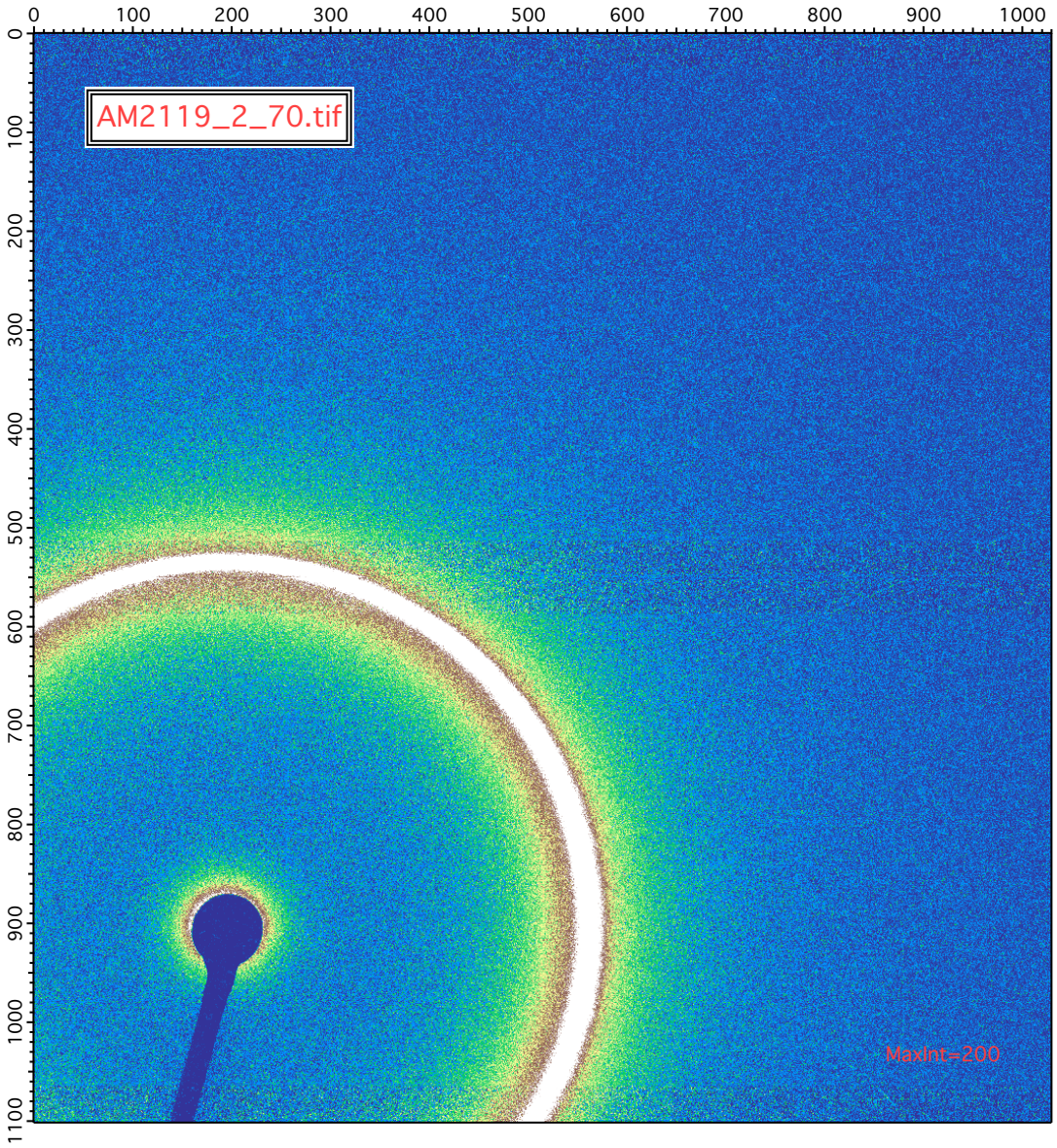

Figure 5.29: Home built SAXS image showing beginning of disorder in sample $PTFEA_{20}$-b-$PLAc_{19}$ (AM2119) at 70°C.

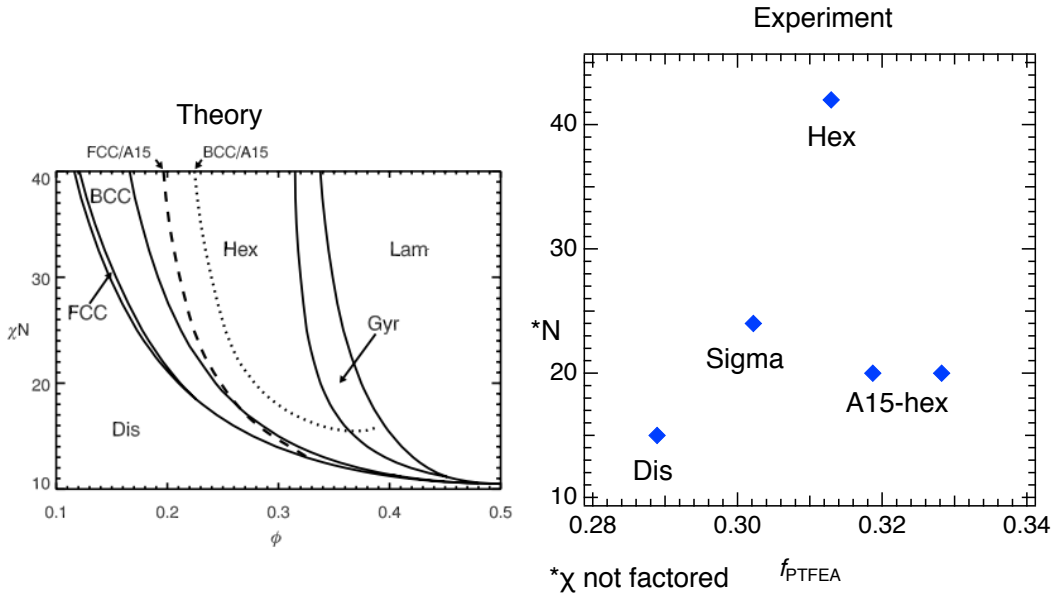

Figure 5.30: A comparison between theory [98] and experimental phase diagrams for the PTFEA-b-PLA polymers tested by SAXS.

5.6 Comparison of Experiment to Theory

In the region between N = 15-40, a close match between theory and experiment is found, comparing [98] to the polymers synthesized and tested by SAXS. At N = 15, the polymer is disordered. Increasing to N = 20, the A15-hex phase is found. At N = 25, sigma phase is found with the addition of heat, while increasing to N = 42, hexagonally packed cylinders are found and stable over a range of temperatures through 90 °C. Expanding through the phase diagram will likely show the typical diblock phases, including lamellar, gyroid, BCC, and FCC. Here, a complex phase diagram is shown for the spherical phases.

5.7 Conclusion

Conclusive evidence herein demonstrates the possibility to unravel unique polymer morphology with patient studies around degrees of polymerization of interest. Recent work in the field has shown that there are many phases, such as the numerous Frank Kasper phases, that are yet to be uncovered by using temperature studies, discrete polymers, and high resolution SAXS. Accordingly, diligent polymer chemists should team up with theoreticians to advance the field. Interesting phases are not only difficult to discover through experiment, a lump on a low resolution SAXS can be ignored as a fluke in a one-pass experiment. Guaranteed success is hard to come by, and close discussions with physical chemists is the best way forward in designing experiments and targeting which polymers to make.

The A15 phase has been shown to be one of the most simple complex structure in metals, where it is found in Cr_3Si. [106] Observations in metals indicate that the A15 stability depends on the electronic structure of the d bands. [104] Laves phases, on the other hand, are one of the more complex structures and can be less easily recognized. Determining the phase morphology is difficult for polymer chemists who may be unfamiliar with inorganic crystal structures, and might not immediately match the phases to known crystal structures. More overlap between inorganic chemists, polymer theoreticians, and polymer chemists is needed to ensure that all possibilities are explored. Essentially, a library of phases for polymers, just as those that exist for X-Ray Reflectivity Diffractometry of inorganic materials, must be made with an eye toward flexible radii of polymer blocks. Not only will this help with identifying phases, it will open up the field of

polymer physics to overlap with other fields more closely. Other fields have greatly benefited from digitizing the analysis of data with algorithms. The opportunities for future work here are endless.

The one problem untold between literature interest, society's hopes for technology is the sheer size of the work that needs to be done in order to understand and control the physical packing of new polymers. A push towards high throughput polymerization, such as that which has been done with synthetic peptoid work and their morphology characterization, [107] can be a great way to achieve these goals.

Chapter 6

Well-defined star polymers via Cu(0)-mediated reversible-deactivation radical polymerization

6.1 Introduction

Star polymers are branched macromolecules of diverse architectures that have attracted significant attention in both industry and academia. They are classified as having at least three linear polymer chains or "arms" connected to a single core. Compared to linear analogues, star polymers can exhibit different viscosities, lower hydrodynamic volumes, and relatively minimal chain entanglements. [108] Due to these characteristics, star polymers are used in a wide range of applications:

as polymer therapeutics, MRI contrast agents, drug delivery vehicles, nanoreactors for inorganic nanoparticle synthesis, viscosity modifiers, and cosmetic additives. [89, 108, 109, 110, 111, 112] Star polymers can be synthesized via controlled radical polymerization through three synthetic approaches, called "arm first," "grafting onto," and "core first." Among the synthetic techniques available, star polymers are most often prepared using copper-mediated approaches, including conventional atom transfer radical polymerization (ATRP) [113, 114] and Cu(0), also referred to as single electron transfer living radical polymerization (SET LRP), [16] ring opening polymerization (ROP), [115] and reversible addition-fragmentation chain transfer (RAFT) polymerization. [116, 117, 118, 119] In both the "arm first" and "grafting onto" approaches, linear polymers are first synthesized and then attached together through cross-linking or coupling chemistries to form star polymers. In this way, each polymer arm has a known chain length and molar mass prior to coupling. However, these techniques are plagued by both broad molar mass distributions, due to statistical distributions of the number of arms per molecule, and the need for extensive purification to remove any unreacted linear polymers. [108] As such, the "core first" strategy has attracted significant attention due to the excellent yields of pure star polymers with a known number of arms from multifunctional cores via a simple purification process to remove monomer and other small molecules. However, an on-going drawback of the latter strategy, especially when combined with reversible-deactivation radical polymerization RDRP (e.g. ATRP), is the propensity for deleterious side reactions such as bimolecular star-star coupling and disproportionation. [120, 121, 122] Size Exclusion Chromatography (SEC) analysis shows evidence of these side re-

actions, indicating undesired variable star architectures. The tendency towards these side reactions is not surprising, given that star polymers inherently contain multiple propagation sites relative to their linear analogues and are statistically more likely to undergo radical-radical termination events. These unwanted events become even more probable over time, at high monomer conversions, or when higher molar masses are targeted.

To address these challenges, star polymerizations are typically stopped at low monomer conversions (e.g. 10-40 %) before any severe coupling events occur. [109,123,124] Alternatively, synthesis can also be conducted under extremely dilute conditions (e.g. 1-10 wt% of the monomer) to reduce intermolecular couplings. Both of these strategies are wasteful of starting materials, inspiring polymer chemists to find better methods. Whittaker and co-workers partially addressed these issues by using an excess of $CuBr_2$ deactivator (0.16 eq. per arm) in dimethylsulfoxide (DMSO), although these star multi-block copolymers were confined to low molar masses (M_n <10,000). [125] In addition, Haddleton and co-workers reported that star-star coupling could be suppressed by designing a system in which the star polymers phase separate from the reaction medium allowing for the synthesis of polymers with a significantly improved degree of control. However, this strategy was limited in scope to a particular solvent and monomer combination, and no star block copolymers were demonstrated. [126, 127]

To widen monomer scope, accessible molar masses, and arm topologies in the preparation of well-defined star polymers, we utilize Cu(0)-wire RDRP [128, 129, 130, 131, 132] to prepare star polymers via the "core first" approach. Through careful optimization of reaction conditions, trifluoroethanol (TFE) was found to

be an optimal solvent as it can maintain the critical balance between catalyst and polymer solubility while simultaneously minimizing star-star coupling. With the use of parts per million (ppm) concentrations of copper, tetra-, octa- and cyclodextrin-based initiators were used for the synthesis of a breadth of well-defined star polymers. All polymerizations exhibited near quantitative monomer conversions (>95 %) and narrow molar mass distributions (Đ$\sim$ 1.1) with minimal star-star coupling, even for higher molar mass stars, up through degrees of polymerization per arm, $\mathrm{DP}_{per\ arm}$, is equal to 600, and the M_n = 171,000 g·mol^{-1}.

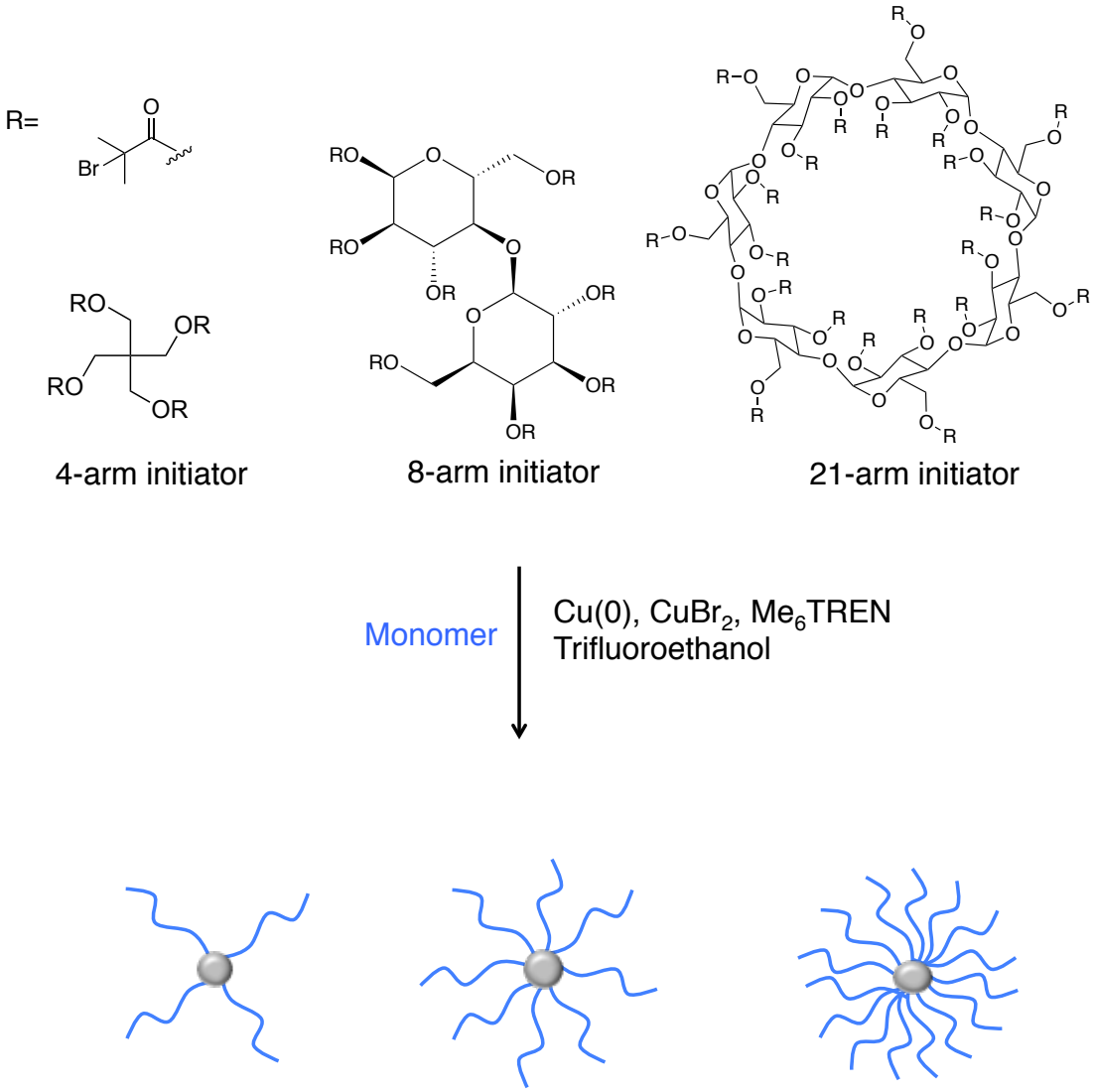

Figure 6.1: Synthesis of polyacrylate star polymers via Cu(0) RDRP in TFE. Chemical structures of the multifunctional 4-, 8-, and 21-arm ATRP initiators are shown, where R is 2-bromo-2-methylproprionate.

6.2 Materials and Methods

Materials

Methyl acrylate (MA) (99 %), *tert*-butyl acrylate (tBA) (98 %), hexyl acrylate (HA) (98 %), and butyl acrylate (nBA) (99 %) were purchased from Sigma Aldrich and passed through a column of basic alumina (150 mesh, Brockmann I grade) just prior to use. Reagent grade solvents were used as received: 2,2-trifluoroethanol (TFE) and dimethyl sulfoxide (DMSO) were purchased from Sigma Aldrich and acetonitrile (MeCN), N,N-dimethyl formamide (DMF), N-Methyl-2-pyrrolidone (NMP), tetrahydrofuran (THF), pyridine (anhydrous), dichloromethane (DCM), ethyl acetate, isopropanol (IPA) and toluene were purchased from Fisher Scientific. Copper(II) bromide ($CuBr_2$) (99 %), tris[2 (dimethylamino)ethyl]amine (Me_6-TREN) (97 %), β-cyclodextrin, and 2,2-trifluoroethyl acrylate (TFEA) were purchased from TCI America and used as received. β-Lactose, 2-bromoisobutyryl bromide (EBib), pentaerythritol, and triethylamine were purchased from Sigma Aldrich and used as received. Copper (0)-wire (0.25 mm gauge) was purchased from Comax Engineered Wires.

Characterization

Nuclear magnetic resonance (NMR) spectra were recorded on a Varian 600 MHz spectrometer using $CDCl_3$ or CD_3OD as the solvent. Analysis of number average molecular weights (M_n) and weight average molecular weights (M_w) was performed via size exclusion chromatography (SEC), relative to linear polystyrene standards, on a Waters 2690 separation module equipped with Waters 2414 refractive index and 2996 photodiode array detectors. $CHCl_3$ containing 0.25 % triethylamine was used as the eluent at a flow rate of 1 mL $\cdot$ min^{-1}. Fourier

Transform Infrared (FTIR) spectra were collected on a Nicolet is10 FTIR spectrometer with a Smart Diamond ATR accessory from Thermo Fisher Scientific. Electrospray ionization spectra were taken on a Waters Xevo G2-XS TOF mass spectrometer with ESI source.

Synthesis of 4-arm ATRP initiator

The four arm initiator was synthesized according to the literature. [133] All glassware was flame dried before use and Argon flow was present during addition of EBib, and the remainder of the reaction was performed under an Argon atmosphere. 2-bromoisobutyryl bromide (5 eq., 25 g, 0.11 mol) dissolved in 80 mL of dry THF was added dropwise to another solution containing pentaerythritol (1 eq., 3.0 g, 0.022 mol) and triethylamine (5 eq., 11 g, 0.11 mol) dissolved in 220 mL of dry THF at 0 °C. The reaction was allowed to stir for 6 h and then filtered to remove the salts. The filtrate was concentrated by rotary evaporation. The crude product was dissolved in 300 mL ether and sequentially washed with (3 x 100 mL) 10 wt % HCl, (3 x 100 mL) saturated $NaHCO_3$ solution, and brine. The organic layer was collected, dried over anhydrous $MgSO_4$, and filtered. The filtrate was concentrated by rotary evaporation. The concentrate was purified by silica gel column chromatography using ethyl acetate/petroleum ether (1/6, v/v) as the eluent. Yield: white crystals, 10 g, 65 %.^{1}H NMR (600 MHz, $CDCl_3$): δ 1.94 (s, 24H), 4.33 (s, 8H). ^{13}C NMR (150 MHz, $CDCl_3$): δ 171.04, 63.04, 55.34, 43.82, 30.79.

Synthesis of 8-arm ATRP initiator from lactose

A synthetic protocol was adapted from previous literature reports. [134] β-Lactose (1 eq., 5.0 g, 0.015 mol) was dissolved in a mixture of anhydrous pyridine

(33 mL) and anhydrous DCM (33 mL) under nitrogen atmosphere and cooled in an ice bath to 0 °C. 2-bromoisobutyryl bromide (9.6 eq., 17 mL, 0.14 mol) was dissolved in 17 mL anhydrous DCM and slowly added dropwise with an addition funnel to the cooled lactose mixture. The reaction was allowed to warm to room temperature and react for 72 h with stirring. The mixture was then diluted in DCM and washed first with ice water, then (3 x 100 mL) aqueous saturated $NaHCO_3$, and then again with H_2O. The organic layer was collected, dried over $MgSO_4$, and concentrated by rotary evaporation to yield orange syrup. The product was recrystallized from ethanol to yield a white powder. Yield: 1.25 g, 5.6 %. ^{1}H NMR (600 MHz, $CDCl_3$) δ 6.32 (d, J = 3.7 Hz, 1H), 5.63 (t, J = 9.9 Hz, 1H), 5.49 (d, J = 3.2 Hz, 1H), 5.25 (dd, J = 10.5, 8.1 Hz, 1H), 5.08 (dd, J = 10.3, 3.8 Hz, 1H), 5.01 (dd, J = 10.5, 3.3 Hz, 1H), 4.74 (d, J = 8.1 Hz, 1H), 4.69 (dd, J = 12.9, 2.7 Hz, 1H), 4.48 (dd, J = 12.8, 2.1 Hz, 1H), 4.42 - 4.29 (m, 2H), 4.27 - 4.13 (m, 3H), 2.06 - 1.84 (m, 45H), 1.77 (s, 3H). MS (ESI, *m/z*): [M + H] + calcd for C_{44} H_{62} Br_8 O_{19}: 1533.73; found, 1533.9.

Synthesis of 21-arm ATRP initiator from β-cyclodextrin

A synthetic protocol was adapted from previous literature reports. [135, 136] To a dry 100 mL round bottom flask fitted with an addition funnel and in an ice bath was added β-cyclodextrin (1 eq., 1.1 g, 0.003 mol), stir bar, and 10 mL anhydrous NMP. In a separate flask, 2-bromoisobutyryl bromide (42 eq., 10 mL, 0.13 mol) and 5 mL anhydrous NMP were added and stirred until thoroughly mixed; this was then introduced to the addition funnel and added dropwise to the reaction flask. The reaction was allowed to warm up to room temperature overnight and let react for 72 h. The reaction mixture was diluted with 50 mL

DCM, washed first with (2 x 100 mL) aqueous saturated $NaHCO_3$ and then with (2 x 100 mL) H_2O. The organic layer was concentrated under reduced pressure and dried overnight under vacuum, followed by dialysis (MWCO = 2000) against DI H_2O for several days until white and brown sediment settled in the dialysis tubing. The brownish/white precipitate was dissolved in DCM, dried over $MgSO_4$, filtered, and redissolved in minimal DCM. The product (herein referred to as cyclodextrin-initiator or CD-initiator) was then precipitated in cold hexanes to yield a white powder. Yield: 1.68 g, 14 %. FTIR cm^{-1}: 2991 -2910 (ν_{C-H}), 1737 ($\nu_{C=O}$), 1150 (ν_{C-O-C}), 1034 and 1102 (ν_{C-C} and ν_{C-O}). ^{1}H NMR (600 MHz, $CDCl_3$): δ 1.19 (d, J = 86.8, 2H), 2.35-1.60 (m, 126H), 5.89-3.54 (m, 49H). MS (ESI, *m/z*): [M] + calcd for C_{126} H_{175} Br_{21} O_{56}: 4264; found, 3992.

General synthesis of star polymers from multi-arm initiators via Cu(0) RDRP

The synthesis of PtBA, PMA, PHA, and PnBA were performed at room temperature using either the 4-, 8-, or CD- initiators. A typical reaction to prepare 4-arm PtBA stars with 37 repeat units per arm, [M]/[I]=150, contained: 5 cm of copper wire, 1 eq. of initiator (0.039 g, 0.055 mmol), 150 eq. of tBA (1.2 mL, 8.2 mmol), 0.05 eq. of $CuBr_2$ (0.6 mg, 0.027 mmol; 0.0125 eq. per CH-Br), 0.72 eq. of Me_6TREN (0.0026 mL, 0.040 mmol; 0.18 eq. per CH-Br), and 1.2 mL of solvent (TFE, MeCN, toluene, DMSO, or DMF, all 1:1 with the monomer). The copper wire was first activated in HCl for 10 minutes, rinsed with acetone, and wrapped around a stir bar. $CuBr_2$, solvent, and Me_6TREN were added in that order to a glass reaction vial and sonicated until the mixture turned a bright green color and all of the $CuBr_2$ was dissolved. The initiator and monomer were then added to the reaction vial, the stir bar was placed at the top of the vial and held in place

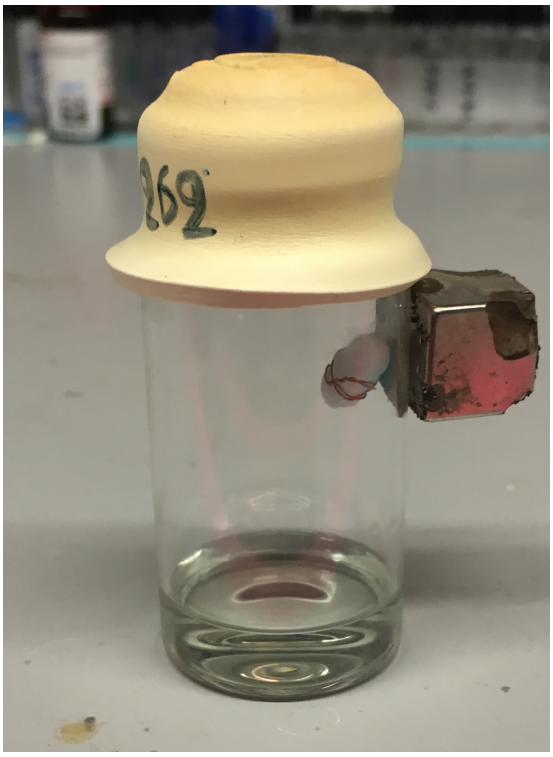

Figure 6.2: Photo of the reaction setup showing the stirbar with copper wire wrapped around it. The stir bar is magnetized to the side of the reaction vessel during the degassing step.

with a magnet, and everything was sealed with a suba-seal septum and degassed by purging the solution with N_2 (Figure 6.2).

Subsequently, the stir bar was allowed to drop to the bottom of the vial and the reaction commenced with stirring. Small aliquots were taken periodically for the kinetic experiments under an inert N_2 atmosphere, taking care not to introduce oxygen into the system. At reaction completion as indicated by NMR, the vial was opened to air. For chain extension reactions, after the first block reached very high conversion (typically >98 %), a degassed solution of monomer and solvent (1:1 v/v) were added *in situ* via syringe without the need to purify the macroinitiator. For example, for chain extensions of the PtBA mentioned above, 1.2 mL of hexyl acrylate and 1.2 mL of solvent were added to yield PtBA-b-PHA.

6.3 Results and Discussion

Two inherent problems that plague all chain ends on star polymers are bimolecular and intramolecular reactions, where star-star coupling or termination events become inevitable at high monomer conversion where there is a high concentration of chain ends (relative to linear analogues). Not only does this lead to uncontrolled coupling and variable star architectures, it precludes chain extensions to form diblock star copolymers, which are interesting to the research community for their self-assembly behavior and potential applications as drug delivery agents. [137,138] Certain solvents and monomers seem more prone to loss of control and star-star coupling, in particular solvents such as DMSO and DMF, which are widely used for copper mediated RDRP. In addition, there is a dichotomy between the polar solvents needed to solubilize the catalyst/ligand for Cu(0)-RDRP and the types of star polymers that researchers are interested in, such as hydrophobic

stars, which necessitate the use of a nonpolar solvent like toluene. In this study, we surveyed the literature and screened a number of solvents commonly used for Cu(0)-RDRP. N,N-Dimethyl formamide (DMF), acetonitrile (MeCN), dimethyl sulfoxide (DMSO), toluene, mixtures of toluene/isopropanol, and trifluoroethanol (TFE) were assessed for their capability to produce well defined star polymers. Moreover, *in situ* chain extensions were conducted for each solvent. *Tert*-butyl acrylate was chosen as a model monomer as it provides a synthetic handle to both hydrophobic and hy-drophilic stars, if deprotected with trifluoroacetic acid to yield poly(acrylic acid) stars. [139] Polymerization conditions were chosen that flout usual measures to suppress star-star coupling: a high concentration of monomer (1:1 with the solvent), a low amount of deactivator (0.01 eq. of $CuBr_2$ per CH-Br), and reaction cessation at high conversion ($>$ 95 %). Such small amounts of copper have previously been reported to give rise to substantial star-star coupling. [140] While MeCN and DMF could efficiently solubilize the catalyst mixture and resulted in relatively low dispersities (Đ$\sim$ 1.1), evidence of star-star coupling at higher monomer conversions (>80 %) was observed (Figure 6.3 part a and b, respectively).

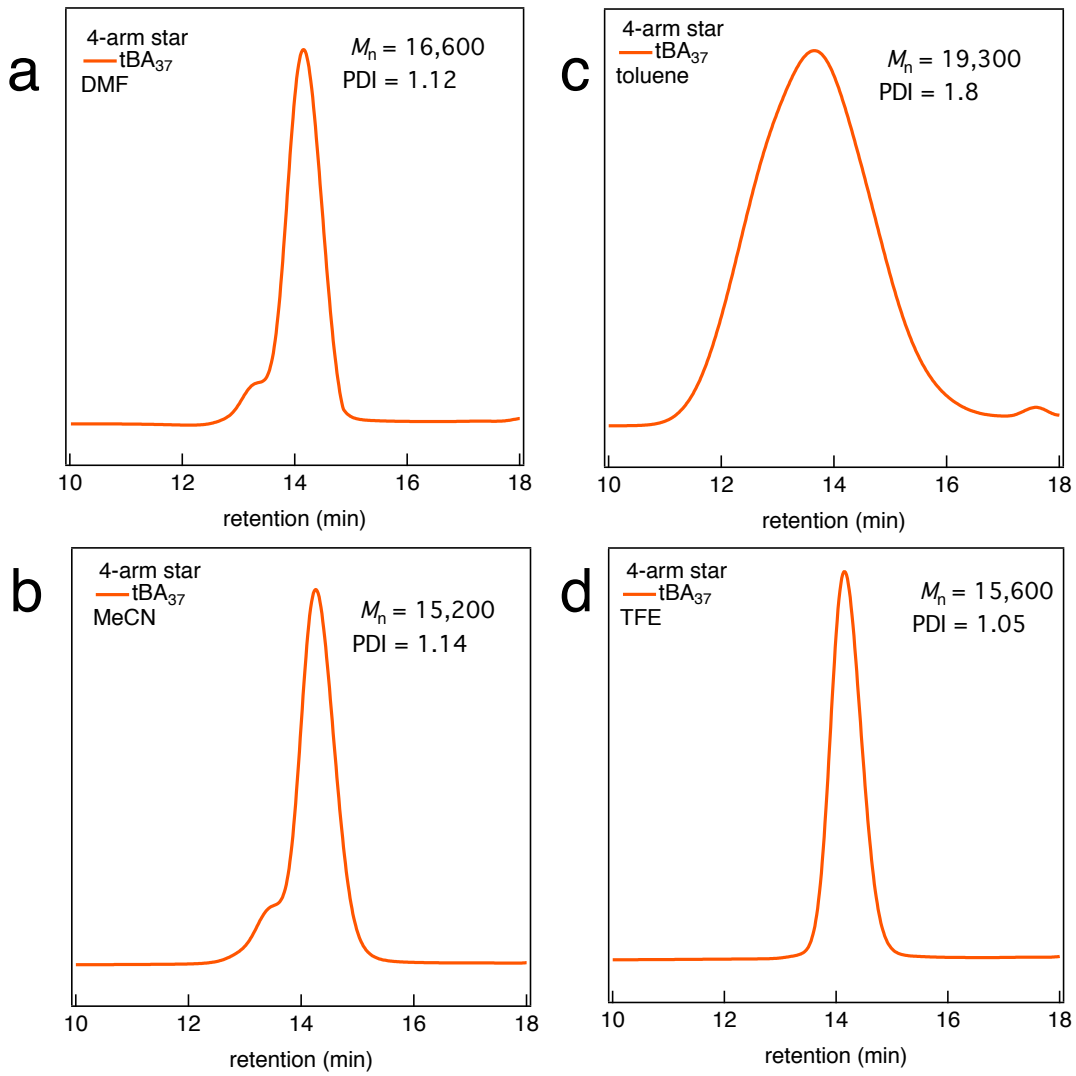

Figure 6.3: SEC traces (dRI $CHCl_3$) of 4-arm star PtBA homopolymers (solid orange line) synthesized via Cu(0) RDRP using (a) DMF, (b) MeCN, (c) toluene, (d) TFE. All reactions were run to high monomer conversion ($>$ 95 %).

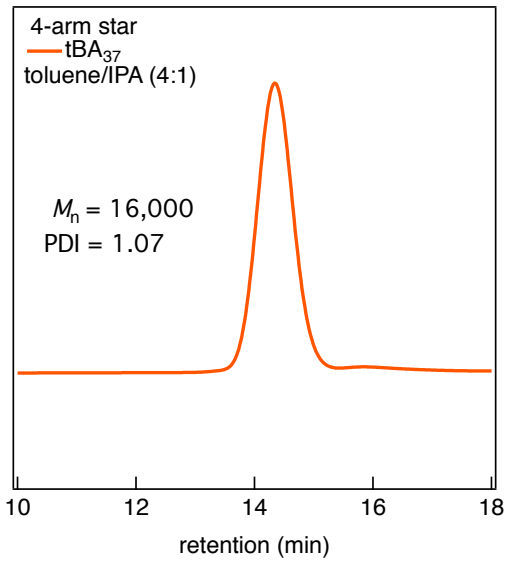

Figure 6.4: Reaction scheme and SEC traces (dRI $CHCl_3$) of 4-arm PtBA and PtBA-b-PHA stars in toluene/isopropanol (4:1).

In toluene, a complete loss of control was observed (Đ$\sim$ 1.8) (Figure 6.3 part c), which was attributed to the limited solubility of the catalyst complex used in this solvent. To circumvent this, a mixture of toluene with a small amount of isopropanol (4:1 toluene/IPA) resulted in minimal star-star coupling using this protocol (Figure 6.4), however chain extension of these stars did not give reproducible results.

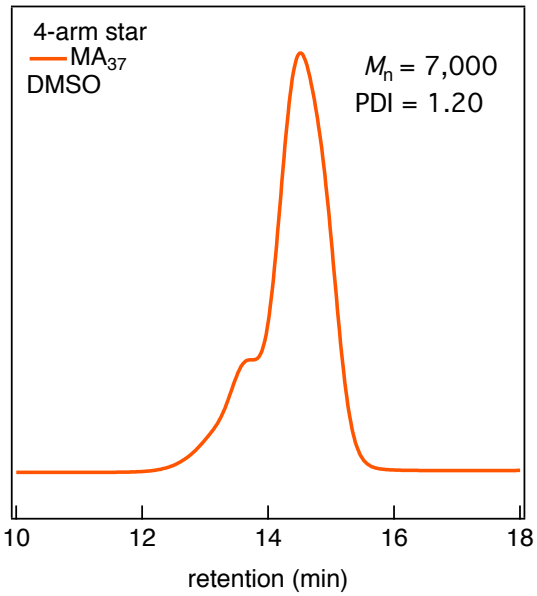

Figure 6.5: Reaction scheme and SEC traces (dRI $CHCl_3$) of 4-arm PMA stars in DMSO.

Similarly, when the polymerization was performed in DMSO (methyl acrylate was polymerized instead due to the limited solubility of PtBA in DMSO), the most widely used solvent for Cu(0)-wire polymerizations, [132, 141] substantial star-star coupling was detected (Figure 6.5).

This is in good agreement with previous reports showing substantial star-star coupling of stars consisting of MA in DMSO, whereas n-butyl acrylate could be polymerized in the absence of radical-radical coupling due to phase separation from the reaction medium upon polymerization. [127] Finding star-star coupling and loss of control to occur readily in these solvents, we turned our attention towards other solvents capable of solubilizing hydrophobic stars and the catalyst system. Inspired by reports from Percec and co-workers, as well as recent work in the Hawker group using semi-fluorinated solvents for the controlled synthesis of linear polyacrylates and polymethacrylates via Cu(0)-RDRP [79, 80, 81, 82, 83, 84, 85,86] and light ATRP [87,88] respectively, efforts were directed to trifluoroethanol (TFE). TFE is a commercially available solvent that is capable of solubilizing a vast array of monomers with different functionalities, including both hydrophobic and fluorinated side chains. In order to access these functionalities, TFE was used in the following study. Upon sonication for ∼15 min, $CuBr_2$ and Me_6TREN exhibit good solubility in TFE, evidenced by a solution color change to bright green. Polymerization of tBA was allowed to commence at room temperature, resulting in uniform stars with minimal star-star coupling and narrow molar mass distributions (Figure 6.3, part d).

A kinetic study was performed on tBA polymerization in TFE. Kinetic analysis revealed a linear increase of $\ln([M]_0/[M]_t)$ vs. time as well as linear evolution of M_n with monomer conversion (Figure 6.6), suggesting a controlled reaction and no star-star coupling evidenced by SEC even at high conversion (Figure 6.7).

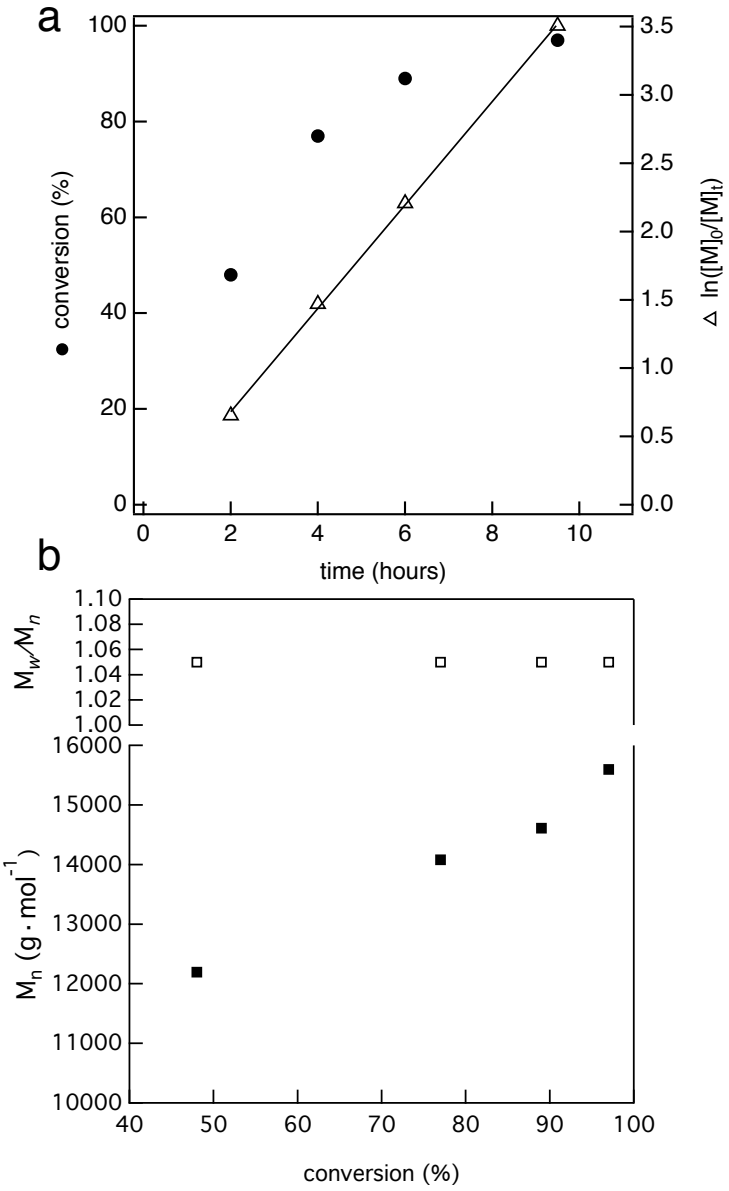

Figure 6.6: A single kinetic experiment for PtBA (DP_{target}, per arm =37) using the 4-arm star ATRP initiator exhibits a) linear kinetics and controlled growth through high conversion and b) molar mass evolution versus conversion shows livingness of the reaction.

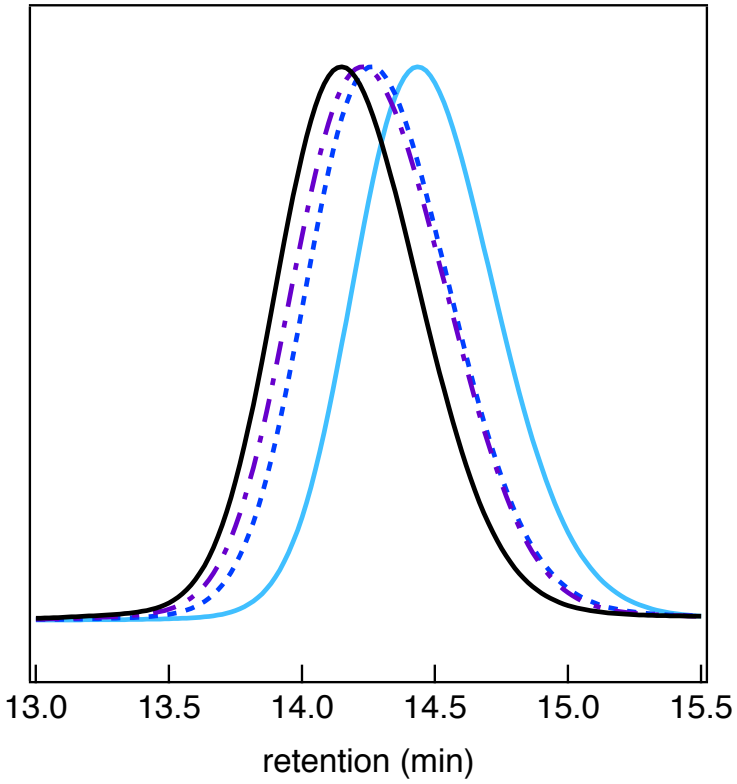

Figure 6.7: SEC traces (dRI $CHCl_3$) of 4-arm star PtBA (DPtarget, per arm=37) corresponding to each time point of kinetic experiment for 4-arm star PtBA (DP_{target}, per arm=37). SEC traces show no star-star coupling through high monomer conversions

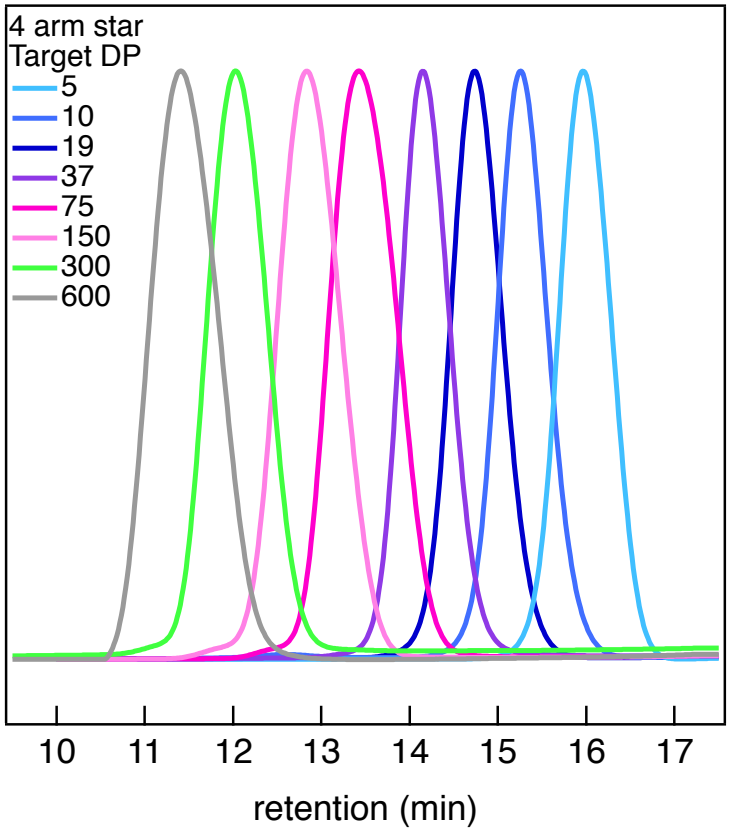

Figure 6.8: SEC traces (dRI $CHCl_3$) of 4-arm star PtBA polymers synthesized via Cu(0) RDRP in TFE. Target degrees of polymerization per arm are shown in legend (DP = 5-600 per arm). Narrow molar mass distributions and minimal star-star couplings are notable for these polymers.

While there is some deviation between experimental and theoretical M_n values, it should be noted that star polymers adopt significantly different hydrodynamic volumes relative to the linear PS standards used for SEC calibration. [142] Nevertheless, narrow molar mass distributions (Đ$\sim$ 1.1) were observed throughout the polymerization with minimal star-star coupling even at very high monomer conversions (>95 %).

			M_n (kg mol^{-1})		
Entry	**$DP_{per\ arm}$**	**conv (%)**	**theor**	**exp[b]**	**Đ[b]**
1	5	99	3.3	2.9	1.08
2	10	99	5.6	5.8	1.07
3	19	99	10.3	9.3	1.07
4	37	99	20	15.6	1.05
5	75	99	39.1	28.2	1.09
6	150	99	77.6	48	1.09
7	300	97	154	99	1.08
8	600	95	308	171	1.11
9	1200	93	616	225	1.18
10	2400	92	1213	318	1.21

Figure 6.9: Table of ^{1}H NMR and SEC analysis of 4-arm PtBA stars. In all polymerizations, 5 cm of Cu(0)-wire, 5 % $CuBr_2$, and 72 % Me_6TREN with respect to initiator (mol %) were utilized. The volume ratio of monomer to TFE was maintained at 1:1. Conversion was calculated via ^{1}H NMR. ^{b}Determined by SEC relative to PS standards.

In order to probe the potential of this technique to maintain control for both very low and very high molar masses, a series of polymers were synthesized targeting degrees of polymerization (DP) from 5 to 2400 per arm using the 4-arm initiator.

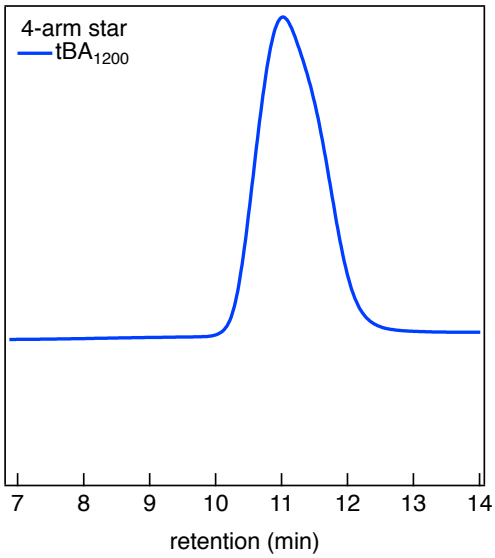

Figure 6.10: SEC traces (dRI $CHCl_3$) of 4-arm polymer PtBA stars (DP_{perarm} = 1200).

A low molar mass 4-arm PtBA star (DP_{perarm} = 5, Figure 6.9, entry 1) gave rise to a narrow molar mass distribution (Đ= 1.08). Upon targeting a range of star polymers with dif-ferent molar masses (DP_{perarm} = 10-600, Figure 6.9, entries 2-8), narrow molar mass distributions were also achieved (Đ∼ 1.1) with very minimal star-star coupling (Figure 6.8), even at quantitative or near-quantitative monomer conversions (>95 %). For instance, targeting DP_{perarm} = 600 yielded a well-defined star polymer with M_n = 171,000 g·mol^{-1} with a Đ= 1.11 at a conversion of 95 %. Pushing the system further to target DPper arm = 1200 and DP_{perarm} = 2400 (Figure 6.9, entries 9-10) gave rise to broadened distributions, suggesting that the limits of the technique had been reached (Figure 6.10 and 6.11, respectively). Nevertheless, molar masses up to 320,000 g ·mol^{-1} (relative to linear polystyrene standards) could be targeted with a final Đ= 1.21 at very high conversions (>90 %) (Figure 6.11).

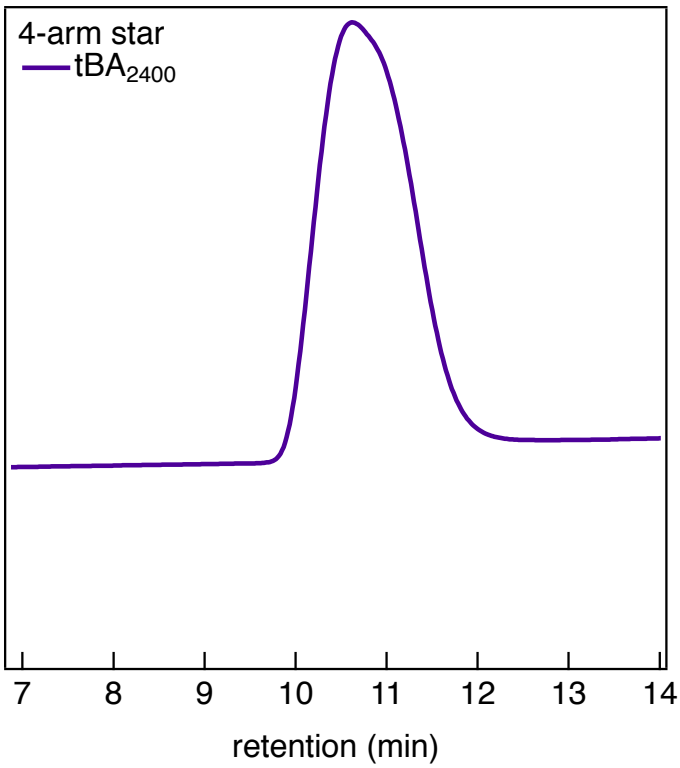

Figure 6.11: SEC traces (dRI $CHCl_3$) of 4-arm polymer PtBA stars (DP_{perarm} = 2400).

The scope of the technique using the 4-arm initiator was then extended to a library of acrylic monomers including n-butyl acrylate (nBA), methyl acrylate (MA), hexyl acrylate (HA) and trifluoroethyl acrylate (TFEA).

All polymerizations (DP_{perarm} = 37) reached very high monomer conversions (>95 %) within 8 h while exhibiting narrow molar mass distributions (Đ$\sim$ 1.1) and minimal star-star coupling (Figure 6.12 and Figure 6.13).

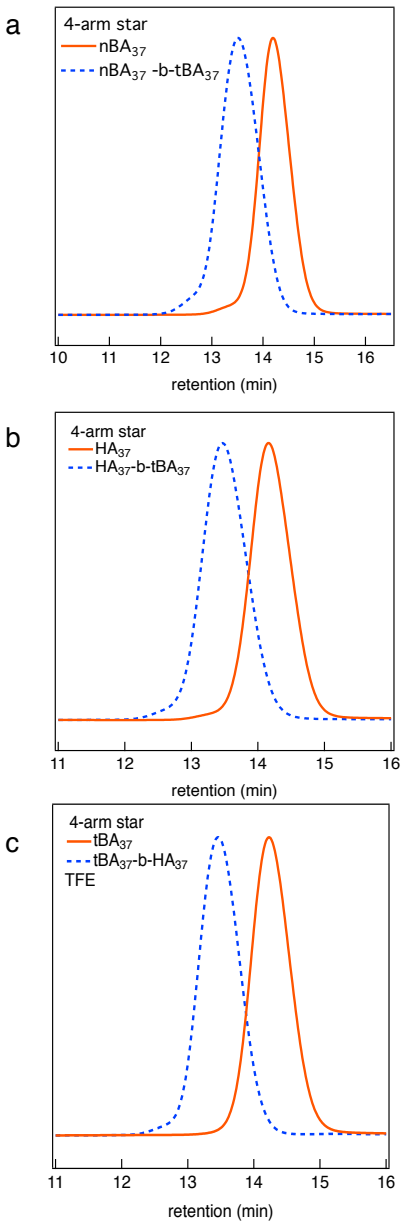

Figure 6.12: SEC traces of 4-arm homopolymer precursors (solid orange lines) of (a) PnBA, (b) PHA, and (c) PtBA and the corresponding star block polymers following chain extension with PtBA or PHA (dashed blue lines).

				M_n (kg mol^{-1})		
	Entry	**$DP_{per\ arm}$**	**conv (%)**	**theor**	**exp[b]**	**Đ[b]**
1		*t*BA	99	20.0	14.5	1.06
2		TFEA	97	23.8	10.8	1.09
3		nBA	99	19.9	15.1	1.07
4		HA	99	24.1	15.4	1.07

Figure 6.13: Table of ^{1}H NMR and SEC analysis of various acrylates polymerized using the 4-arm initiator. In all polymerizations, 5 cm of Cu(0)-wire, 5 % $CuBr_2$, and 72 % Me_6TREN with respect to initiator (mol %) were utilized. The volume ratio of monomer to TFE was maintained at 1:1. Conversion was calculated via ^{1}H NMR. ^{b}Determined by SEC relative to PS standards.

These monomers showed slightly more star-star coupling at very high conversions (>99 %) than the negligible coupling of PtBA stars. Compared to current literature reports, this coupling of other monomers tested is incredibly minor. In order to determine chain-end fidelity of the PtBA stars, *in situ* diblock copolymers were synthesized (Figure 6.12). Upon completion of the polymerization of PtBA (∼99 % conversion), an equimolar aliquot of hexyl acrylate to the tBA monomer feed ratio was injected into the polymerization mixture. Without the need to purify the macroinitiator, a well-defined star diblock PtBA-PHA was obtained in a one-pot synthesis (M_n = 28,600 g·mol^{-1}, Đ∼ 1.1). Limited star-star coupling was observed, thus highlighting the ability of TFE to suppress undesired coupling while maintaining good chain-end fidelity. In addition to PtBa-b-PHA, two other diblocks were synthesized: PnBA-b-PtBA and PHA-b-PtBA. The success of these reactions, including re-initiation of the macroinitiators in a one-pot synthesis (Đ 1.1), indicates the relative monomer and sequence tolerance of this chemistry (Figure 6.12). Similar attempts to do chain extensions of HA from PtBA in other solvents (e.g. DMF and MeCN) resulted in inefficient re-initiation of the macroinitiator and/or severe star-star coupling (Figure 6.14 and 6.14). In DMF, the first block of tBA reached 99% conversion, with M_n = 16,700 g·mol^{-1} and Đ∼ 1.12. The chain extension with HA to 93% conversion resulted in M_n = 19,100 g·mol^{-1} and Đ∼ 1.19, with visible star-star coupling. In MeCN, the first block of tBA similarly reached 99% conversion with M_n = 15,000 g·mol^{-1} and Đ∼ 1.14. The chain extension of HA in MeCN at 90% conversion showed a M_n = 27,400 g·mol^{-1} and Đ∼ 1.14, also with visible star-star coupling.

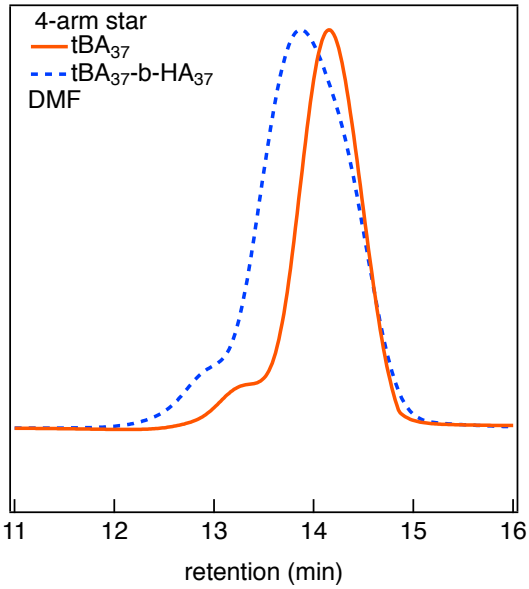

Figure 6.14: SEC traces (dRI $CHCl_3$) of 4-arm PtBA and PtBA-b-PHA stars in DMF

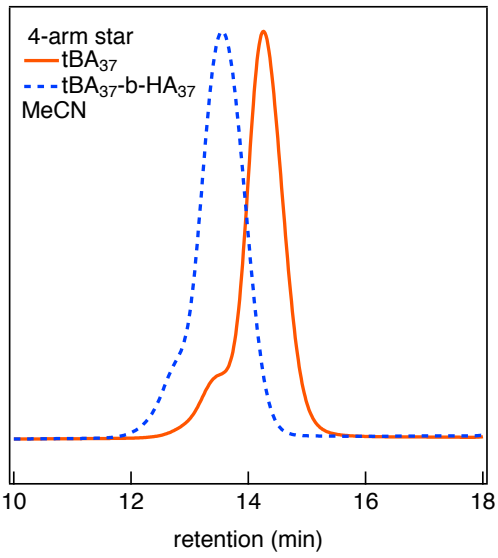

Figure 6.15: SEC traces (dRI $CHCl_3$) of 4-arm PtBA and PtBA-b-PHA stars in MeCN

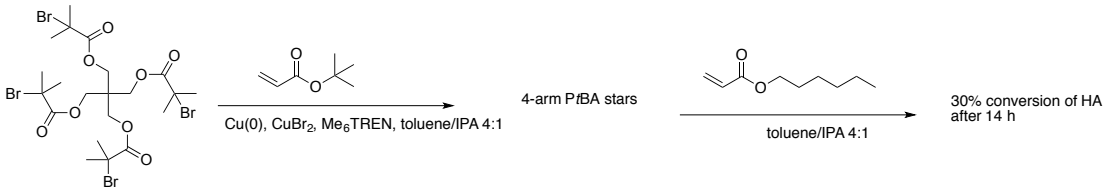

Figure 6.16: Reaction scheme of 4-arm PtBA-b-PHA stars ($DP_{perarm} = 37$ for each block) in toluene/IPA

Re-initiation to grow a second block using HA in the toluene/IPA mixture did not work well, with low monomer conversion even after 14 h (Figure 6.16, 6.17).

Repetitions of this polymerization led to mixed results, sometimes showing better control but to lower conversions (less than 90%), therefore showing a less robust chemistry than the TFE solvent. When TFE was used as a solvent for light-mediated ATRP (no copper wire), significant star-star coupling was observed at high monomer conversion. This suggests that it is the combination of TFE and heterogeneous catalysis using Cu(0)-wire that facilitates the synthesis of well-defined stars that can undergo chain extension and exhibit marginal star-star coupling.

Entry	Block	Rxn time	$DP_{per\ arm}$	Conversion (%)	$M_{n,\ theor.}$ [g/mol]	$M_{n,\ exp.}$ [g/mol]	Đ
1	*t*BA	8 h	37	91	20,000	16,000	1.07
2	*t*BA-b-HA	30 h	37	30	43,400	21,000	1.06
3	*t*BA-b-HA	39 h	37	39	43,400	21,000	1.08

Figure 6.17: Table of GPC and NMR data for 4-arm PtBA and 4-arm PtBA-b-PHA stars ($DP_{perarm} = 37$ for each block) in toluene/IPA

After establishing optimal conditions for the synthesis of several monomers and for a range of molar masses, a further challenge to this system included evaluating the compatibility of this chemistry using initiators with a greater number of initiating sites or "arms." One would expect that a higher number of arms would increase the local concentration of radicals within a certain volume, exacerbating any star-star coupling events. For this purpose, an octa-arm initiator was synthesized from lactose following a well-established literature protocol. [134] Kinetic investigation of the polymerization of tBA with a target DP = 37 per arm revealed a short inhibition period (∼40 min), likely due to initial insolubility of the initiator in TFE, followed by fast polymerization rates with full monomer conversion achieved within 4 h (Figure 6.18). SEC traces show perfectly unimodal distributions throughout the polymerization without any visible star-star coupling, while the molar mass distributions remained at Đ= 1.1 for the entire reaction. Upon reaching very high conversions for PtBA (∼ 98 %), hexyl acrylate was added to the polymerization mixture *in situ* yielding a well-defined PtBA-b-PHA diblock copolymer with a final Đ= 1.1 (Figure 6.19).

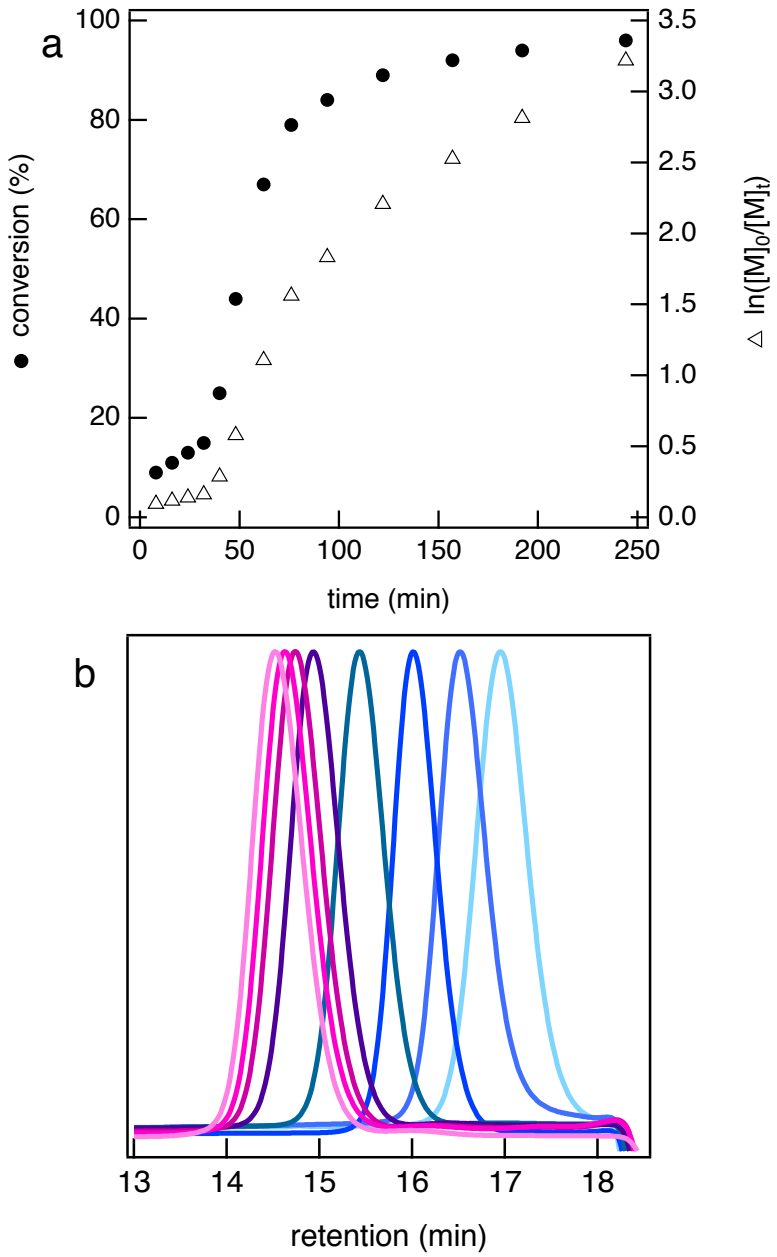

Figure 6.18: (a) Conversion (closed circle) and kinetic plot (open triangle) for the polymerization of tBA using the 8-arm initiator. (b) Corresponding SEC chromatograms of produced star polymers isolated at various times.

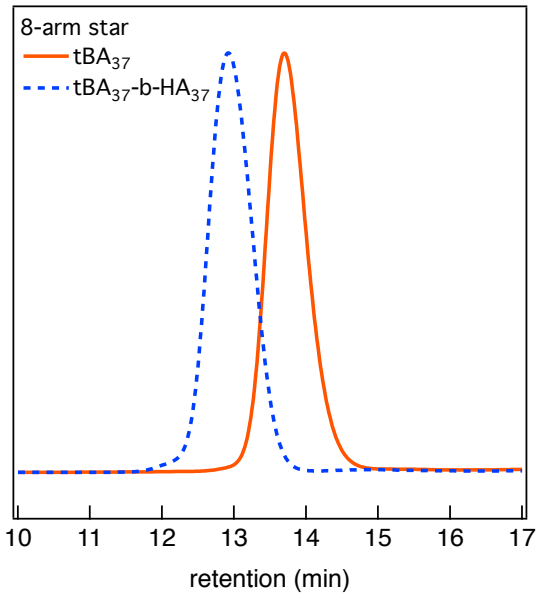

Figure 6.19: SEC traces (dRI $CHCl_3$) of the 8-arm diblock polymers showing PtBA homopolymer precursors (solid orange line) and PtBA-b-PHA diblock copolymers (dashed blue line).

			M_n (kg mol^{-1})		
Entry	**$DP_{per\ arm}$**	**conv (%)**	**theor**	**exp[b]**	**Đ[b]**
1	18	95	18.2	12.5	1.05
2	37	95	35.7	22.7	1.06
3	75	94	72.1	37.7	1.05
4	150	94	144	77	1.06
5	300	91	280	119	1.07

Figure 6.20: Table of $_1$H NMR and SEC analysis of 8-arm PtBA stars. In all polymerizations, 5 cm of Cu(0)-wire, 5 % $CuBr_2$, and 72 % Me_6TREN with respect to initiator (mol %) were utilized. The volume ratio of monomer to TFE was maintained at 1:1. Conversion was calculated via ^{1}H NMR. ^{b}Determined by SEC relative to PS standards.

No star-star coupling was observed for the 8-arm PtBA-b-PHA diblock copolymer, demonstrating the capacity of the Cu(0)/$CuBr_2$/TFE system to prevent this side reaction even with more arms. Additional higher molar mass 8-arm star polymers were prepared from tBA, resulting in well-defined stars (6.20).

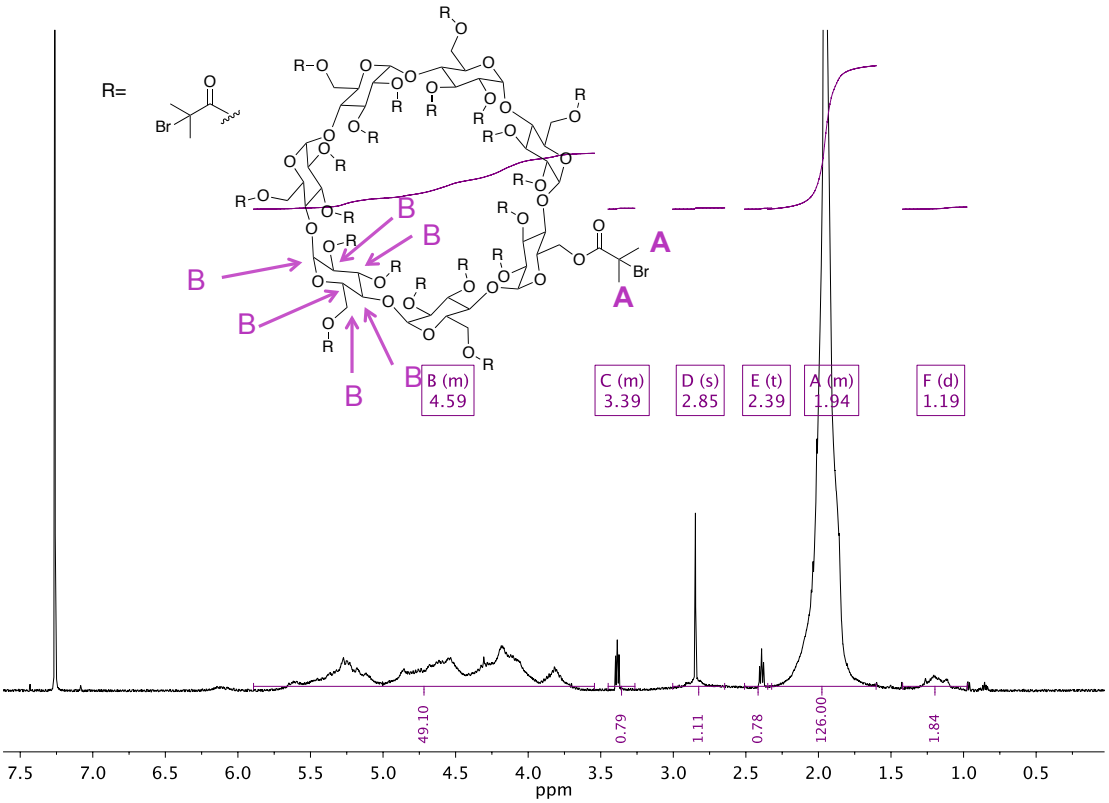

Figure 6.21: ^{1}H NMR of the cyclodextrin initiator. 18 methyl protons per sugar unit x 7 = 126H at 1.1ppm, 7 acetal protons per sugar unit x 7 = 49H from 3.6-5.5ppm.

To expand the scope beyond tetra- and octa- arm stars, a cyclodextrin based initiator (CD), with up to 21 arms, was targeted through a literature protocol. [135] According to ^{1}H NMR, the synthesis of the CD-initiator reached completion as evidenced by the integration of methylene protons between 5.89-3.54 ppm equal to 49 relative to the 126 methylene protons found at 2.35-1.60 ppm, in agreement with previous reports of the compound (Figure 6.21).

IR spectroscopy was also used to analyze consumption of the hydroxyl groups, showing a disappearance of the broad peak at 3320 cm^{-1} (Figure 6.22). ESI-MS, on the other hand, confirmed functionalization of the cyclodextrin through 19 bromines, averaging 17 ATRP functionalities per cyclodextrin molecule (Figure 6.23).

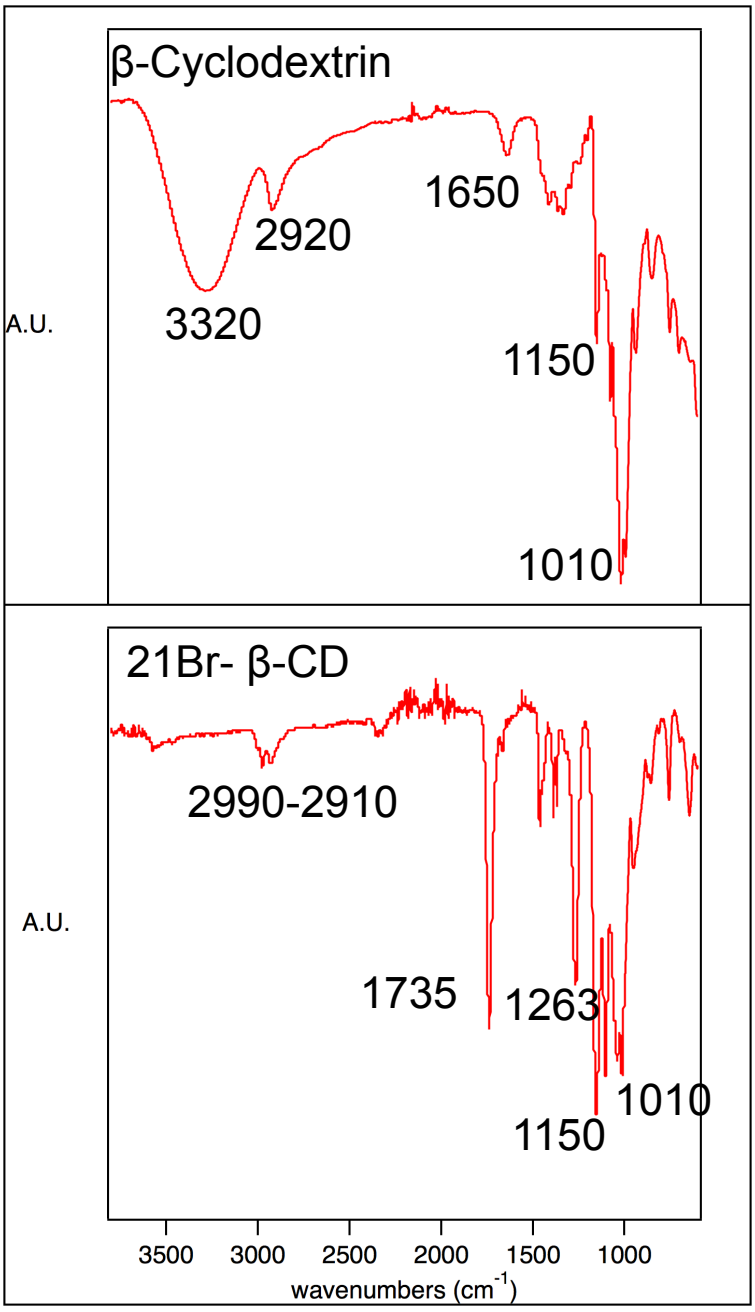

Figure 6.22: IR spectra comparing cyclodextrin starting material (top) to the effectively 17-arm CD-initiator (bottom).

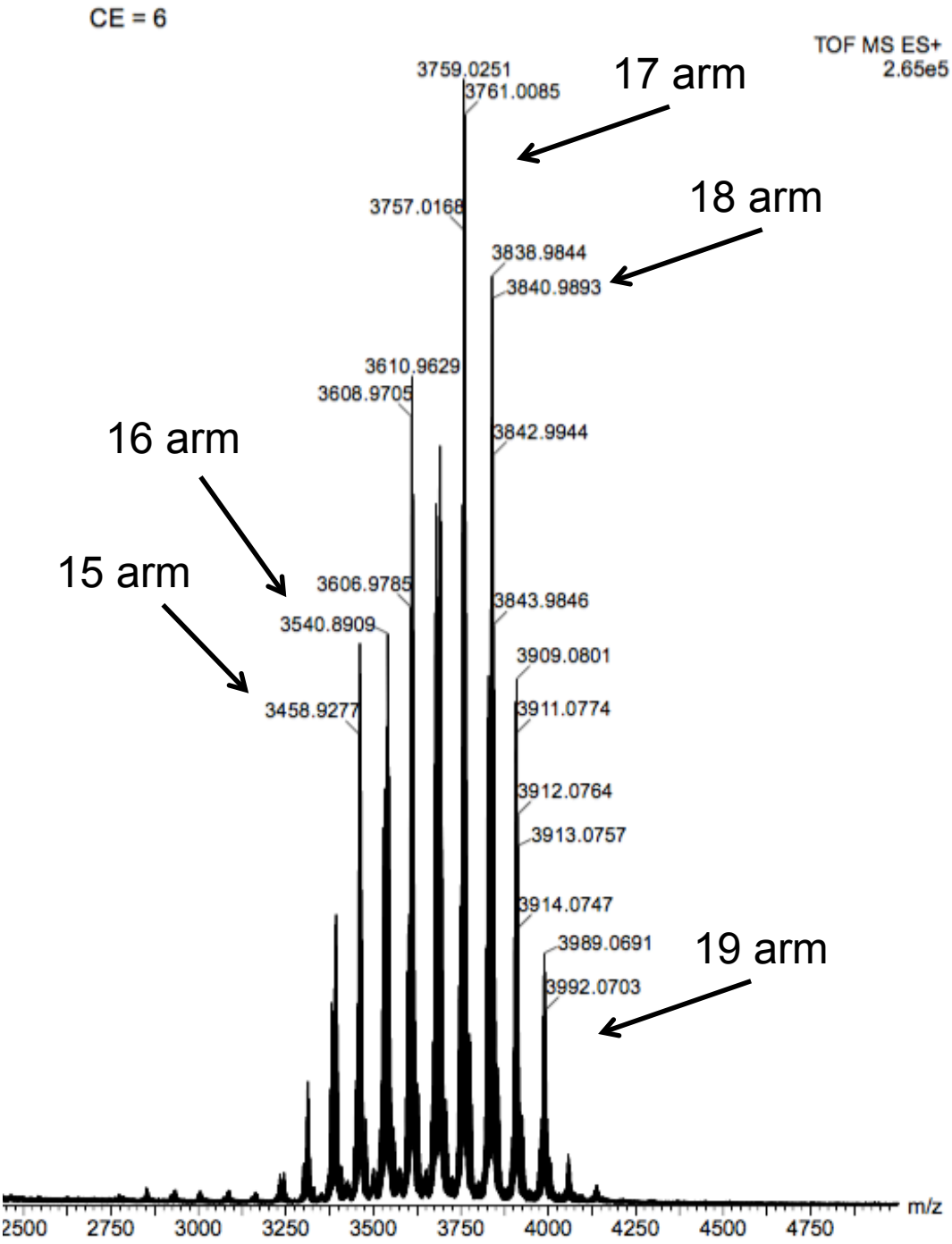

Figure 6.23: ESI of the multi-arm initiator (up to 19 arms and an average of 17 arm) showing a range of arms functionalized.

Mass (arms)	Ions	Peak
3364 (15 arm)	$2H + 4Na^{+}$	3458
3514 (16 arm)	$3H + 1Na^{+}$	3540
3664 (17 arm)	$4H + 4Na^{+}$	3759
3814 (18 arm)	$3H + 1Na^{+}$	3840
3964 (19 arm)	$2H + 1Na^{+}$	3989
4264 (21 arm)	--	--

Figure 6.24: Analysis of the ESI spectrum with counter ions for ESI-MS

			M_n (kg mol^{-1})		
Entry	**$DP_{per\ arm}$**	**conv (%)**	**theor**	**exp[b]**	**Đ[b]**
1	7	96	23.2	8.3	1.13
2	32	94	90	21.3	1.19
3	52	90	132	31.3	1.26
4	79	92	196	63.5	1.10

Figure 6.25: Table of ^{1}H NMR and SEC analysis of CD PtBA stars. In all polymerizations, 5 cm of Cu(0)-wire, 5 % $CuBr_2$, and 72 % Me_6TREN with respect to initiator (mol %) were utilized. The volume ratio of monomer to TFE was maintained at 1:1. Conversion was calculated via ^{1}H NMR. ^{b}Determined by SEC relative to PS standards.

Given that the number of arms was at least double the octa-functional initiator, reactions proceeded in TFE using tBA. Low molar mass tailing of the SEC trace of the CD-stars for the tBA homopolymer is in accordance with the literature. [136] When the polymerization of tBA reached high conversion (96 %), trifluoroethyl acrylate was subsequently added *in situ*, efficiently yielding a PtBA-b-PTFEA diblock copolymer (Figure 6.26, M_n = 22,800, Đ= 1.04). Higher molar masses were targeted for these multi-arm PtBA stars, which showed low dispersities (Figure 6.27, 6.24 and Figure 6.25). No star-star coupling was observed for these multi-arm polymers, further highlighting this technique as a way to obtain semi-fluorinated star polymers of low viscosity but high molar mass, which may find use in a wide range of applications (e.g. MRI agents).

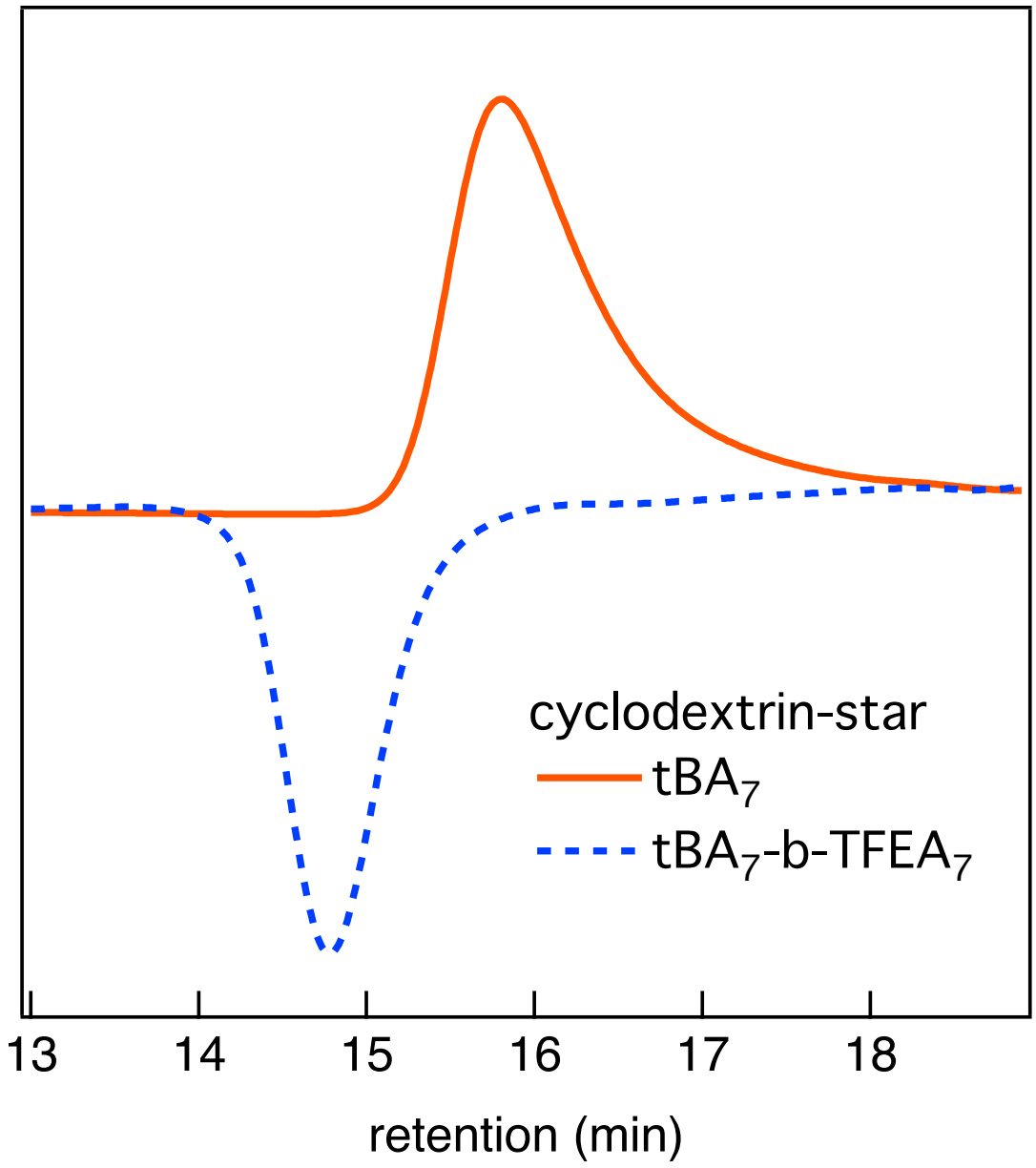

Figure 6.26: SEC traces (dRI $CHCl_3$) of the cyclodextrin-star (CD-star) diblock polymers showing PtBA homopolymer precursors (solid orange line) and PtBA-b-PTFEA diblock copolymers (dashed blue line).

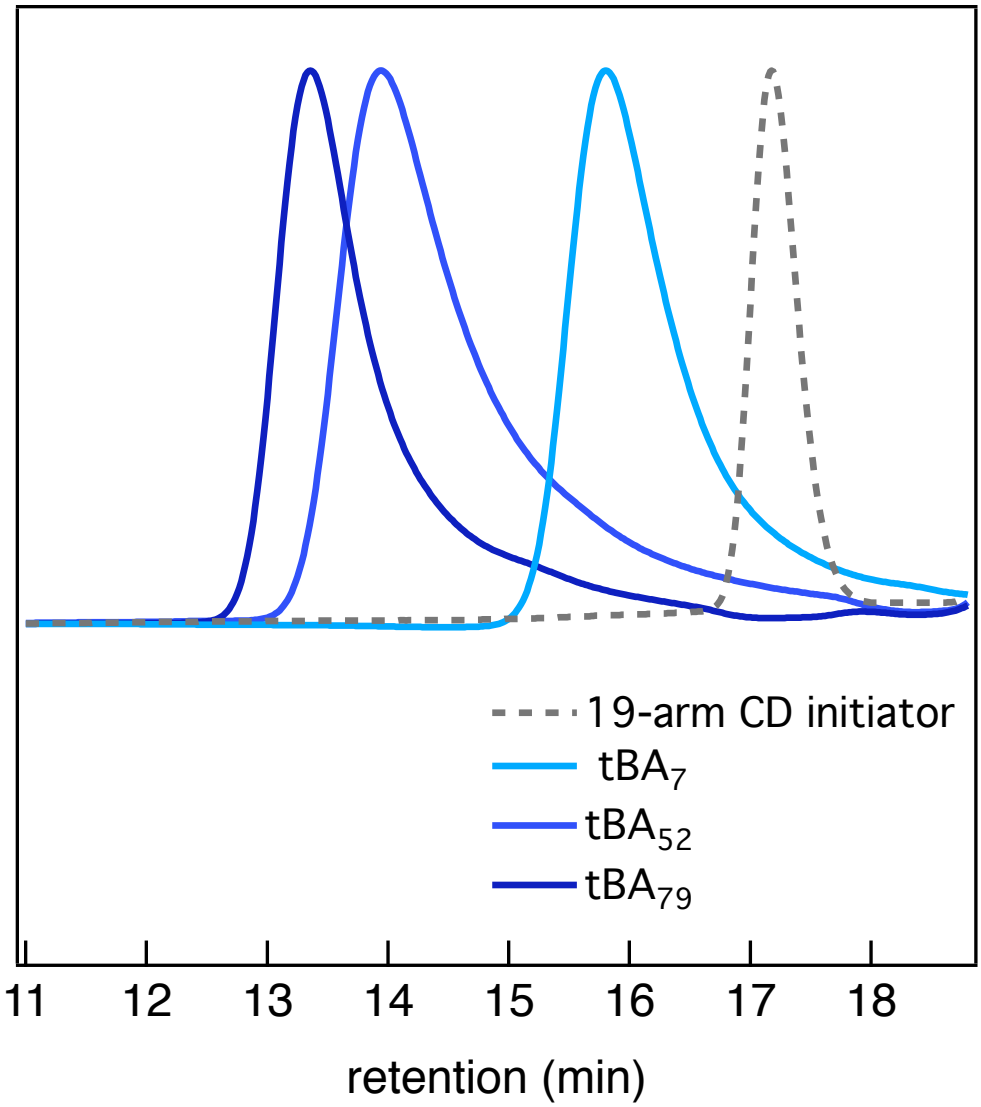

Figure 6.27: SEC traces (dRI $CHCl_3$) of PtBA stars polymerized from CD- initiator (max. 19 arms) in TFE (DP_{perarm} shown in legend). ^{1}H NMR conversion and GPC values found in Figure 6.25.

6.4 Conclusion

In conclusion, we developed the combination of Cu(0)-wire RDRP and TFE to synthesize well-defined stars for a range of hydrophobic and semi-fluorinated acrylic monomers. Different molar masses (DP_{perarm} = 5-2400) of star polymers, including multi-arm diblock stars, could be obtained while exhibiting low molar mass distributions and high end-group fidelity, even through high monomer conversions. This level of control permits the *in situ* generation of diblock star copolymers with minimal side reactions, thus allowing facile access to the synthesis of well-defined star materials for a variety of applications.

Bibliography

[1] K. Matyjaszewski and J. Spanswick, *Controlled/living radical polymerization*, *Materials Today* **8** (2005), no. 3 26 – 33.

[2] K. Matyjaszewski, *Controlled Radical Polymerization: State-of-the-Art in 2014*, ch. 1, pp. 1–17.

[3] K. Matyjaszewski, *Atom transfer radical polymerization (atrp): Current status and future perspectives*, *Macromolecules* **45** (2012), no. 10 4015–4039.

[4] G. Moad, E. Rizzardo, and S. H. Thang, *Radical additionfragmentation chemistry in polymer synthesis*, *Polymer* **49** (2008), no. 5 1079 – 1131.

[5] C. J. Hawker, A. W. Bosman, and E. Harth, *New polymer synthesis by nitroxide mediated living radical polymerizations*, *Chemical Reviews* **101** (2001), no. 12 3661–3688.

[6] B. P. Fors and C. J. Hawker, *Control of a Living Radical Polymerization of Methacrylates by Light*, *Angewandte Chemie International Edition* **51** (2012), no. 35 8850–8853.

[7] M. Chen, M. Zhong, and J. A. Johnson, *Light-controlled radical polymerization: Mechanisms, methods, and applications*, *Chemical Reviews* **116** (2016), no. 17 10167–10211.

[8] A. J. D. Magenau, Y. Kwak, and K. Matyjaszewski, *Atrp of methacrylates utilizing cuiix2/l and copper wire*, *Macromolecules* **43** (2010), no. 23 9682–9689.

[9] A. Anastasaki, V. Nikolaou, Q. Zhang, J. Burns, S. R. Samanta, C. Waldron, A. J. Haddleton, R. McHale, D. Fox, V. Percec, P. Wilson, and D. M. Haddleton, *Copper(II)/Tertiary Amine Synergy in Photoinduced Living Radical Polymerization: Accelerated Synthesis of*

ω-Functional and α,ω-Heterofunctional Poly(acrylates), *Journal of the American Chemical Society* **136** (2014), no. 3 1141–1149.

[10] B. Oschmann, J. Lawrence, M. W. Schulze, J. M. Ren, A. Anastasaki, Y. Luo, M. D. Nothling, C. W. Pester, K. T. Delaney, L. A. Connal, A. J. McGrath, P. G. Clark, C. M. Bates, and C. J. Hawker, *Effects of tailored dispersity on the self-assembly of dimethylsiloxanemethyl methacrylate block co-oligomers*, *ACS Macro Letters* **6** (2017), no. 7 668–673.

[11] W. J. Chung, J. J. Griebel, E. T. Kim, H. Yoon, A. G. Simmonds, H. J. Ji, P. T. Dirlam, R. S. Glass, J. J. Wie, N. A. Nguyen, B. W. Guralnick, J. Park, A. Somogyi, P. Theato, M. E. Mackay, Y.-E. Sung, K. Char, and J. Pyun, *The use of elemental sulfur as an alternative feedstock for polymeric materials.*, *Nature chemistry* **5** (2013), no. 6 518–524.

[12] C. Liu, K. Kubo, E. Wang, K.-S. Han, F. Yang, G. Chen, F. A. Escobedo, G. W. Coates, and P. Chen, *Single polymer growth dynamics*, *Science* **358** (2017), no. 6361 352–355.

[13] S. Lee, M. J. Bluemle, and F. S. Bates, *Discovery of a Frank-Kasper sigma phase in sphere-forming block copolymer melts.*, *Science (New York, N.Y.)* **330** (2010), no. 6002 349–353.

[14] M. D. Dimitriou, Z. Zhou, H.-S. Yoo, K. L. Killops, J. A. Finlay, G. Cone, H. S. Sundaram, N. A. Lynd, K. P. Barteau, L. M. Campos, D. A. Fischer, M. E. Callow, J. A. Callow, C. K. Ober, C. J. Hawker, and E. J. Kramer, *A general approach to controlling the surface composition of poly(ethylene oxide)-based block copolymers for antifouling coatings*, *Langmuir* **27** (2011), no. 22 13762–13772.

[15] Y.-H. La, E. W. Edwards, S.-M. Park, and P. F. Nealey, *Directed assembly of cylinder-forming block copolymer films and thermochemically induced cylinder to sphere transition: a hierarchical route to linear arrays of nanodots*, *Nano Letters* **5** (2005), no. 7 1379–1384.

[16] J. Rivnay, S. C. B. Mannsfeld, C. E. Miller, A. Salleo, and M. F. Toney, *Quantitative determination of organic semiconductor microstructure from the molecular to device scale.*, *Chemical reviews* **112** (2012), no. 10 5488–5519.

[17] L. Dong, W. Li, and W.-S. Li, *Construction of a long range p/n heterojunction with a pair of nanometre-wide continuous d/a phases*, *Nanoscale* **3** (2011) 3447–3461.

[18] S. Dadashi Silab, M. Atilla Tasdelen, and Y. Yagci, *Photoinitiated atom transfer radical polymerization: Current status and future perspectives*, *Journal of Polymer Science Part A: Polymer Chemistry* **52** (2014), no. 20 2878–2888.

[19] F. A. Leibfarth, K. M. Mattson, B. P. Fors, H. A. Collins, and C. J. Hawker, *External regulation of controlled polymerizations.*, *Angewandte Chemie (Int. ed.)* **52** (2013), no. 1 199–210.

[20] A. J. D. Magenau, N. C. Strandwitz, A. Gennaro, and K. Matyjaszewski, *Electrochemically mediated atom transfer radical polymerization*, *Science* **332** (2011), no. 6025 81–84.

[21] A. G. Tennyson, K. M. Wiggins, and C. W. Bielawski, *Mechanical activation of catalysts for cc bond forming and anionic polymerization reactions from a single macromolecular reagent*, *Journal of the American Chemical Society* **132** (2010), no. 46 16631–16636.

[22] J. Zhang, A. Li, H. Liu, D. Yang, and J. Liu, *Well-controlled raft polymerization initiated by recyclable surface-modified nb(oh)5 nanoparticles under visible light irradiation*, *Journal of Polymer Science Part A: Polymer Chemistry* **52** (2014), no. 19 2715–2724.

[23] M. Tanabe and I. Manners, *Photolytic living anionic ring-opening polymerization (ROP) of silicon-bridged [1] ferrocenophanes via an iron-cyclopentadienyl bond cleavage mechanism*, *Journal of the American Chemical Society* **126** (2004), no. 37 11434–11435.

[24] Q. Liu, L. Liu, Y. Ma, C. Zhao, and W. Yang, *Visible light-induced controlled radical polymerization of methacrylates with perfluoroalkyl iodide as the initiator in conjugation with a photoredox catalyst fac-[ir(ppy)]3*, *Journal of Polymer Science Part A: Polymer Chemistry* **52** (2014), no. 22 3283–3291.

[25] M. Tanabe, G. Vandermeulen, and W. Y. Chan, *Photocontrolled living polymerizations*, *Nature Materials* (2006), no. 5 467–470.

[26] S. Dadashi-Silab, A. M. Asiri, S. B. Khan, K. A. Alamry, and Y. Yagci, *Semiconductor nanoparticles for photoinitiation of free radical polymerization in aqueous and organic media*, *Journal of Polymer Science Part A: Polymer Chemistry* **52** (2014), no. 10 1500–1507.

[27] N. J. Treat, H. Sprafke, J. W. Kramer, P. G. Clark, B. E. Barton, J. Read de Alaniz, B. P. Fors, and C. J. Hawker, *Metal-Free Atom Transfer Radical Polymerization*, *Journal of the American Chemical Society* **136** (Nov., 2014) 16096–16101.

[28] N. J. Treat, B. P. Fors, J. W. Kramer, M. Christianson, C.-Y. Chiu, J. Read de Alaniz, and C. J. Hawker, *Controlled radical polymerization of acrylates regulated by visible light*, *ACS Macro Letters* **3** (2014), no. 6 580–584.

[29] M. Neumann and K. Zeitler, *Application of microflow conditions to visible light photoredox catalysis.*, *Organic letters* **14** (2012), no. 11 2658–2661.

[30] F. R. Bou-Hamdan and P. H. Seeberger, *Visible-light-mediated photochemistry: accelerating ru(bpy)32+-catalyzed reactions in continuous flow*, *Chem. Sci.* **3** (2012) 1612–1616.

[31] J. W. Tucker, Y. Zhang, T. F. Jamison, and C. R. J. Stephenson, *Visible-light photoredox catalysis in flow*, *Angewandte Chemie International Edition* **51** (2012), no. 17 4144–4147.

[32] C. Tonhauser, A. Natalello, H. Lwe, and H. Frey, *Microflow technology in polymer synthesis*, *Macromolecules* **45** (2012), no. 24 9551–9570.

[33] A. Natalello, J. Morsbach, A. Friedel, A. Alkan, C. Tonhauser, A. H. E. Mller, and H. Frey, *Living anionic polymerization in continuous flow: Facilitated synthesis of high-molecular weight poly(2-vinylpyridine) and polystyrene*, *Organic Process Research & Development* **18** (2014), no. 11 1408–1412.

[34] B. Wenn, M. Conradi, A. D. Carreiras, D. M. Haddleton, and T. Junkers, *Photo-induced copper-mediated polymerization of methyl acrylate in continuous flow reactors*, *Polym. Chem.* **5** (2014) 3053–3060.

[35] T. Aillet, K. Loubiere, O. Dechy-Cabaret, and L. Prat, *Photochemical synthesis of a cage compound in a microreactor: Rigorous comparison with a batch photoreactor*, *Chemical Engineering and Processing: Process Intensification* **64** (2013), no. Supplement C 38 – 47.

[36] D. Wilms, J. Klos, and H. Frey, *Microstructured reactors for polymer synthesis: A renaissance of continuous flow processes for tailor-made macromolecules?*, *Macromolecular Chemistry and Physics* **209** (2008), no. 4 343–356.

[37] A. Nagaki, K. Kawamura, S. Suga, T. Ando, M. Sawamoto, and J.-i. Yoshida, *Cation pool-initiated controlled/living polymerization using microsystems*, *Journal of the American Chemical Society* **126** (2004), no. 45 14702–14703.

[38] J. A. Burns, C. Houben, A. Anastasaki, C. Waldron, A. A. Lapkin, and D. M. Haddleton, *Poly(acrylates) via set-lrp in a continuous tubular reactor*, *Polym. Chem.* **4** (2013) 4809–4813.

[39] T. Noda, A. J. Grice, M. E. Levere, and D. M. Haddleton, *Continuous process for atrp: Synthesis of homo and block copolymers*, *European Polymer Journal* **43** (2007), no. 6 2321 – 2330.

[40] C. Rosenfeld, C. Serra, C. Brochon, and G. Hadziioannou, *High-temperature nitroxide-mediated radical polymerization in a continuous microtube reactor: Towards a better control of the polymerization reaction*, *Chemical Engineering Science* **62** (2007), no. 18 5245 – 5250.

[41] T. Wu, Y. Mei, J. T. Cabral, C. Xu, and K. L. Beers, *A new synthetic method for controlled polymerization using a microfluidic system*, *Journal of the American Chemical Society* **126** (2004), no. 32 9880–9881.

[42] C. Diehl, P. Laurino, N. Azzouz, and P. H. Seeberger, *Accelerated continuous flow raft polymerization*, *Macromolecules* **43** (2010), no. 24 10311–10314.

[43] C. H. Hornung, C. Guerrero-Sanchez, M. Brasholz, S. Saubern, J. Chiefari, G. Moad, E. Rizzardo, and S. H. Thang, *Controlled raft polymerization in a continuous flow microreactor*, *Organic Process Research & Development* **15** (2011), no. 3 593–601.

[44] F. Wojcik, A. G. O'Brien, S. Gtze, P. H. Seeberger, and L. Hartmann, *Synthesis of carbohydrate-functionalised sequence-defined oligo(amidoamine)s by photochemical thiolene coupling in a continuous flow reactor*, *Chemistry A European Journal* **19** (2013), no. 9 3090–3098.

[45] J. J. Griebel, G. Li, R. S. Glass, K. Char, and J. Pyun, *Kilogram scale inverse vulcanization of elemental sulfur to prepare high capacity polymer electrodes for Li-S batteries*, *Journal of Polymer Science Part A: Polymer Chemistry* **53** (2015), no. 2 173–177.

[46] J. Lim, J. Pyun, and K. Char, *Recent Approaches for the Direct Use of Elemental Sulfur in the Synthesis and Processing of Advanced Materials*, *Angewandte Chemie International Edition* **54** (2015), no. 11 3249–3258.

[47] J. J. Griebel, R. S. Glass, K. Char, and J. Pyun, *Polymerizations with elemental sulfur: A novel route to high sulfur content polymers for sustainability, energy and defense*, *Progress in Polymer Science* **58** (2016) 90–125.

[48] M. P. Crockett, A. M. Evans, M. J. H. Worthington, I. S. Albuquerque, A. D. Slattery, C. T. Gibson, J. A. Campbell, D. A. Lewis, G. J. L. Bernardes, and J. M. Chalker, *Sulfur-Limonene Polysulfide: A Material Synthesized Entirely from Industrial By-Products and Its Use in Removing Toxic Metals from Water and Soil*, *Angewandte Chemie* **55** (2016), no. 5 1714–1718.

[49] J. J. Griebel, S. Namnabat, E. T. Kim, R. Himmelhuber, D. H. Moronta, W. J. Chung, A. G. Simmonds, K.-J. Kim, J. van der Laan, N. A. Nguyen, E. L. Dereniak, M. E. Mackay, K. Char, R. S. Glass, R. A. Norwood, and J. Pyun, *New infrared transmitting material via inverse vulcanization of elemental sulfur to prepare high refractive index polymers.*, *Advanced materials* **26** (2014), no. 19 3014–3018.

[50] A. G. Simmonds, J. J. Griebel, J. Park, K. R. Kim, W. J. Chung, V. P. Oleshko, J. Kim, E. T. Kim, R. S. Glass, C. L. Soles, Y.-E. Sung, K. Char, and J. Pyun, *Inverse Vulcanization of Elemental Sulfur to Prepare Polymeric Electrode Materials for Li–S Batteries*, *ACS Macro Letters* **3** (2014), no. 3 229–232.

[51] D. H. P. Kang, M. Chen, and O. A. Ogunseitan, *Potential Environmental and Human Health Impacts of Rechargeable Lithium Batteries in Electronic Waste*, *Environmental Science & Technology* **47** (2013), no. 10 5495–5503.

[52] Y. V. Mikhaylik and J. R. Akridge, *Polysulfide Shuttle Study in the Li/S Battery System*, *Journal of The Electrochemical Society* **151** (2004), no. 11 A1969–A1976.

[53] C. Fu, G. Li, J. Zhang, B. Cornejo, S. S. Piao, K. N. Bozhilov, R. C. Haddon, and J. Guo, *Electrochemical Lithiation of Covalently Bonded Sulfur in Vulcanized Polyisoprene*, *ACS Energy Letters* **1** (2016), no. 1 115–120.

[54] K. A. See, Y.-S. Jun, J. A. Gerbec, J. K. Sprafke, F. Wudl, G. D. Stucky, and R. Seshadri, *Sulfur-Functionalized Mesoporous Carbons as Sulfur Hosts in Li–S Batteries: Increasing the Affinity of Polysulfide Intermediates to Enhance Performance*, *ACS Applied Materials & Interfaces* **6** (2014), no. 14 10908–10916.

[55] K. H. Kim, Y.-S. Jun, J. A. Gerbec, K. A. See, G. D. Stucky, and H.-T. Jung, *Sulfur infiltrated mesoporous graphene–silica composite as a polysulfide retaining cathode material for lithium–sulfur batteries*, *Carbon* **69** (2014) 543–551.

[56] Z. Wei Seh, W. Li, J. J. Cha, G. Zheng, Y. Yang, M. T. McDowell, P.-C. Hsu, and Y. Cui, *Sulphur-TiO2 yolk-shell nanoarchitecture with internal void space for long-cycle lithium-sulphur batteries.*, *Nature Communications* **4** (2013) 1331.

[57] R. Raccichini, A. Varzi, S. Passerini, and B. Scrosati, *The role of graphene for electrochemical energy storage.*, *Nature materials* **14** (2015), no. 3 271–279.

[58] V. P. Oleshko, J. Kim, J. L. Schaefer, S. D. Hudson, C. L. Soles, A. G. Simmonds, J. J. Griebel, R. S. Glass, K. Char, and J. Pyun, *Structural origins of enhanced capacity retention in novel copolymerized sulfur-based composite cathodes for high-energy density Li–S batteries*, *MRS Communications* **5** (2015), no. 03 353–364.

[59] B. Oschmann, J. Park, C. Kim, K. Char, Y.-E. Sung, and R. Zentel, *Copolymerization of Polythiophene and Sulfur To Improve the Electrochemical Performance in Lithium–Sulfur Batteries*, *Chemistry of Materials* **27** (2015), no. 20 7011–7017.

[60] P. T. Dirlam, A. G. Simmonds, R. C. Shallcross, K. J. Arrington, W. J. Chung, J. J. Griebel, L. J. Hill, R. S. Glass, K. Char, and J. Pyun, *Improving the charge conductance of elemental sulfur via tandem inverse vulcanization and electropolymerization*, *ACS Macro Letters* **4** (2015), no. 1 111–114.

[61] M. Arslan, B. Kiskan, and Y. Yagci, *Combining Elemental Sulfur with Polybenzoxazines via Inverse Vulcanization*, *Macromolecules* **49** (2016), no. 3 767–773.

[62] P. T. Dirlam, A. G. Simmonds, T. S. Kleine, N. A. Nguyen, L. E. Anderson, A. O. Klever, A. Florian, P. J. Costanzo, P. Theato, M. E.

Mackay, R. S. Glass, K. Char, and J. Pyun, *Inverse vulcanization of elemental sulfur with 1,4-diphenylbutadiyne for cathode materials in Li–S batteries*, *RSC Advances* **5** (2015) 24718–24722.

[63] Y. Zhang, J. J. Griebel, P. T. Dirlam, N. A. Nguyen, R. S. Glass, M. E. Mackay, K. Char, and J. Pyun, *Inverse vulcanization of elemental sulfur and styrene for polymeric cathodes in li-s batteries*, *Journal of Polymer Science Part A: Polymer Chemistry* **55** (2017), no. 1 107–116.

[64] A. Hoefling, D. T. Nguyen, Y. J. Lee, S.-W. Song, and P. Theato, *A sulfur-eugenol allyl ether copolymer: a material synthesized via inverse vulcanization from renewable resources and its application in li-s batteries*, *Mater. Chem. Front.* **1** (2017) 1818–1822.

[65] J. L. Cawse, J. L. Stanford, and R. H. Still, *Polymers from renewable sources. III. Hydroxy-terminated myrcene polymers*, *Journal of Applied Polymer Science* **31** (1986), no. 7 1963–1975.

[66] T. L. Peppard, *Volatile organosulphur compounds in hops and hop oils: A review*, *Journal of the Institute of Brewing* **87** (1981), no. 6 376–385.

[67] L. Blight, B. R. Currell, B. J. Nash, R. A. M. Scott, and C. Stillo, *Preparation and Properties of Modified Sulfur Systems*, in *Copolymers, Polyblends, and Composites*, pp. 13–30. American Chemical Society, Washington, D.C., 2009.

[68] A. Behr and L. Johnen, *Myrcene as a natural base chemical in sustainable chemistry: A critical review*, *ChemSusChem* **2** (2009), no. 12 1072–1095.

[69] J. M. Bolton, M. A. Hillmyer, and T. R. Hoye, *Sustainable Thermoplastic Elastomers from Terpene-Derived Monomers*, *ACS Macro Letters* **3** (2014), no. 8 717–720.

[70] Z. Sun, M. Xiao, S. Wang, D. Han, S. Song, G. Chen, and Y. Meng, *Sulfur-rich polymeric materials with semi-interpenetrating network structure as a novel lithium–sulfur cathode*, *Journal of Materials Chemistry A* **2** (2014), no. 24 9280–9286.

[71] J. J. Griebel, N. A. Nguyen, A. V. Astashkin, R. S. Glass, M. E. Mackay, K. Char, and J. Pyun, *Preparation of dynamic covalent polymers via inverse vulcanization of elemental sulfur*, *ACS Macro Letters* **3** (2014), no. 12 1258–1261.

[72] J. Hilschmann and G. Kali, *Bio-based polymyrcene with highly ordered structure via solvent free controlled radical polymerization*, *European Polymer Journal* **73** (2015) 363–373.

[73] P. Sarkar and A. K. Bhowmick, *Synthesis, characterization and properties of a bio-based elastomer: polymyrcene*, *RSC Advances* **4** (2014), no. 106 61343–61354.

[74] B. Meyer, *Elemental sulfur*, *Chemical Reviews* **76** (1976), no. 3 367–388.

[75] S. Georges, M. Bria, P. Zinck, and M. Visseaux, *Polymyrcene microstructure revisited from precise high-field nuclear magnetic resonance analysis*, *Polymer* **55** (2014), no. 16 3869–3878.

[76] S. Shukla, A. Ghosh, U. K. Sen, P. K. Roy, S. Mitra, and B. Lochab, *Cardanol benzoxazine-Sulfur Copolymers for Li-S batteries: Symbiosis of Sustainability and Performance*, *ChemistrySelect* **1** (2016), no. 3 594–600.

[77] A. Ghosh, S. Shukla, G. S. Khosla, B. Lochab, and S. Mitra, *Sustainable Sulfur-rich Copolymer/Graphene Composite as Lithium-Sulfur Battery Cathode with Excellent Electrochemical Performance.*, *Scientific Reports* **6** (2016) 25207.

[78] K. A. See, M. Leskes, J. M. Griffin, S. Britto, P. D. Matthews, A. Emly, A. Van der Ven, D. S. Wright, A. J. Morris, C. P. Grey, and R. Seshadri, *Ab Initio Structure Search and in Situ 7Li NMR Studies of Discharge Products in the Li–S Battery System*, *Journal of the American Chemical Society* **136** (2014), no. 46 16368–16377.

[79] S. R. Samanta, R. Cai, and V. Percec, *Set-lrp of semifluorinated acrylates and methacrylates*, *Polym. Chem.* **5** (2014) 5479–5491.

[80] S. R. Samanta, H.-J. Sun, A. Anastasaki, D. M. Haddleton, and V. Percec, *Self-activation and activation of cu(0) wire for set-lrp mediated by fluorinated alcohols*, *Polym. Chem.* **5** (2014) 89–95.

[81] S. R. Samanta and V. Percec, *Synthesis of high molar mass poly(n-butyl acrylate) and poly(2-ethylhexyl acrylate) by set-lrp in mixtures of fluorinated alcohols with dmso*, *Polym. Chem.* **5** (2014) 169–174.

[82] S. R. Samanta, M. E. Levere, and V. Percec, *Set-lrp of hydrophobic and hydrophilic acrylates in trifluoroethanol*, *Polym. Chem.* **4** (2013) 3212–3224.

[83] S. R. Samanta, A. Anastasaki, C. Waldron, D. M. Haddleton, and V. Percec, *Set-lrp of methacrylates in fluorinated alcohols*, *Polym. Chem.* **4** (2013) 5563–5569.

[84] S. R. Samanta, R. Cai, and V. Percec, *A rational approach to activated polyacrylates and polymethacrylates by using a combination of model reactions and set-lrp of hexafluoroisopropyl acrylate and methacrylate*, *Polym. Chem.* **6** (2015) 3259–3270.

[85] S. R. Samanta, A. Anastasaki, C. Waldron, D. M. Haddleton, and V. Percec, *Set-lrp of hydrophobic and hydrophilic acrylates in tetrafluoropropanol*, *Polym. Chem.* **4** (2013) 5555–5562.

[86] S. R. Samanta, R. Cai, and V. Percec, *Synthesis of amphiphilic homopolymers with high chain end functionality by setlrp*, *Journal of Polymer Science Part A: Polymer Chemistry* **53** (2015), no. 2 294–303.

[87] A. Anastasaki, B. Oschmann, J. Willenbacher, A. Melker, M. H. C. Van Son, N. P. Truong, M. W. Schulze, E. H. Discekici, A. J. McGrath, T. P. Davis, C. M. Bates, and C. J. Hawker, *One-Pot Synthesis of ABCDE Multiblock Copolymers with Hydrophobic, Hydrophilic, and Semi-Fluorinated Segments.*, *Angewandte Chemie ASAP* (2017).

[88] E. H. Discekici, A. Anastasaki, R. Kaminker, J. Willenbacher, N. P. Truong, C. Fleischmann, B. Oschmann, D. J. Lunn, J. Read de Alaniz, T. P. Davis, C. M. Bates, and C. J. Hawker, *Light-Mediated Atom Transfer Radical Polymerization of Semi-Fluorinated (Meth)acrylates: Facile Access to Functional Materials.*, *Journal of the American Chemical Society* **139** (2017), no. 16 5939–5945.

[89] W. Du, A. M. Nyström, L. Zhang, K. T. Powell, Y. Li, C. Cheng, S. A. Wickline, and K. L. Wooley, *Amphiphilic hyperbranched fluoropolymers as nanoscopic 19F magnetic resonance imaging agent assemblies.*, *Biomacromolecules* **9** (2008), no. 10 2826–2833.

[90] J. Ilavsky, *Nika: software for two-dimensional data reduction*, *Journal of Applied Crystallography* **45** (2012), no. 2 324–328.

[91] K. Kim, M. W. Schulze, A. Arora, R. M. Lewis, M. A. Hillmyer, K. D. Dorfman, and F. S. Bates, *Thermal processing of diblock copolymer melts mimics metallurgy.*, *Science* **356** (2017), no. 6337 520–523.

[92] S. Lee, C. Leighton, and F. S. Bates, *Sphericity and symmetry breaking in the formation of Frank-Kasper phases from one component materials.*, *Proceedings of the National Academy of Sciences of the United States of America* **111** (2014), no. 50 17723–17731.

[93] S. Lee, M. J. Bluemle, and F. S. Bates, *Discovery of a Frank-Kasper sigma phase in sphere-forming block copolymer melts.*, *Science* **330** (2010), no. 6002 349–353.

[94] T. M. Gillard, S. Lee, and F. S. Bates, *Dodecagonal quasicrystalline order in a diblock copolymer melt.*, *Proceedings of the National Academy of Sciences of the United States of America* **113** (2016), no. 19 5167–5172.

[95] J. Zhang and F. S. Bates, *Dodecagonal quasicrystalline morphology in a poly(styrene-b-isoprene-b-styrene-b-ethylene oxide) tetrablock terpolymer*, *Journal of the American Chemical Society* **134** (2012), no. 18 7636–7639.

[96] M. W. Schulze, R. M. Lewis, J. H. Lettow, R. J. Hickey, T. M. Gillard, M. A. Hillmyer, and F. S. Bates, *Conformational Asymmetry and Quasicrystal Approximants in Linear Diblock Copolymers.*, *Physical review letters* **118** (2017), no. 20 207801.

[97] N. Xie, W. Li, F. Qiu, and A.-C. Shi, *σ Phase Formed in Conformationally Asymmetric AB-Type Block Copolymers*, *ACS Macro Letters* **3** (2014), no. 9 906–910.

[98] G. M. Grason, B. A. DiDonna, and R. D. Kamien, *Geometric theory of diblock copolymer phases*, *Phys. Rev. Lett.* **91** (Jul, 2003) 058304.

[99] D. V. Perroni and M. K. Mahanthappa, *Inverse Pm3n cubic micellar lyotropic phases from zwitterionic triazolium gemini surfactants*, *Soft Matter* **9** (2013), no. 33 7919–7922.

[100] J. Tang, Y. Jiang, X. Zhang, D. Yan, and J. Z. Y. Chen, *Phase Diagram of Rod–Coil Diblock Copolymer Melts*, *Macromolecules* **48** (2015), no. 24 9060–9070.

[101] H. Pattabhiraman and M. Dijkstra, *On the formation of stripe, sigma, and honeycomb phases in a core-corona system*, *Soft Matter* **13** (2017) 4418–4432.

[102] M. Huang, C.-H. Hsu, J. Wang, S. Mei, X. Dong, Y. Li, M. Li, H. Liu, W. Zhang, T. Aida, W.-B. Zhang, K. Yue, and S. Z. D. Cheng,

Self-assembly. Selective assemblies of giant tetrahedra via precisely controlled positional interactions., *Science* **348** (2015), no. 6233 424–428.

[103] P. Ziherl and R. D. Kamien, *Maximizing entropy by minimizing area: towards a new principle of self-organization*, *The Journal of Physical Chemistry B* **105** (2001), no. 42 10147–10158.

[104] P. Turchi, G. Treglia, and F. Ducastelle, *Electronic structure and phase stability of a15 transition metals and alloys*, *Journal of Physics F: Metal Physics* **13** (1983), no. 12 2543.

[105] S. Wang, S. Vajjala Kesava, E. D. Gomez, and M. L. Robertson, *Sustainable Thermoplastic Elastomers Derived from Fatty Acids*, *Macromolecules* **46** (Sept., 2013) 7202–7212.

[106] *Order-disorder phenomena in complex alloys: The case of a15-based substitutional alloys*, *MRS Proceedings* **186** (1990) 101.

[107] C. D. R., W. B. M., B. Hilda, F. J. A., F. Daniel, C. A. S., S. R. A., and O. C. K., *Oligopeptide-modified hydrophobic and hydrophilic polymers as antifouling coatings*, *Green Materials* **5** (2017), no. 1 31–43.

[108] J. M. Ren, T. G. McKenzie, Q. Fu, E. H. H. Wong, J. Xu, Z. An, S. Shanmugam, T. P. Davis, C. Boyer, and G. G. Qiao, *Star Polymers.*, *Chemical Reviews* **116** (2016), no. 12 6743–6836.

[109] K. Wang, H. Peng, K. J. Thurecht, and A. K. Whittaker, *Fluorinated POSS-Star Polymers for 19F MRI*, *Macromolecular Chemistry and Physics* **217** (2016), no. 20 2262–2274.

[110] X. Pang, L. Zhao, W. Han, X. Xin, and Z. Lin, *A general and robust strategy for the synthesis of nearly monodisperse colloidal nanocrystals.*, *Nature nanotechnology* **8** (2013), no. 6 426–431.

[111] J. Qu, X. Luo, and Z. Wang, *Fluorinated star-shaped block copolymers: Synthesis and optical properties*, *Journal of Polymer Science Part A: Polymer Chemistry* **54** (2016), no. 13 1969–1977.

[112] H. G. and and K. Matyjaszewski, *Synthesis of Star Polymers by a Combination of ATRP and the "Click" Coupling Method*, *Macromolecules* **39** (2006), no. 15 4960–4965.

[113] K. Matyjaszewski, P. J. Miller, J. Pyun, G. Kickelbick, and S. Diamanti, *Synthesis and characterization of star polymers with varying arm number, length, and composition from organic and hybrid inorganic/organic multifunctional initiators*, *Macromolecules* **32** (1999), no. 20 6526–6535.

[114] K. Matyjaszewski, *The synthesis of functional star copolymers as an illustration of the importance of controlling polymer structures in the design of new materials*, *Polymer international* **52** (2003), no. 10 1559–1565.

[115] J. M. Ren, Q. Fu, A. Blencowe, and G. G. Qiao, *Organic Catalyst-Mediated Ring-Opening Polymerization for the Highly Efficient Synthesis of Polyester-Based Star Polymers*, *ACS Macro Letters* **1** (2012), no. 6 681–686.

[116] M. Stenzel Rosenbaum, T. P. Davis, V. Chen, and A. G. Fane, *Star-polymer synthesis via radical reversible addition–fragmentation chain-transfer polymerization*, *Journal of Polymer Science Part A: Polymer Chemistry* **39** (2001), no. 16 2777–2783.

[117] J. Liu, H. Duong, M. R. Whittaker, T. P. Davis, and C. Boyer, *Synthesis of Functional Core, Star Polymers via RAFT Polymerization for Drug Delivery Applications*, *Macromolecular Rapid Communications* **33** (2012), no. 9 760–766.

[118] J. Liu, L. Tao, J. Xu, Z. Jia, C. Boyer, and T. P. Davis, *RAFT controlled synthesis of six-armed biodegradable star polymeric architectures via a 'core-first' methodology*, *Polymer* **50** (2009), no. 19 4455–4463.

[119] V. Darcos, A. Duréault, D. Taton, Y. Gnanou, P. Marchand, A.-M. Caminade, J.-P. Majoral, M. Destarac, and F. Leising, *Synthesis of hybrid dendrimer-star polymers by the RAFT process.*, *Chemical communications* **99** (2004), no. 18 2110–2111.

[120] B. Wenn, A. C. Martens, Y. M. Chuang, J. Gruber, and T. Junkers, *Efficient multiblock star polymer synthesis from photo-induced copper-mediated polymerization with up to 21 arms*, *Polymer Chemistry* **7** (2016), no. 15 2720–2727.

[121] Z. Zhang, Y. Gnanou, and N. Hadjichristidis, *Well-defined 4-arm stars with hydroxy-terminated polyethylene, polyethylene- b -polycaprolactone and polyethylene- b -(polymethyl methacrylate) 2 arms*, *Polymer Chemistry* **7** (2016), no. 35 5507–5511.

[122] S. Angot, K. S. Murthy, D. Taton, and Y. Gnanou, *Atom transfer radical polymerization of styrene using a novel octafunctional initiator: Synthesis of well-defined polystyrene stars*, *Macromolecules* **31** (1998), no. 21 7218–7225.

[123] H. Ding, S. Park, M. Zhong, X. Pan, J. Pietrasik, C. J. Bettinger, and K. Matyjaszewski, *Facile Arm-First Synthesis of Star Block Copolymers via ARGET ATRP with ppm Amounts of Catalyst*, *Macromolecules* **49** (2016), no. 18 6752–6760.

[124] R. Aksakal, M. Resmini, and C. R. Becer, *Pentablock star shaped polymers in less than 90 minutes via aqueous SET-LRP*, *Polymer Chemistry* **7** (2016), no. 1 171–175.

[125] C. Boyer, A. H. Soeriyadi, P. B. Zetterlund, and M. R. Whittaker, *Synthesis of Complex Multiblock Copolymers via a Simple Iterative Cu(0)-Mediated Radical Polymerization Approach*, *Macromolecules* **44** (2011), no. 20 8028–8033.

[126] C. Boyer, A. Atme, C. Waldron, A. Anastasaki, P. Wilson, P. B. Zetterlund, D. Haddleton, and M. R. Whittaker, *Copper(0)-mediated radical polymerisation in a self-generating biphasic system*, *Polymer Chemistry* **4** (2013), no. 1 106–112.

[127] C. Waldron, A. Anastasaki, R. McHale, P. Wilson, Z. Li, T. Smith, and D. M. Haddleton, *Copper-mediated living radical polymerization (SET-LRP) of lipophilic monomers from multi-functional initiators: reducing star–star coupling at high molecular weights and high monomer conversions*, *Polymer Chemistry* **5** (2014), no. 3 892–898.

[128] A. Anastasaki, V. Nikolaou, G. Nurumbetov, P. Wilson, K. Kempe, J. F. Quinn, T. P. Davis, M. R. Whittaker, and D. M. Haddleton, *Cu(0)-Mediated Living Radical Polymerization: A Versatile Tool for Materials Synthesis*, *Chemical Reviews* **116** (2015), no. 3 835–877.

[129] V. Percec, T. Guliashvili, J. S. Ladislaw, A. Wistrand, A. Stjerndahl, M. J. Sienkowska, M. J. Monteiro, and S. Sahoo, *Ultrafast synthesis of ultrahigh molar mass polymers by metal-catalyzed living radical polymerization of acrylates, methacrylates, and vinyl chloride mediated by SET at 25 degrees C.*, *Journal of the American Chemical Society* **128** (2006), no. 43 14156–14165.

[130] A. Anastasaki, V. Nikolaou, and D. M. Haddleton, *Cu(0)-mediated living radical polymerization: recent highlights and applications; a perspective*, *Polymer Chemistry* **7** (2016), no. 5 1002–1026.

[131] K. Matyjaszewski, S. Coca, S. G. Gaynor, M. Wei, and B. E. Woodworth, *Zerovalent metals in controlled/living radical polymerization*, *Macromolecules* **30** (1997), no. 23 7348–7350.

[132] B. M. Rosen and V. Percec, *Single-Electron Transfer and Single-Electron Transfer Degenerative Chain Transfer Living Radical Polymerization*, *Chemical Reviews* **109** (2009), no. 11 5069–5119.

[133] D. Lu, M. D. Hossain, Z. Jia, and M. J. Monteiro, *One-Pot Orthogonal Copper-Catalyzed Synthesis and Self-Assembly of l-Lysine-Decorated Polymeric Dendrimers*, *Macromolecules* **48** (2015), no. 6 1688–1702.

[134] A. J. Limer, A. K. Rullay, V. S. Miguel, C. Peinado, S. Keely, E. Fitzpatrick, S. D. Carrington, D. Brayden, and D. M. Haddleton, *Fluorescently tagged star polymers by living radical polymerisation for mucoadhesion and bioadhesion*, *Reactive and Functional Polymers* **66** (2006), no. 1 51–64.

[135] J. Li and H. Xiao, *An efficient synthetic-route to prepare [2,3,6-tri-O-(2-bromo-2-methylpropionyl]-β-cyclodextrin)*, *Tetrahedron Letters* **46** (2005), no. 13 2227–2229.

[136] P. Chmielarz, S. Park, A. Sobkowiak, and K. Matyjaszewski, *Synthesis of β-cyclodextrin-based star polymers via a simplified electrochemically mediated ATRP*, *Polymer* **88** (2016) 36–42.

[137] Y. Sakai-Otsuka, S. Zaioncz, I. Otsuka, S. Halila, P. Rannou, and R. Borsali, *Self-Assembly of Carbohydrate-block-Poly(3-hexylthiophene) Diblock Copolymers into Sub-10 nm Scale Lamellar Structures*, *Macromolecules* **50** (2017), no. 8 3365–3376.

[138] A. C. Carr, L. E. Felberg, V. A. Piunova, J. E. Rice, T. Head-Gordon, and W. C. Swope, *Effect of Hydrophobic Core Topology and Composition on the Structure and Kinetics of Star Polymers: A Molecular Dynamics Study*, *The Journal of Physical Chemistry B* **121** (2017), no. 13 2902–2918.

[139] Q. Ma and K. L. Wooley, *The preparation of t-butyl acrylate, methyl acrylate, and styrene block copolymers by atom transfer radical polymerization: Precursors to amphiphilic and hydrophilic block copolymers*

and conversion to complex nanostructured materials, *Journal of Polymer Science Part A: Polymer Chemistry* **38** (2000), no. S1 4805–4820.

[140] C. Boyer, A. Derveaux, P. B. Zetterlund, and M. R. Whittaker, *Synthesis of multi- block copolymer stars using a simple iterative Cu(0)-mediated radical polymerization technique*, *Polymer Chemistry* **3** (2012), no. 1 117–123.

[141] N. H. Nguyen, B. M. Rosen, X. Jiang, S. Fleischmann, and V. Percec, *New efficient reaction media for SET-LRP produced from binary mixtures of organic solvents and H2O*, *Journal of Polymer Science Part A: Polymer Chemistry* **47** (2009), no. 21 5577–5590.

[142] K. Ohno, B. Wong, and D. M. Haddleton, *Synthesis of well-defined cyclodextrin-core star polymers*, *Journal of Polymer Science Part A: Polymer Chemistry* **39** (July, 2001) 2206–2214.